Radar imaging techniques for the characterization and diagnosis of roadways

Mengda Wu

COLLEGE MATHS, TELECOMS
DOCTORAL INFORMATIQUE, SIGNAL
BRETAGNE SYSTEMES, ELECTRONIQUE

Université de Rennes

THÈSE DE DOCTORAT DE

L'UNIVERSITÉ DE RENNES

ÉCOLE DOCTORALE N° 601
Mathématiques, Télécommunications, Informatique, Signal, Systèmes, Électronique
Spécialité : *Télécommunications*

Par

Mengda WU

Radar imaging techniques for the characterization and diagnosis of roadways

Thèse présentée et soutenue à Toulouse, le 14/12/2023
Unité de recherche : Institut d'Electronique et des Technologies du numéRique (IETR)
Thèse N° : « »

Rapporteurs avant soutenance :

Atika RIVENQ MENHAJ	Professeur, Université Polytechnique Hauts-de-France, Valenciennes, France
Torbjorn ELTOFT	Professeur, Arctic University of Norway, Tromso, Norway

Composition du Jury :

Président :	Philippe PAILLOU	Professeur, Université de Bordeaux, Bordeaux, France
Examinateurs :	Philippe PAILLOU	Professeur, Université de Bordeaux, Bordeaux, France
	David GUILBERT	Chercheur, CEREMA, Angers, France
Dir. de thèse :	Laurent FERRO-FAMIL	Professeur, Université de Rennes, Rennes, France
Co-dir. de thèse :	Yide WANG	Professeur, Université de Nantes, Nantes, France

Acknowledgement

This thesis is dedicated to my mother WANG Wei for her lifelong support to me, and to Prof. WU Liuren for his help.

I would like to express my deepest gratitude to my supervisor, Prof. Laurent Ferro-Famil, for his invaluable guidance, unwavering support, and extensive expertise throughout the course of my research. His mentorship has not only enriched my academic experience but also played a pivotal role in my personal and professional growth. I am truly fortunate to have the privilege of being under his guidance, and I am sincerely thankful for his continuous encouragement and belief in my life.

I would extend my heartfelt thanks to my co-supervisor, Prof. Yide Wang, for his exceptional guidance in the realm of signal processing. His rigorous and conscientious attitude towards research has set a benchmark for my research career. Moreover, I am deeply grateful to Frederic Boutet for his invaluable assistance and expertise during the experiments. His technical skills and experience greatly contributed to the success of the measurements.

I also would like to acknowledge my dear friends and colleagues, Clément Férise, Ray Abdo, and Lekhmissi Harkati, for the precious memories we have created together, both in our research endeavors and life in Rennes. As I reflect on the last year in ISAE-SUPAERO, I feel fortunate to embark on a new chapter with Yi Ding, Florent Feriol, Justin Cano, César Debunne, Titouan Tyack, and Léa Dubereil. Their support and camaraderie have been instrumental in shaping the last phase of my thesis.

Finally, I would like to express my heartfelt gratitude to all of my friends for their support and companionship throughout the journey of this thesis.

Table of Contents

Résumé **9**

1 Introduction **17**
1.1 Context and motivation . . . 17
1.2 Microwave monitoring techniques . . . 19
1.2.1 Non destructive testing - GPR . . . 19
1.2.2 Remote sensing techniques - SAR . . . 20
1.3 Thesis contributions and outline . . . 21

2 Principles of SAR imaging **25**
2.1 Introduction . . . 25
2.2 Principle of a coherent radar system . . . 26
2.2.1 Objectives of a coherent radar measurement . . . 26
2.2.2 Signal model of radar responses . . . 26
2.3 Range focusing techniques . . . 28
2.3.1 Radar waveforms . . . 29
2.3.2 Range focusing . . . 32
2.4 2-D SAR imaging techniques . . . 36
2.4.1 Geometry a SAR measurement . . . 37
2.4.2 2-D SAR focusing . . . 39
2.4.3 Properties of focused signal in azimuth . . . 45
2.5 TomoSAR imaging techniques . . . 46
2.5.1 Tomographic SAR geometry . . . 46
2.5.2 3-D tomographic focusing . . . 48
2.6 Conclusion . . . 50

3 Comparison of SAR imaging configurations for roadway characterization **51**
3.1 Introduction . . . 51
3.2 Comparison of imaging modes . . . 53

3.2.1 Nadir-looking ground penetrating radar . . . 53
3.2.2 Off-nadir synthetic aperture radar . . . 54
3.3 Experiment configuration for roadway characterization . . . 59
3.3.1 Ground-based SAR system operated in BSC and FSC configuration 59
3.3.2 Experiment setup and scene description . . . 61
3.4 Measurement campaign results . . . 64
3.4.1 Comparison of configurations . . . 64
3.4.2 Tomography correction with refraction compensation . . . 71
3.5 Result analysis and advanced feature extraction of roadways . . . 75
3.5.1 Analysis of imaging configurations . . . 75
3.5.2 Permittivity estimation with polarization response . . . 77
3.5.3 Roughness estimation . . . 80
3.6 Conclusion . . . 82

4 Sliding bistatic TomoSAR imaging 85
4.1 Introduction . . . 85
4.2 Investigation of the sliding FSC mode . . . 86
4.2.1 Sliding forward-scattering . . . 87
4.2.2 Resolution comparison of imaging modes . . . 88
4.3 Measurement configuration . . . 90
4.3.1 Sliding Off-Nadir System . . . 90
4.3.2 Bituminous slabs designed for measurements . . . 92
4.4 Measurement campaign results and polarization analysis . . . 95
4.4.1 Illustration of COSBis scattering mechanisms . . . 95
4.4.2 Standard monolayer slabs . . . 95
4.4.3 Horizontal crack . . . 98
4.4.4 Vertical crack . . . 100
4.4.5 Analysis of polarimetric responses . . . 104
4.5 Conclusion . . . 108

5 Bistatic imaging using high-resolution spectral estimation techniques 111
5.1 Introduction . . . 111
5.2 Generic signal model . . . 112
5.2.1 Simple model for a non dispersive medium . . . 112
5.2.2 Stochastic aspects . . . 113

5.2.3 Spectral smoothing 114
5.3 Spectral estimation methods 117
5.3.1 Nonparametric methods 118
5.3.2 Parametric methods 118
5.3.3 Spectral estimation applied to defects inspection using a nadir-looking GPR 119
5.4 High-resolution imaging techniques applied in the COSBis configuration . . 120
5.4.1 Principles of COSBis focusing using spectral estimation methods . . 120
5.4.2 Horizontal crack 123
5.4.3 Vertical crack 125
5.5 Conclusion 126

Conclusions and Perspectives **129**

Bibliography **133**

Publications **142**

TABLE DES FIGURES

1 Structure d'une chaussée flexible 9
2 Illustration des résultats de la focalisation SAR 11
3 Illustrations des configurations et des résultats de focalisation au chapitre 3 12
4 Illustrations des configurations et des résultats de focalisation au chapitre 4 13
5 Illustration de l'imagerie à haute résolution au chapitre 5 14

1.1 Flexible Pavement structure 18

2.1 Principle of a radar measurement, with $s_e(\tau)$ being the emitted signal and $s_r(\tau)$ being the response of an object 26
2.2 Synopsis of a coherent radar system 27
2.3 Examples of pulsed radar waveforms 29
2.4 Examples of continuous radar waveforms 31
2.5 Synopsis of a CW radar 31
2.6 Illustration of range resolution and ambiguity in detecting multi targets . . 33
2.7 Observation modes of radar measurements 37
2.8 Geometry of a side-looking measurement [FP16a] 38
2.9 SAR measurement of multi scatterers [FP16a] 40
2.10 Geometry of a rectilinear SAR measurement with regular sampling [FP16a] 41
2.11 Range migration 43
2.12 SAR focusing using back projection 44
2.13 Geometry of a TomoSAR acquisition 47
2.14 Schematic of TomoSAR 3-D focsuing 49

3.1 Geometry of a nadir-looking GPR acquisition 54
3.2 Geometry of off-nadir SAR imaging in BSC and FSC modes 55
3.3 Illustration of cylindrical ambiguity when measuring 3 superimposed layers in BSC mode 56
3.4 Illustration of ground-range ambiguity when measuring 3 superimposed layers in FSC mode 58

3.5 Graphical representation of tomographic resolution cells separating two horizontal layers with $\theta_1 = \theta_2 = 45°$ 59
3.6 Configurations used during the experiment 60
3.7 Overview of the fatigue-test facility [Dér+21] 62
3.8 Description of the debonded roadway zones 63
3.9 Nadir-looking focusing results obtained over different zones 65
3.10 BSC 2-D focusing results obtained over different zones 66
3.11 BSC tomographic imaging results over different zones 67
3.12 FSC single-channel focusing results over different zones 68
3.13 FSC tomographic imaging results over different zones 69
3.14 Schematic of refraction compensation 72
3.15 Illustration of refraction effect and its compensation with the simulated medium 73
3.16 Results comparison before and after compensation over geotextile zone at X band 74
3.17 Compensated imaging results over the sand zone 75
3.18 Compensated imaging results over the air-gap zone 76
3.19 Parametric reflectivity of different zones 80
3.20 Roughness estimation 81

4.1 Geometrical configuration of imaging modes 87
4.2 Resolution comparison simulated over single scatter at (1, 0) 89
4.3 Configurations used during the experiment 91
4.4 Structure of the surface layer in a flexible pavement 92
4.5 Description of asphalt samples used in experiments 93
4.6 Illustration of the artificial cracks used in experiments 94
4.7 Illustration of FSC and BSC scattering mechanisms with focused images of metal handles lying on a wooden floor at X band 96
4.8 Illustration of FSC and BSC scattering mechanisms with focused images of metal handles lying on a wooden floor at C band 97
4.9 Focusing results over VTBC 98
4.10 Focusing results over STBC 99
4.11 Focusing results over HMA 100
4.12 Focusing results over a horizontal detachment with <1 mm vertical space . 101
4.13 Focusing results over a horizontal detachment with 5mm vertical space . . 102

4.14 Focusing results over a vertical crack of <1mm width 103
4.15 Focusing results over a vertical crack of 5mm width 104
4.16 Permittivity estimation with FSC focusing results in HH and VV polarizations over STBC 105
4.17 HH and VV polarization images in FSC mode. 1-D normalized profiles (e) and (f) are acquired along the white dash lines in (a)(c) and (b)(d), correspondingly. 106
4.18 HH and VV polarization images in FSC mode. 1-D normalized profiles in (c) are acquired along the white dash lines in (a) and (b). 107
4.19 Comparison of BSC focusing results in HH and VV polarizations over the horizontal gap 108

5.1 Subarrays of SSP method 115
5.2 Variation of correlation coefficient $\hat{\rho}_{mn}$ and resolution α_{mn} in the case of $\rho_{mn} = 1$ 116
5.3 Structure of the sand-defect zone 119
5.4 Application of spectral estimation techniques to nadir-looking A-scan at C and X bands over the sand-defect zone 120
5.5 Application of spectral estimation techniques to nadir-looking B-scan at C and X bands over the sand-defect zone 121
5.6 Illustration of focusing grids of BSC and COSBis modes 122
5.7 Original COSBis images over the horizontal crack 123
5.8 Application of spectral estimation techniques to COSBis at VV and HH polarizations over the horizontal crack 124
5.9 Original COSBis images over the vertical crack 126
5.10 Application of spectral estimation techniques to COSBis at VV and HH polarizations over the vertical crack 127

Résumé

Le réseau routier national français, qui s'étend sur une distance excédant un million de kilomètres, revêt une importance capitale en tant qu'élément fondamental de l'infrastructure de transport nationale. Au sein de cet imposant maillage, sont répertoriés quelque 11 000 kilomètres d'autoroutes, édifiées selon une structure de chaussée flexible, composée de plusieurs strates superposées, comme illustré à la Figure 1. La complexité inhérente à ce système implique une maintenance régulière et méticuleuse, condition sine qua non pour assurer la sécurité et la pérennité de ces voies de circulation. Les opérations d'entretien embrassent une vaste palette d'interventions visant à préserver l'intégrité et la qualité de la chaussée. Ces efforts se révèlent cruciaux pour garantir le bien-être de l'ensemble des usagers de la route [Dat23 ; SS00 ; IDR14].

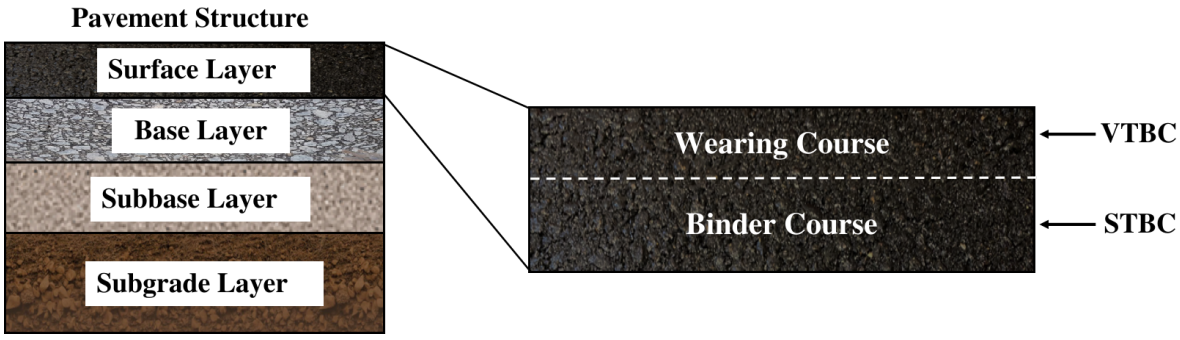

Figure 1 – Structure d'une chaussée flexible

Un aspect essentiel de l'entretien routier réside dans l'examen minutieux des fissures encastrées. Cette démarche sert un double objectif : mesurer l'épaisseur de ces revêtements et détecter, et surveiller d'éventuelles fissures qui pourraient s'être développées. La surveillance des fissures revêt une importance particulière, car elles peuvent compromettre l'intégrité structurelle de la route et représenter un danger pour les automobilistes. L'évaluation systématique et la résolution de ces problèmes permettent aux autorités routières de maintenir de manière proactive la sécurité et la durabilité du réseau routier [SS00 ; BP15 ; Le 07].

L'augmentation constante du volume de circulation en France complexifie la tâche de l'entretien routier. Cette croissance constante nécessite la réévaluation périodique des

conceptions de la structure routière pour accueillir des charges plus lourdes et un flux de circulation accru. Lorsque de nouveaux projets de construction sont entrepris, l'objectif principal est d'estimer les épaisseurs des composants de la chaussée et de vérifier s'ils sont conformes aux exigences strictes définies dans les spécifications du projet. Ce processus de vérification est essentiel pour s'assurer que l'infrastructure achevée est robuste, sûre et adaptée à l'usage.

La détection, la localisation et la caractérisation des fissures encastrées, qu'elles soient horizontales ou verticales, sont nécessaires pour formuler des stratégies rigoureuses d'entretien et de gestion. Ces irrégularités structurelles servent d'indicateurs critiques de l'état dégradé d'un matériau, entraînant une réduction notable de la durée de vie opérationnelle de la chaussée. Comprendre les paramètres géométriques précis de ces défauts, englobant leur morphologie, leurs dimensions et leur profondeur d'occurrence, ainsi qu'une analyse complète de la caractérisation électromagnétique de la permittivité, de la perméabilité, de l'atténuation et du coefficient de diffusion, sont des métriques cruciales pour évaluer l'intégrité et la durabilité de ces systèmes. Cette approche diagnostique facilite non seulement la localisation précise des pathologies potentielles au sein de la structure, mais permet également une évaluation rigoureuse de son état de santé global. De plus, elle permet des prévisions précises concernant son évolution future, augmentant ainsi l'efficacité des outils de soutien à la décision dans l'entretien et la gestion structurels.

Pour l'entretien efficace et durable du vaste réseau routier français, il est impératif d'atteindre une détection précoce, une localisation précise et une caractérisation géométrique précise de ces défauts. L'identification précoce de fissures minces (horizontales ou verticales) demeure un défi persistant en raison des minuscules épaisseurs des vides résultant de telles fissures. Ce défi revêt une importance significative pour les utilisateurs finaux, notamment les clients et les autorités attributaires, car il permet d'optimiser l'entretien de la structure routière une fois que ces défauts sont identifiés à un stade précoce.

Les dispositifs radar à micro-ondes utilisant des techniques de contrôle non destructif (NDT) et de télédétection se sont révélés être des capteurs précieux pour la détection et la caractérisation des caractéristiques en sous-surface. Le Radar à Pénétration de Sol (GPR), un outil NDT de premier plan, joue un rôle essentiel dans ce domaine. Il utilise des ondes électromagnétiques haute fréquence pour sonder le sous-sol, fournissant des informations détaillées sur l'état des couches de chaussée et les défauts potentiels. De plus, la technologie d'imagerie SAR contribue de manière significative à l'évaluation des chaussées. Les satellites et les avions équipés de SAR capturent des images à haute résolution

de la surface de la Terre, permettant la détection de déformations, de rugosités de surface et d'autres caractéristiques cruciales. Ces approches garantissent la détection précoce et la caractérisation précise des anomalies structurelles, améliorant ainsi la durabilité et la sécurité des réseaux routiers.

L'objectif principal de cette thèse tourne autour de la caractérisation exhaustive des défauts encastrés et de l'estimation précise de leurs attributs géométriques dans la surveillance précoce des chaussées. Cette recherche se concentre sur les développements méthodologiques de l'imagerie tomographique 3-D à l'aide du SAR au Sol (GB-SAR) dans l'inspection des chaussées. Deux configurations novatrices de GB-SAR bistatique ont été rigoureusement examinées par le biais d'analyses théoriques et de validations expérimentales, et comparées à l'approche bien établie du GPR. Les résultats mettent en lumière les avantages distincts des approches proposées dans la caractérisation des fissures encastrées et dans l'estimation des propriétés électromagnétiques des chaussées flexibles. Cette contribution majeure aborde non seulement les défis actuels, mais pose également les bases pour les avancées futures dans le domaine de l'inspection et du diagnostic des chaussées.

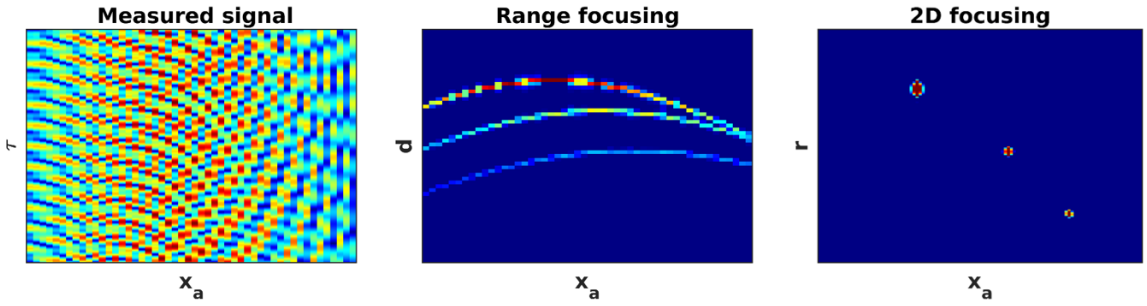

FIGURE 2 – Illustration des résultats de la focalisation SAR

Le chapitre 2 offre une introduction approfondie aux techniques d'imagerie par SAR, offrant une compréhension approfondie des principes du radar, de la propagation des ondes électromagnétiques à l'acquisition du signal. Le chapitre établit un cadre fondamental, présentant un modèle simplifié pour les signaux radar. Il explore la focalisation en distance (1-D), en utilisant la diversité spectrale et des formes d'onde différentes. Ensuite, la discussion s'élargit pour englober les techniques d'imagerie SAR bidimensionnelles (2-D), mettant en évidence le rôle crucial de la diversité spatiale dans l'obtention d'images de haute qualité. Le point culminant réside dans l'exploration du SAR tomographique (Tomo-SAR) à l'aide de données multi-baselines, permettant l'estimation de profils de

réflectivité tridimensionnels (3-D) des environnements observés.

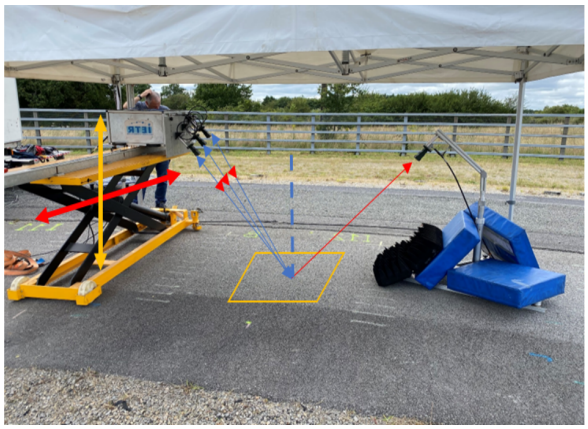

(a) Système GB-SAR utilisé en modes BSC et FSC

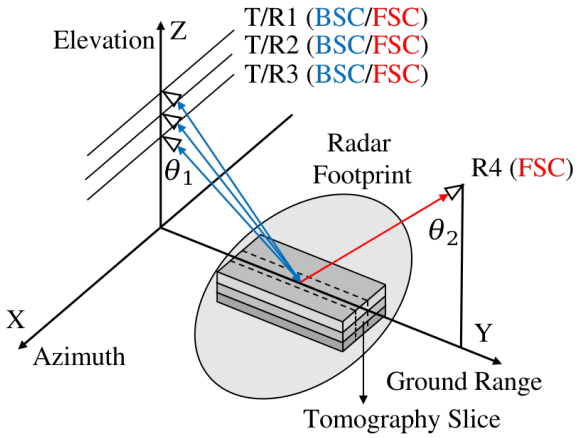

(b) Géométries d'acquisition Tomo BSC et FSC

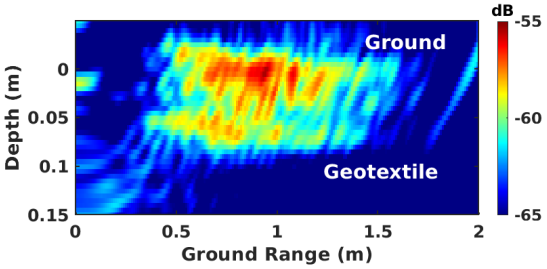

(c) Résultats focalisés sur les défauts intégrés Mode BSC

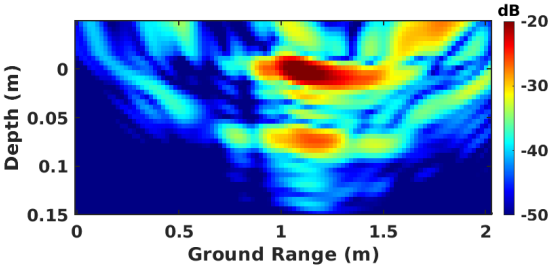

(d) Résultats focalisés sur les défauts intégrés Mode FSC

FIGURE 3 – Illustrations des configurations et des résultats de focalisation au chapitre 3

Le chapitre 3 étudie les configurations radar, y compris le GPR, le Tomo-SAR en modes BSC et FSC, pour l'évaluation des chaussées. Le système SAR tomographique bistatique à visée oblique proposé montre un potentiel remarquable dans la détection des défauts et la caractérisation des routes, grâce à son rapport signal/bruit élevé et à sa résolution verticale constante permettant d'estimer des paramètres critiques tels que la rugosité et la permittivité diélectrique. Un système GB-SAR, fonctionnant en modes BSC et FSC, a été développé à l'Université de Rennes et testé sur les installations routières de l'UGE à Nantes, en France.

Les résultats expérimentaux et l'analyse théorique indiquent les forces et les faiblesses de chaque configuration. La configuration orientée vers le nadir est efficace, surtout avec des signaux à largeur de bande modifiée. Le BSC Tomo-SAR rencontre des difficultés

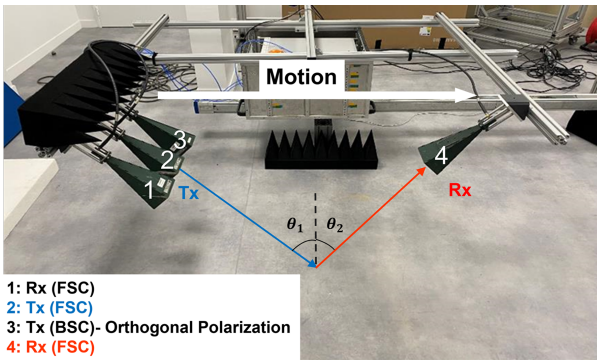

(a) Système GB-SAR en mouvement (COSBis) fonctionnant en mode FSC

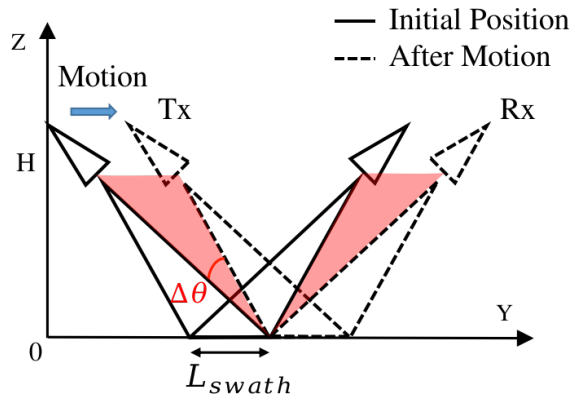

(b) Configuration FSC à déplacement

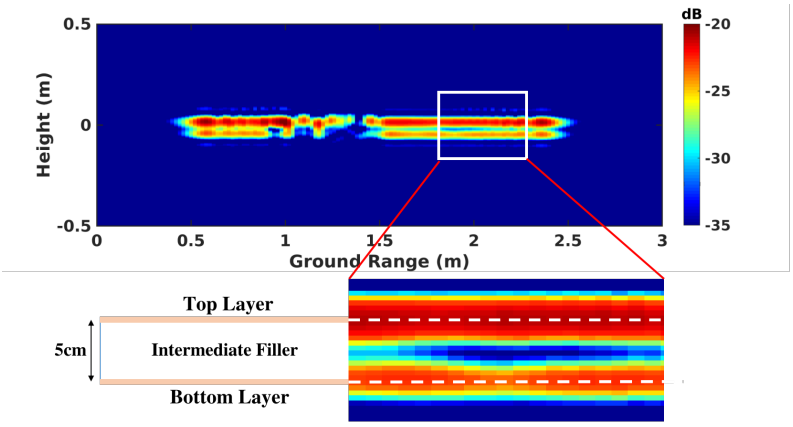

(c) Discrimination verticale - Mode FSC

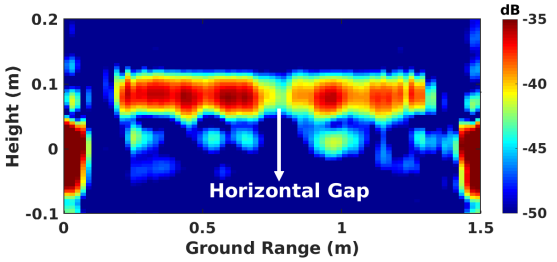

(d) Discrimination horizontale - Mode FSC

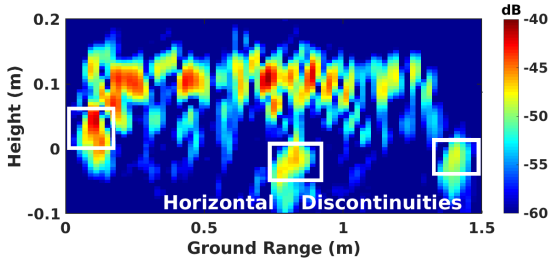

(e) Discrimination horizontale - Mode FSC

FIGURE 4 – Illustrations des configurations et des résultats de focalisation au chapitre 4

avec les surfaces lisses. Le FSC Tomo-SAR se révèle le plus prometteur, isolant efficacement tous les types de défauts, notamment dans la bande X améliorée. L'incorporation de diversités polarimétriques et angulaires améliore les estimations et corrige les distorsions géométriques. L'utilisation du mode de propagation vers l'avant (FSC) permet de

caractériser des défauts légers et d'estimer des paramètres géophysiques clés, tels que la rugosité et la permittivité diélectrique.

Le chapitre 4 présente une nouvelle avancée dans le domaine de l'inspection des routes grâce au développement d'une configuration SAR bistatique à déplacement. Ce mode résout une limitation critique du Tomo-SAR dans la direction de déplacement en mettant en œuvre le FSC à canal unique avec un mouvement contrôlé. Des expériences avec un système GB-SAR en mouvement (COSBis) sur des échantillons d'asphalte donnent des résultats convaincants, mettant l'accent sur la détection de cibles souterraines et de fissures de quelques millimètres de large.

Le SAR bistatique à déplacement démontre une discrimination horizontale tout en maintenant une résolution verticale constante. Il distingue efficacement les fissures verticales et horizontales et a montré une sensibilité aux variations de largeur de défauts. Le mode BSC s'est distingué dans la discrimination horizontale, permettant une localisation claire des discontinuités. La diversité polarimétrique facilite l'estimation de la permittivité diélectrique et révèle d'intéressantes différences de sensibilité entre les polarisations. La structure adaptable du COSBis offre une alternative prometteuse pour l'analyse des chaussées, se basant sur une configuration simple, qui permet d'atteindre une discrimination forte dans les dimensions verticales et horizontales, et qui montre une sensibilité à la polarisation des ondes.

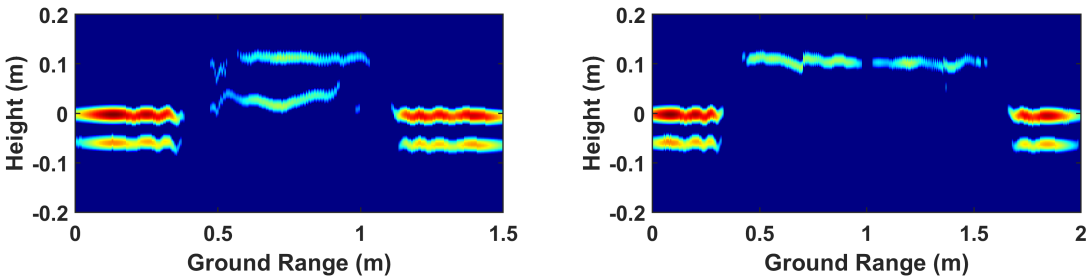

(a) Fissure verticale **(b)** Fissure horizontale

FIGURE 5 – Illustration de l'imagerie à haute résolution au chapitre 5

Le Chapitre 5 se focalise sur les techniques d'imagerie à haute résolution, mettant l'accent sur l'estimation spectrale pour rehausser la précision de l'imagerie dans le diagnostic des chaussées. Des techniques telles que le lissage spectral sont introduites pour réduire la corrélation des données. L'application de méthodes de sous-espace à haute résolution au GPR et au SAR bistatique coulissant est explorée, dans le but d'améliorer les capacités

de discrimination des fissures intégrées. Les résultats démontrent des améliorations significatives, confirmant l'efficacité des méthodes à haute résolution et soutenant davantage la viabilité du SAR bistatique coulissant pour l'inspection des chaussées.

Chapitre 1

Introduction

Contents

1.1 Context and motivation 17

1.2 Microwave monitoring techniques 19

1.2.1 Non destructive testing - GPR 19

1.2.2 Remote sensing techniques - SAR 20

1.3 Thesis contributions and outline 21

1.1 Context and motivation

ACIMP project

The French national roadway network spans over one million kilometers, including 11,000 kilometers of highways, constructed with the multi-layer flexible pavement structure, as shown in Fig. 1.1, making it a critical component of the country's transportation infrastructure [Dat23]. To ensure the safety of all users, regular and meticulous maintenance of these roads is imperative. This maintenance encompasses a diverse range of tasks aimed at preserving road integrity and quality [SS00 ; IDR14].

The ACIMP project, known as the improvement of knowledge of complex media composed of cracks and multiparameter inversion, has been thus established and funded by the French National Research Agency (ANR). Its primary objective is to improve the early detection of embedded defects within the pavement infrastructure, enabling precise localization and detailed geometric characterization through the application of microwave monitoring techniques. Within the framework of this project, this study aims to innovatively apply Ground-Based Synthetic Aperture Radar (GB-SAR) to pavement diagnosis and focuses on the methodological developments of 3-D tomographic imaging. This work brings together the collaboration of the Institut d'Electronique et des Technologies du

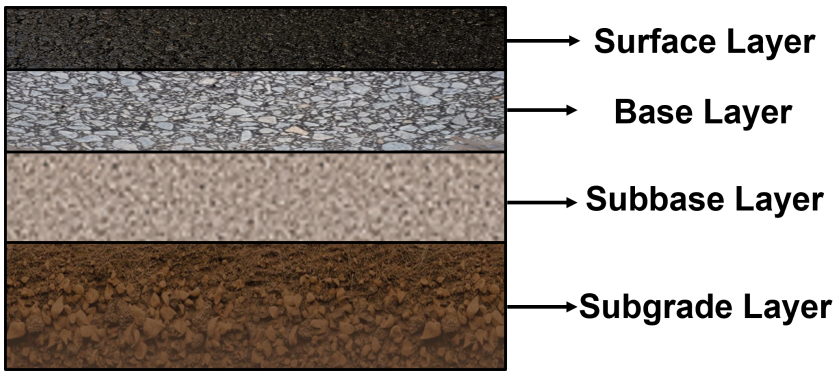

FIGURE 1.1 – Flexible Pavement structure

numéRique (IETR), Université Gustave Eiffel (UGE), ICAM OUEST, and Cerema Direction Territoriale Ouest, collectively striving to advance the field of pavement structural characterization and maintenance.

Background and motivation

An important aspect of road maintenance involves the thorough examination of embedded cracks. This process serves a dual purpose : measuring the thickness of these coatings and detecting and monitoring any cracks that may have developed. Monitoring cracks is particularly crucial, as they can compromise the structural integrity of the road and pose a hazard to motorists. By systematically assessing and addressing these issues, road authorities can proactively maintain the road network's safety and longevity [SS00 ; BP15 ; Le 07].

France's ever-increasing traffic volume adds complexity to the task of road maintenance. This constant growth necessitates the periodic reassessment of road structure designs to accommodate higher loads and increased traffic flow. When new construction projects are received, the primary goal is to estimate the thicknesses of road components and verify whether they align with the stringent requirements outlined in the project specifications. This verification process is essential to ensuring that the completed infrastructure is robust, safe, and fit for purpose.

The detection, localization, and characterization of both horizontal and vertical embedded cracks hold paramount importance in formulating rigorous maintenance and management strategies. These structural irregularities serve as critical indicators of a material's degraded state, leading to a notable reduction in the pavement's operational lifespan. Understanding the precise geometric parameters of these defects—encompassing

their morphology, dimensions, and depth of occurrence—alongside a comprehensive analysis of Electromagnetic (EM) characterization of permittivity, permeability attenuation, scattering coefficient [Ado06], are pivotal metrics for gauging the structural integrity and durability of these systems. This diagnostic approach not only facilitates the precise localization of potential pathologies within the structure but also enables a rigorous assessment of its overall health. Furthermore, it empowers accurate prognostications regarding its future evolution, thereby augmenting the efficiency of decision support tools in structural maintenance and management.

For the effective and sustainable maintenance of the extensive French road network, it is imperative to achieve early detection, precise location, and accurate geometric characterization of these defects. The early identification of thin (horizontal or vertical) cracks remains a persistent challenge due to the minuscule thicknesses of voids resulting from such cracks. This challenge holds significant importance for end-users, including clients and awarding authorities, as it enables the optimization of road structure maintenance once these defects are identified at an early stage.

Microwave radar devices using Non-Destructive Testing (NDT) and remote sensing techniques have proven to be valuable sensors for detecting and characterizing subsurface features. Ground Penetrating Radar (GPR), a prominent NDT tool, plays a pivotal role in this domain. It employs high-frequency electromagnetic waves to probe the subsurface, providing detailed information about the condition of the pavement layers and potential defects. Additionally, Synthetic Aperture Radar (SAR) technology, a form of remote sensing, significantly contributes to pavement assessment. SAR-equipped satellites and aircraft capture high-resolution images of the Earth's surface, enabling the detection of deformations, surface roughness, and other critical features. These approaches ensure the early detection and accurate characterization of structural anomalies, ultimately enhancing the longevity and safety of road networks.

1.2 Microwave monitoring techniques

1.2.1 Non destructive testing - GPR

In the field of civil engineering, GPR has been a widely utilized NDT method for assessing road pavement structures and quality since the 1970s [LDA18 ; Jol08 ; SPF21]. GPR instruments emit radio wave signals into a material and subsequently capture the

resulting echoes, which arise from alterations in material properties within the structure. These radio wave signals are predominantly brief pulses of EM energy. Notably, the GPR signal encompasses an extensive array of frequency components, typically spanning the 10–5000 MHz range. This characteristic prompts the classification of GPR instruments as Ultra-Wide Band (UWB) radio wave devices. The GPR signals manifest as electromagnetic EM waves, characterized by interlinked electric and magnetic fields that propagate through the material. Changes in the electric and magnetic attributes of the material lead to the scattering and reflection of these EM waves. Efficient techniques based on GPR acquisitions have been developed for characterizing complex underground media structures [SS00 ; Cha+07 ; Ras+20 ; Liu+23]. However, the detection and evaluation of small defects, such as thin horizontal or vertical cracks, remain a concerned challenge.

Conventional signal processing methods, like the widely known Fast Fourier Transform (FFT) and cross-correlation-based methods, face limitations in their ability to separate two echoes due to system frequency bandwidth [Le 07]. In fact, time resolution is closely related to the frequency bandwidth, denoted as B. The processing time resolution, for a given frequency bandwidth, is determined by the minimal time shift $\Delta\tau$ between two echoes that the processing can effectively distinguish. The product $B\Delta\tau$ characterizes the time resolution capability. The classical FFT-based methods can successfully resolve two echoes when their $B\Delta\tau$ product is greater than 1 [Kay88]. Advanced signal processing methods offer the important potential to retrieve high-precision vertical information of $B\Delta\tau < 1$ and estimate the structural properties of observed roadways [Sun+22 ; Sun+18 ; Le +14 ; Pan+21 ; Sun+19 ; Le +19].

1.2.2 Remote sensing techniques - SAR

Synthetic Aperture Radar (SAR), a remote sensing technique, has also found applications in monitoring pavement and infrastructure conditions [Ozd+16 ; MAH20 ; KM20]. SAR imaging is a sophisticated signal processing technique that leverages spatial and spectral diversities to synthesize a detailed 2-D map, offering insights into the reflectivity of a given scene [Sou99 ; FP16a]. The operation of SAR imaging primarily involves a side-looking configuration, enabling the estimation of vital geophysical parameters like roughness and humidity using various diversity modes [UMF81 ; FP16b].

The advent of SAR in the late 1980s marked a significant leap forward in remote sensing capabilities. These SAR systems offered the capacity to observe vast expanses with high precision, providing a complementary perspective to optical imagery. Through the

analysis of measured electromagnetic images, it became possible to discern the influence of various physical parameters within the observed scene. Techniques such as detection, classification, and radiometric identification were employed to dissect these parameters. As the 1990s unfolded, the advent of multichannel SAR sensors further expanded this capability, enabling the acquisition of multidimensional electromagnetic images. This, in turn, allowed for more precise estimation of characteristics pertaining to both environments and objects. The realm of SAR remote sensing swiftly found applications in a multitude of fields including geology, hydrology, agriculture, forestry, oceanography, snow and ice studies, land cover and elevation mapping, urban planning, volcanology, as well as disaster prediction and management.

To enhance the vertical resolution and overcome the inherent cylindrical ambiguity, the Tomographic SAR (TomoSAR) technique has emerged as a powerful solution [RM00 ; KS01]. It empowers the estimation of the 3-D reflectivity of environments, offering a more comprehensive understanding of complex scenes. TomoSAR leverages the acquisition of multi-baseline interferometric SAR data from subtly shifted trajectories [RM00 ; FHP16a ; FP16b], which are then coherently integrated to generate detailed 3-D images. By merging multi-baseline data, it uncovers the intricate topography and composition of diverse terrains. Its application has proven invaluable in investigating diverse 3-D media, including snow [Rek+17 ; Fre+17], ice [Yit+17 ; Teb+16], and forest [TR12 ; HFR12 ; Agh+20 ; HZF21].

Unlike traditional SAR systems mounted on aircraft or satellites, GB-SAR, operating from a fixed terrestrial position, represents a significant advancement in near-range imaging. This innovative approach offers distinct advantages, including the ability to capture high-resolution images and monitor surface movements with exceptional precision. GB-SAR systems utilize a sophisticated combination of radar technology and signal processing techniques, allowing for detailed assessments of various environments. Practical studies have utilized GB-SAR in conjunction with tomographic imaging to explore detailed structural properties [Fre+17 ; Yit+16 ; Yit+17 ; Rek+17 ; Abd+21 ; Har+20].

1.3 Thesis contributions and outline

The core objective of this thesis revolves around the comprehensive characterization of embedded defects and the precise estimation of their geometrical attributes in early pavement monitoring. This research focuses on the methodological developments of 3-D

tomographic imaging using GB-SAR in pavement inspection. The thesis introduces two bistatic GB-SAR configurations, which have been rigorously scrutinized through theoretical analysis and experimental validation, and benchmarked against the established GPR approach. The results demonstrate the distinct advantages of the proposed approaches in characterizing embedded cracks and estimating the electromagnetic properties of flexible pavements. This seminal contribution not only addresses current challenges but also lays the foundation for future advancements in the realm of pavement inspection and diagnosis.

The organization of the thesis is as follows :

— Chapter 2 provides a comprehensive introduction of SAR imaging techniques, from radar principles, to advanced range (1-D) focusing and multidimensional (2-D, 3-D) imaging techniques. The fundamental explanation of radar mechanisms covers the propagation of EM waves, and presents a simplified model for the signals acquired by radar systems. The concept of one-dimensional (1-D) range focusing is then elucidated, employing spectral diversity and drawing comparisons with commonly used pulse and continuous waveforms. The discussion progresses to encompass two-dimensional (2-D) SAR imaging techniques, emphasizing the significance of spatial diversity. The chapter culminates in an exploration of TomoSAR through the utilization of multi-baseline data, enabling the estimation of three-dimensional (3-D) reflectivity profiles of environments. This theoretical overview serves as a foundational framework for understanding and implementing advanced SAR methodologies.

— Chapter 3 presents a forward-scattering (FSC) bistatic tomographic SAR configuration, and investigates its performance with a variety of radar imaging modes, such as nadir-looking B scans, or back-scattering (BSC) TomoSAR, for the inspection and characterization of roadways. The comparison is led by evaluating the ability of each configuration, to discriminate and characterize shallow underground defects in the subsurface of roadways. Campaign measurements are conducted using short-range radar at the pavement fatigue carousel over debonded areas with artificial defects. Results indicate the great potential of the newly proposed forward scattering side-looking tomographic configuration for characterizing light defects, and estimating key geophysical parameters, such as roughness and dielectric permittivity. The relevant content has been published in [WFW21 ; Fer+22 ; Wu+23b].

— Chapter 4 takes one step further based on the previous chapter and presents a new sliding FSC configuration for roadway inspection, reducing the complexity to minimal level through the utilization of a single pair of opposite side-looking Tx and

Rx antennas, sliding along the ground-range direction. This configuration achieves good horizontal discrimination by exploiting the created angular aperture, while maintaining a constant vertical resolution. An experiment is performed with asphalt samples and artificial horizontal and vertical cracks. Results demonstrate the potential of the proposed sliding bistatic SAR mode as a valuable alternative to classical ground penetrating radar for roadway monitoring. A part of the content in this chapter has been presented in [Wu+23a] and selected for the EURAD Prize Finalist.

— Chapter 5 delves into high-resolution imaging techniques centered on spectral estimation, and its application to COSBis configuration, aiming to enhance imaging accuracy in roadway diagnosis. The integration of COSBis configuration with high-resolution techniques makes a promising improvement in subsurface inspection. This approach demonstrates substantial potential in characterizing both horizontal and vertical cracks, delivering more accurate representations of subsurface features.

Chapitre 2

Principles of SAR imaging

Contents

2.1 Introduction 25
2.2 Principle of a coherent radar system 26
2.2.1 Objectives of a coherent radar measurement 26
2.2.2 Signal model of radar responses 26
2.3 Range focusing techniques 28
2.3.1 Radar waveforms 29
2.3.2 Range focusing 32
2.4 2-D SAR imaging techniques 36
2.4.1 Geometry a SAR measurement 37
2.4.2 2-D SAR focusing 39
2.4.3 Properties of focused signal in azimuth 45
2.5 TomoSAR imaging techniques 46
2.5.1 Tomographic SAR geometry 46
2.5.2 3-D tomographic focusing 48
2.6 Conclusion 50

2.1 Introduction

This chapter gives an introduction to some advanced techniques and theoretical basis of Synthetic Aperture Radar (SAR), which are based on [FP16a ; Fer13]. First, the fundamental concept of radar mechanism is presented, including the propagation of EM waves and a simple model for a signal measured by a radar system. Subsequently, the principle of one-dimensional (1-D) range focusing is discussed by using spectral diversity and compared by exploiting common used pulse and continuous waveforms. Two-dimensional (2-D) SAR imaging techniques are then introduced by using the spatial diversity. By

using multi-baseline, tomographic SAR (TomoSAR) is employed to estimate the three-dimensional (3-D) reflectivity of environments in the end.

2.2 Principle of a coherent radar system

2.2.1 Objectives of a coherent radar measurement

In Fig. 2.1, the underlying principle governing active radar measurements is elucidated. A radar system emits an electromagnetic (EM) wave that traverses a defined spatial domain, probing the response of an obstructing entity, denoted as a target or scatterer. The analysis of the received signal, $s_r(\tau)$, affords the means to infer various geophysical attributes pertaining to the illuminated object. Notably, one can ascertain its EM reflectivity based on the energy content of the acquired signal. The determination of radar-target distance, contingent on the propagation time for the wave to complete a round trip from the radar to the target and back, is achievable through this analysis [FP16a ; Sko08].

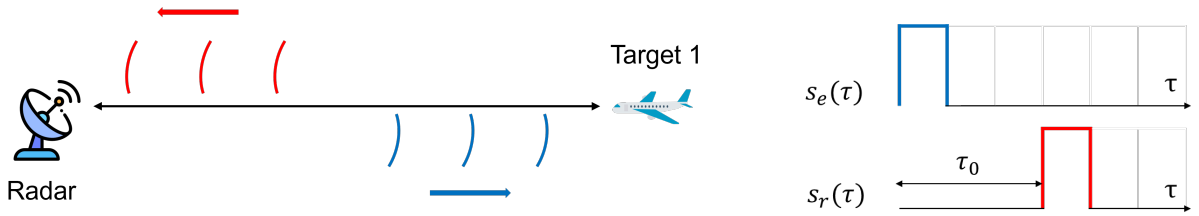

FIGURE 2.1 – Principle of a radar measurement, with $s_e(\tau)$ being the emitted signal and $s_r(\tau)$ being the response of an object

As demonstrated below, leveraging fundamental physical principles concerning the propagation of electromagnetic waves and their interaction with matter enables us to articulate a simple and versatile expression for the radar-received signal. This expression can serve as a foundational model for synthesizing electromagnetic images.

2.2.2 Signal model of radar responses

The general schematic representation of a coherent radar system, which measures signal phase, is depicted in Figure 2.2 [Fer13 ; Sko08]. The baseband waveform $u(\tau)$ employed by the radar undergoes transposition, achieved through multiplication or mixing with the carrier signal, $\exp(j\omega_c\tau)$, within the radio frequency (RF) spectral domain centered around the pulsation ω_c. Following amplification of the modulated signal $p(\tau)$, the

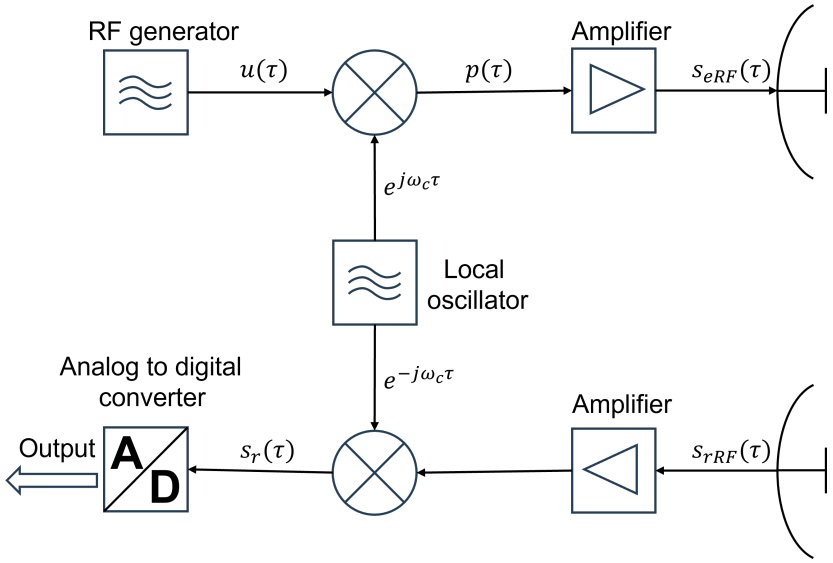

FIGURE 2.2 – Synopsis of a coherent radar system

emitted RF signal, $s_{e_{RF}}(\tau)$ is transformed into an EM field and transmitted by the emitting antenna. he receiving antenna then captures and converts the field scattered by the observed scene into an RF signal $s_{r_{RF}}(\tau)$, which is subsequently transposed into the baseband using the conjugate carrier signal. This process retrieves the received signal $s_r(\tau)$, that is then digitized and stored before processing. The fundamental parameters of a coherent radar system encompass the carrier frequency, employed waveform, antenna system configuration, and the received signal quality, often assessed by Signal-to-Noise Ratio (SNR).

A radar conventionally entails co-located emission and reception, where waves are both emitted and received at the same physical location, effectively acting as a monostatic acquisition. The emitted spherical wave propagates from position $\mathbf{r}_0$ through a non-dispersive medium at a velocity $c = \frac{\omega_c}{k_c} = \frac{1}{\sqrt{\mu_0 \varepsilon_0}}$. To address the complexity of the signal expressions, a typical free-space scene without loss of generality is considered, comprising a set of N_s point targets with non-dispersive reflectivity within the considered band. After coherent demodulation, the received baseband signal is expressed as

$$s_r(\tau) = \sum_{i=1}^{N_s} a_{c_i} u\left(\tau - \tau_i\right) \exp\left(-j\omega_c \tau_i\right) \text{ with } \tau_i = \frac{2d_i}{c}, d_i = \|\mathbf{r}_0 - \mathbf{r}_i\| \tag{2.1}$$

where a_{c_i} denotes the complex scattering amplitude related to the Radar Cross Section (RCS) of the i th illuminated target, with corresponding distance d_i and delay τ_i. The

goal of radar measurements lies in the inversion of this linear model, in order to estimate the equivalent reflectivity a_{c_i} and the radial position d_i of each target [Sou99].

The response from a scene consisting of a continuum of non-separable scatterers is characterized by employing a coherent reflectivity density, rather than relying on a collection of point-like contributions. The model of the received signal is expressed as

$$s_r(\tau) = \int_W a_c(\mathbf{r}')\, u(\tau - \tau') \exp(-j\omega_c \tau')\, J(d', \tau')\, \mathrm{d}V' \text{ with } \tau' = \frac{2d'}{c} \text{ and } d' = \|\mathbf{r}_0 - \mathbf{r}'\| \tag{2.2}$$

Here, $a_c(\mathbf{r}')$ represents the equivalent coherent reflectivity density, measured in the illuminated heterogeneous volume V' ,W and $J(d', \tau')$ is the Jacobian relative to the transformation of distance into time. The utilization of the discrete model $a_c(\mathbf{r}) = \sum_{i=1}^{N_s} a_{c_i} \delta(\mathbf{r} - \mathbf{r}_i)$ make (2.2) a more general expression than (2.1).

In contrast, distributed media and individual point scatterers display disparate statistical behaviors. The response of a point scatterer, exemplified by a calibration target, adheres to deterministic principles. Within distributed environments, a vast number of scatterers possess electromagnetic traits that are largely independent. The superposition of the different contributions of scatterers introduces an element of randomness into $a_c(\mathbf{r})$, commonly referred to as speckle. According to the central limit theorem, which applies to homogeneous environments, $a_c(\mathbf{r})$ conforms to a circularly complex Gaussian distribution, characterized with zero mean and variance $\sigma_a^2(\mathbf{r})$. And $a_c(\mathbf{r})$ is generally regarded as white distributed, comprising uncorrelated spatial samples at the scale of analysis.

2.3 Range focusing techniques

In a simplified scenario where a scene contains only a single target with $N_s = 1$, employing a monochromatic wave described by $u(\tau) = 1$, this case results in a consistent received signal, denoted as $s_r(\tau) = a_{c_1} \exp(-j\omega_c \tau_1)$. This setup allows for the estimation of the magnitude of a_{c_1}. but falls short in accurately determining τ_1. This limitation arises from the condition $\omega_c \tau_1 \gg 2\pi$ and the fact that $a_{c_1} \in \mathbb{C}$. To overcome this challenge, an effective solution is to introduce spectral diversity through a polychromatic waveform $u(\tau) = \exp(-j\Delta\omega\tau) + \exp(+j\Delta\omega\tau)$. The evident spectral seperation in the received signals, denoted as $s_{r_{\pm\Delta\omega}}(\tau)$, allow for the formulation of a dual complex equation system. This enables the unambiguous identification of both a_{c_1} and τ_1, provided the spectral deviation remains sufficiently small $\Delta\omega\tau_1 < \pi$. When dealing with an arbitrary number

of sources N_s, the parameter pairs (a_{c_i}, τ_i) can be accurately approximated by utilizing a wide range of appropriately selected frequency components. his requires the use of a waveform $u(\tau)$ with a bandwidth B_f, tailored for the analysis of the observed scene.

2.3.1 Radar waveforms

The waveforms employed to generate the requisite frequency diversity for distinguishing multiple targets can be broadly categorized into pulsed and continuous waveforms.

Pulsed Waveform

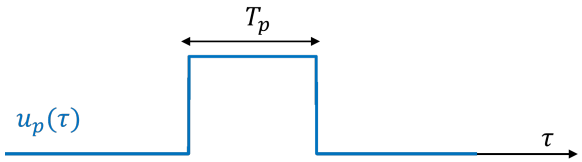

(a) Classical pulse

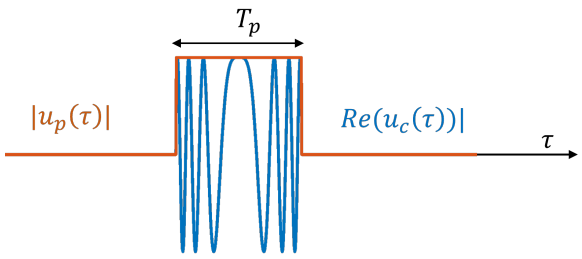

(b) Chirp pulse

FIGURE 2.3 – Examples of pulsed radar waveforms

As illustrated in Fig. 2.3, two pulsed waveforms, denoted as $u_p(\tau)$ and $u_c(\tau)$, are characterized by a finite temporal extent, with a duration of T_p, which is significantly shorter than the time taken for the wave to traverse the distance between the radar

transmitter and the target object. These waveforms are mathematically defined as

$$\begin{aligned} u_p(\tau) &= \text{rect}\left(\frac{\tau}{T_p}\right) \\ u_c(\tau) &= \text{rect}\left(\frac{\tau}{T_p}\right) \exp\left(j\pi\alpha\tau^2\right) \end{aligned} \tag{2.3}$$

where $\alpha = \frac{B_f}{T_p}$ indicates the chirp slope. The waveform $u_p(\tau)$ is a classical pulse, whereas $u_c(\tau)$ is a the chirp pulse modulated linearly in frequency. These waveforms, characterized by finite durations, can be directly applied to the radar response models presented in equations (2.1) and (2.2). The expressions for the radar impulse response of these waveforms are

$$\begin{aligned} h_p(\tau) &= T_p \,\text{tri}\left(\frac{\tau}{2T_p}\right) \\ h_c(\tau) &\approx T_p \sin(B_f\tau) \end{aligned} \tag{2.4}$$

with $\text{tri}(x)$ represents the triangular function with unitary amplitude.

The waveform $u_p(\tau)$ possesses a bandwidth determined by $\frac{1}{T_p}$, whereas $u_c(\tau)$, with instantaneous frequency $f = \alpha\tau$, hexhibits a spectrum given by

$$U_c(f) \approx \text{rect}\left(\frac{f}{B_f}\right) \exp\left(j\pi\frac{f^2}{\alpha}\right) \tag{2.5}$$

where the width is defined by $B_f = \Delta f = \alpha T_p$, provided $\Delta f T_p \geq 200$ [CW05].

Continuous Waveform

Unlike pulsed waveforms, Continuous Waveforms (CW) are defined in the spectral domain, as depicted in Fig. 2.4. It represents signals characterized by a constant amplitude throughout time, and a frequency that changes either gradually or discretely [Sko08 ; Fer13 ; Sou99], and an overview of a CW radar system is illustrated in Fig. 2.5.

Stepped Frequency CW (SFCW) radar systems capture the sustained response of a scene using monochromatic (sinusoidal) signals, typically at discrete frequency values, akin to measurements made by a Vector Network Analyzer (VNA). The Frequency Modulated CW (FMCW) technique extends this approach into a continuous system, achieved by a deliberate slow sweep over a duration T_r across a predefined spectral domain.

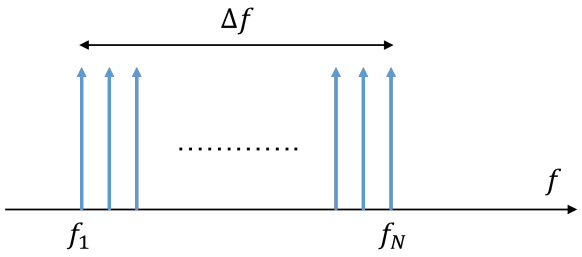

(a) Stepped frequency continuous waves

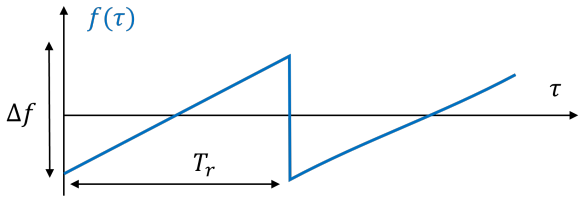

(b) Frequency modulated continuous waves

FIGURE 2.4 – Examples of continuous radar waveforms

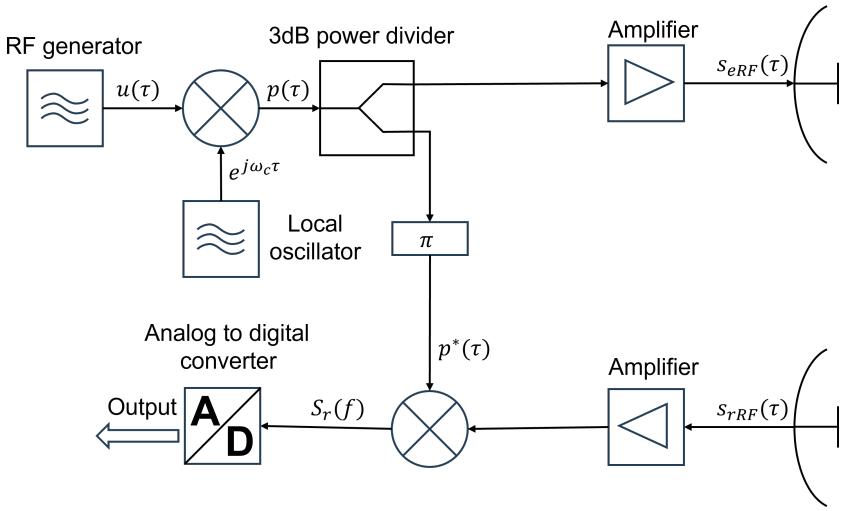

FIGURE 2.5 – Synopsis of a CW radar

The spectrum of two waveforms can be expressed as

$$\begin{aligned} U_{\mathrm{SFCW}}(f) &= \sum_{n=1}^{N_f} \delta(f - f_n) \\ U_{\mathrm{FMCW}}(f) &= \delta(f - f(\tau)) \end{aligned} \tag{2.6}$$

with the corresponding radar impulse response approximately given by

$$h_{\mathrm{FMCW}}(\tau) \approx h_{\mathrm{SFCW}}(\tau) = \frac{\sin(\pi N_f df \tau)}{\sin(\pi df \tau)} \tag{2.7}$$

with $\Delta f = N_f df$ in the case of CW signals. In contrast to the pulsed approach, the CW measurement mode, relying on slow measurements across an equivalent spectral range, enables the synthesis of temporal waveform $u_{SFCW}(\tau)$ and $u_{FMCW}(\tau)$ that can be assimilated to impulses, with reduced material complexity.

2.3.2 Range focusing

Principle of range focusing

In the presence of acquired noise and for a discrete scene, the received signal from the radar can be characterized as

$$s_r(\tau) = \sum_{i=1}^{N_s} a_{c_i} u(\tau - \tau_i) \exp(-j\omega_c \tau_i) + n(\tau) = s_{r_u}(\tau) + n(\tau) \tag{2.8}$$

with $s_{r_u}(\tau)$ represents the useful component of the received signal, while $n(\tau)$ denotes white noise within the utilized frequency band, centered and with variance σ_n^2.

The capacity of a radar system to differentiate and identify various targets is generally assessed through its range resolution and the SNR of the received signal, as depicted in Fig. 2.6b.

The resolution of an imaging system is its ability to discern responses from scatterers situated in nearby positions. In the context of Fig. 2.6b, object responses can be distinguished if $\Delta\tau = |\tau_1 - \tau_2| > T_p$. The range resolution, defined as the minimal range between two targets, is therefore given by

$$\delta d = \frac{cT_p}{2} \tag{2.9}$$

However, range ambiguity may arise, as depicted in Fig. 2.6c, when employing bursts

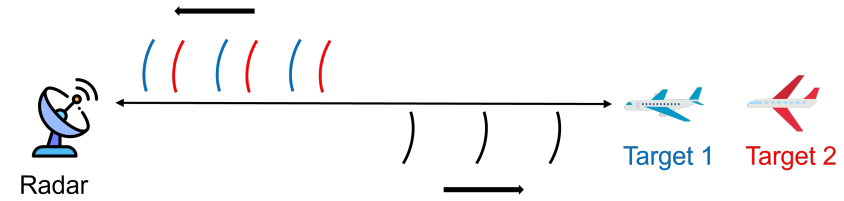

(a) Geometry of detecting multi targets

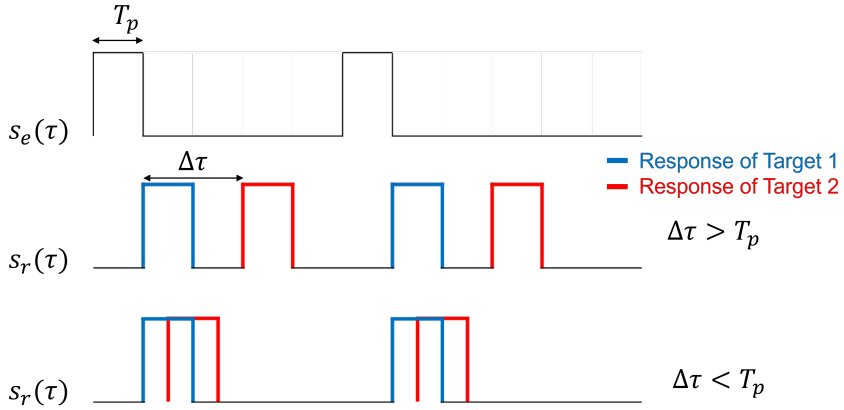

(b) Illustration of range resolution

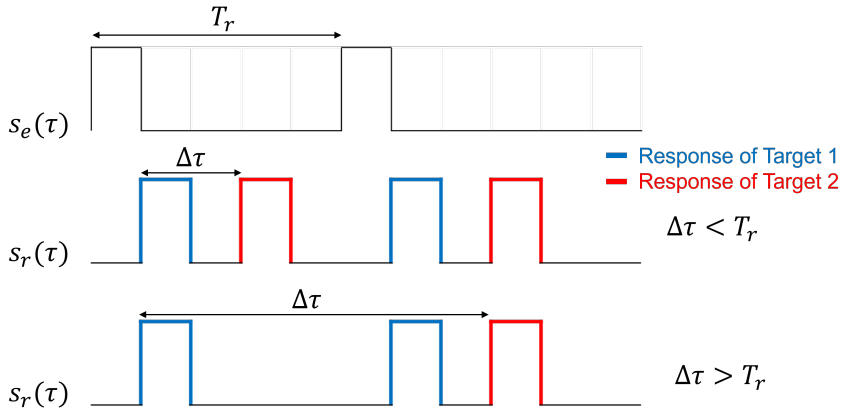

(c) Illustration of range ambiguity

FIGURE 2.6 – Illustration of range resolution and ambiguity in detecting multi targets

of pulses emitted periodically with an interval of T_r, in the case of $\Delta\tau > T_r$. The system is capable of estimating the true relative distance Δd, only if this value is less than the ambiguity distance given by

$$d_{amb} = \frac{cT_r}{2} \tag{2.10}$$

Range focusing of the measured signal serves to concentrate a scatterer's response around its temporal abscissa τ_i and enhance the SNR at this position, ultimately providing a reliable estimate of the reflectivity $|a_{c_i}|$. This process is generally implemented in the form of linear filtering of the received signal, applicable to both discrete and distributed scenes. The focused signal is expressed as

$$s_{rf}(\tau) = s_r(\tau) * g_r(\tau) \tag{2.11}$$

with the convolution operator $*$ and the focusing filter $g_r(\tau)$. The model given in (2.8), indicates that focusing can be interpreted as the localization and estimation of a signal with a known form $u(\tau)$, embedded in noise. The expression of the range focused signal is given, with the adapted filter $g_r(\tau) = u^*(-\tau)$ leading to an optimal SNR, by

$$\begin{aligned} s_{rf}(\tau) &= s_r(\tau) * u^*(-\tau) \\ &= \int_{-\infty}^{-\infty} s_r(\tau')\, u^*(\tau' - \tau)\, d\tau' \\ &= \sum_{i=1}^{N_s} a_{c_i} h(\tau - \tau_i) \exp(-j\omega_c \tau_i) + n_f(\tau) \end{aligned} \tag{2.12}$$

where $n_f(\tau)$ represents the filtered noise. The function $h(\tau) = u(\tau) * u^*(-\tau)$, referred to as the radar impulse response, peaks at $\tau = 0$ and defines the properties of the focused signal.

A simple physical interpretation of range focusing can be provided using (2.8) and (2.12). The spectrum of useful signal before $S_{r_u}(f)$, and after focusing by adapted filtering $S_{rf_u}(f)$, are expressed as

$$\begin{aligned} S_{r_u}(f) &= U(f) \sum_{i=1}^{N_s} \tilde{a}_{c_i} \exp(-j2\pi f \tau_i) \\ S_{rf_u}(f) &= S_{r_u}(f) U^*(f) = H(f) \sum_{i=1}^{N_s} \tilde{a}_{c_i} \exp(-j2\pi f \tau_i) \end{aligned} \tag{2.13}$$

with $\tilde{a}_{c_i} \triangleq a_{c_i} \exp(-j2\pi f_c \tau_i)$ and $H(f) = |U(f)|^2$, the Fourier transform of $h(\tau)$. In the frequently encountered case of a signal with a flat spectrum and a bandwidth B_f, the measured reflectivity density is reconstructed by adapted filtering as

$$\begin{aligned} U(f) &= \text{rect}\left(\frac{f}{B_f}\right) \exp(-j\varphi(f)) \\ \Rightarrow s_{rf_u}(\tau) &= \sum_{i=1}^{N_s} \tilde{a}_{c_i} h(\tau - \tau_i) \\ &= \sum_{i=1}^{N_s} \tilde{a}_{c_i} B_f \,\text{sinc}(B_f(\tau - \tau_i)) \end{aligned} \tag{2.14}$$

with $sinc(x) \triangleq \frac{\sin(\pi x)}{\pi x}$ and $\varphi(f)$ represents an arbitrary phase law. It turns out from (2.14) that as $B_f \to +\infty$, $h(\tau) \to B_f \delta(\tau)$ and the focused signal perfectly reconstructs the equivalent reflectivity density, $s_{rf_u}(\tau) \propto \tilde{a}_c(\tau)$. In cases where the bandwidth is finite, the reconstruction is approximated using the function $h(\tau)$, whose concentration improves with an increase in bandwidth.

Properties of focused signal with Continuous waveform

Adapted filtering can be implemented either in the time domain (2.12) or in the spectral domain (2.13). In the case of CW signals, the focusing process involves a straightforward Fourier transform of the received signal after demodulation by the transmitted signal, and the recorded demodulated signal corresponds to the spectrum of the range-focused response $S_{rf}(f)$.

The focused CW signals share similarities with $h_c(\tau)$ in the vicinity of $\tau = 0$, exhibiting comparable temporal resolution, $\delta\tau = \frac{1}{B_f}$, which aligns with the width of the main lobe of $h_c(\tau)$ at $-3\ dB$. However, one may note that the CW impulsion responses possess a periodic characteristic, with $|h_{CW}(\tau + \tau_{amb})| = |h_{CW}(\tau)| \,\forall\tau$ and $\tau_{amb} = \frac{1}{d_f}$. This feature, originating from the definition of the CW signal in the spectral domain, enforces an unambiguous condition for spatial differentiation, as indicated by

$$\Delta d < \frac{c\tau_{amb}}{2} \tag{2.15}$$

The distinctive characteristics and limitations of each waveform with respect to range focusing applications are succinctly summarized in Table 2.1. This table underscores the contrasting performance between simple pulse waveforms and their counterparts, arising

from the concurrent enhancement of resolution, resulting in conflicting constraints regarding pulse duration T_p.

Wave Form	Classical pulse	Chirp pulse	SFCW	FMCW
Resolution δd	$\frac{cT_p}{2}$	$\frac{c}{2B_f} = \frac{c}{2\alpha T_p}$	$\frac{c}{2B_f} = \frac{c}{2N_f d_f}$	$\frac{c}{2B_f} = \frac{c}{2\alpha T_r}$
Sampling	$f_s \geq \frac{1}{T_p}$	$f_s \geq B_f$	$N_f \geq \frac{\Delta d}{\delta d}$	$f_s \geq \frac{\Delta d}{T_r \delta d}$

TABLE 2.1 – Characteristics of range focusing properties for different waveforms

The focused signal is generally represented as a function of the spatial coordinate $d = \frac{c\tau}{2}$ and two-way wavenumber $k = \frac{4\pi}{\lambda}$, defined with the equivalence $\exp(j\omega\tau) = \exp(jkd)$. The expression of a focused signal for a distributed scene, made up of a large number of non-separable scatterers, is given by

$$s_{rf}(d) = \int_{-\infty}^{-\infty} a_c(d')\, h(d - d') \exp(-jk_c d')\, dd' + n_f(d) \tag{2.16}$$

In the case of discrete targets, the scene density of reflectivity is given by :

$$a_c(d) = \sum_{i=1}^{N_s} a_{c_i} \delta(d - d_i) \tag{2.17}$$

The resolution of radar measurements holds significant sway over the accuracy of estimations within such scenes. In practical terms, advanced spectral estimation methodologies, such as Capon, MUSIC, ESPRIT, etc., are frequently employed to further refine resolutions [Sun+19].

2.4 2-D SAR imaging techniques

SAR imaging stands as a well-established coherent microwave remote sensing technique, proficient in providing high-resolution 2-D images of environmental reflectivity over large areas. SAR systems find versatile applications across various platforms, including spaceborne systems for global remote sensing, airborne radars for adaptable geographic observations, and ground-based SAR (GB-SAR) systems known for their detailed and comprehensive characterizations.

The radar system's capability to distinguish scatterers based on their radial position facilitates its utilization in two primary modes. In a nadir-looking configuration, as illustrated in Fig. 2.7a, the radar conducts vertical measurements, enabling precise estimation of the vertical distribution and average elevation of the observed environment. The precision is contingent upon the system's distance resolution δd. For monitoring applications, the radar adopts a side-looking configuration, depicted in Figure 2.7b, mitigating ground-range ambiguities and naturally enhancing the differentiation of imaged regions through range focusing, with a ground-range resolution $\delta y \approx \frac{\delta d}{\sin\theta}$ determined by the local incident angle θ.

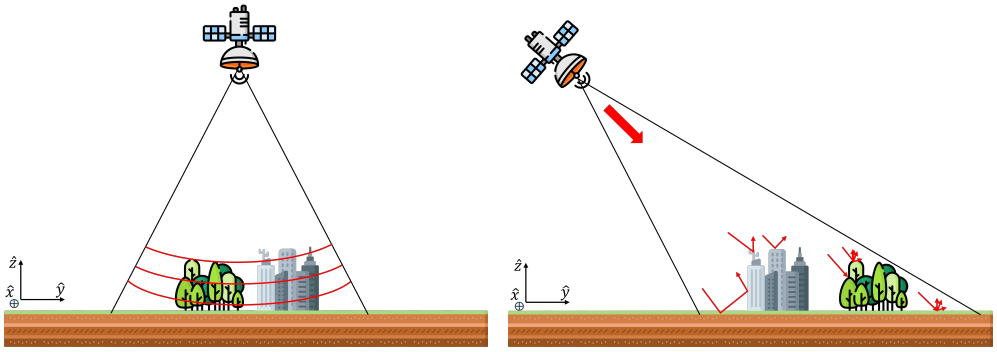

(a) Nadir-looking **(b)** Side-looking

FIGURE 2.7 – Observation modes of radar measurements

2.4.1 Geometry a SAR measurement

The antenna system employed in transmitting and receiving radar signals constitutes a crucial component of SAR measurements. In SAR, an antenna is characterized by its central operating frequency f_c, bandwidth B_f, and radiation pattern $G(\theta, \phi)$, which delineates its radiation characteristics in space. The co-localized transmitting and receiving antennas are assumed to possess a uniform radiation pattern within an aperture, described by

$$G(\theta, \phi) = G \,\mathrm{rect}\left(\frac{\phi}{\phi_a}\right) \mathrm{rect}\left(\frac{\theta}{\theta_a}\right) \tag{2.18}$$

where ϕ_a and θ_a are the apertures in azimuth and elevation, respectively. These apertures can be approximated using the physical dimensions of the antenna, L_ϕ and L_θ in the

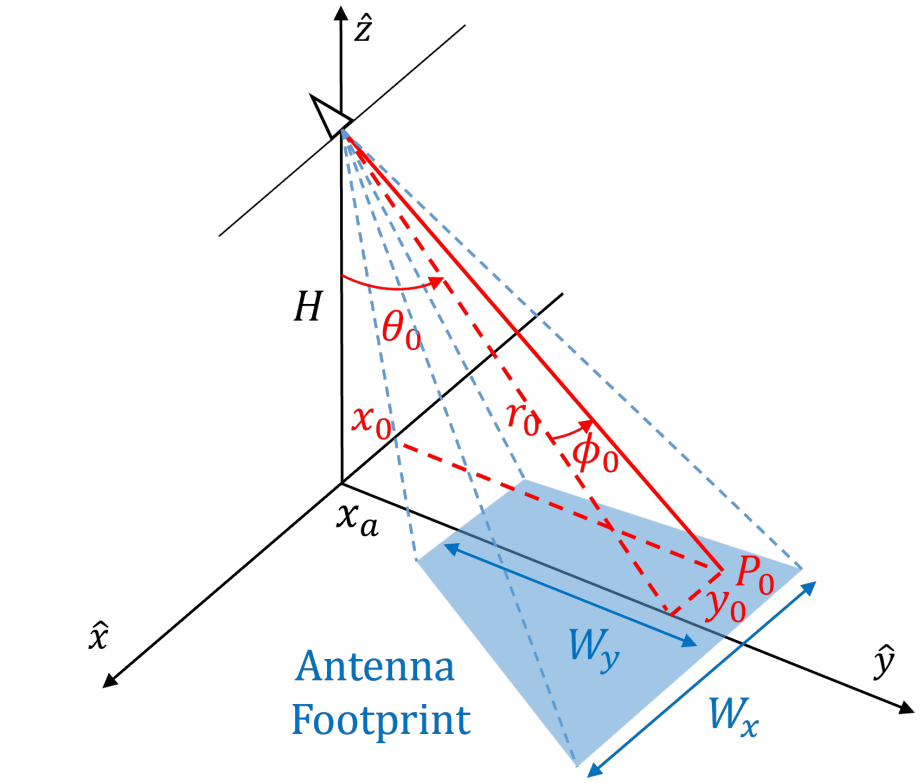

(a) Geometry of radar illumination area

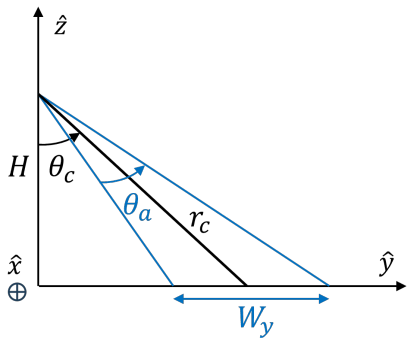

(b) Radar footprint
Ground range - elevation plane

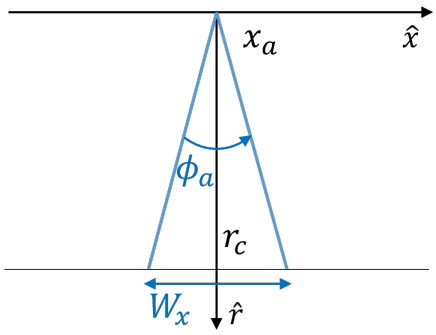

(c) Radar footprint
Azimuth - slant range plane

FIGURE 2.8 – Geometry of a side-looking measurement [FP16a]

azimuth and elevation, respectively, by

$$\phi_a \approx \frac{\lambda_c}{L_\phi}, \quad \theta_a \approx \frac{\lambda_c}{L_\theta} \tag{2.19}$$

where λ_c represents the wavelength of the carrier signal associated with the central frequency f_c, specifically $\lambda_c = \frac{c}{f_c}$.

Figure. 2.8 illustrates the geometrical configuration of a side-looking measurement, where the antenna is aligned with the azimuth axis $\hat{x}$. The radar's position is denoted by $(x_a, y_a = 0, z_a = H)$, while a point tagret is situated at (x_0, y_0, z_0), in Cartesian coordinates. The slant range r_0 and the corresponding angular coordinates (d_0, θ_0, ϕ_0) can be expressed as

$$\begin{aligned} r_0 &= \sqrt{(H - z_0)^2 + (y_a - y)^2} \\ d_0 &= \sqrt{r_0^2 + (x_a - x_0)^2} \\ \sin\phi_0 &= \frac{|x_a - x_0|}{d_0}, \ \sin\theta_0 = \frac{y_0}{r_0} \end{aligned} \tag{2.20}$$

A scatterer is illuminated by the radar within the effective antenna beam under the condition of $|\phi_0| \leq \frac{\phi_a}{2}$ and $|\theta_a - \theta_c| \leq \frac{\theta_1}{2}$, where θ_c represents the central incidence angle. The area encompassed by the antenna beam, known as the antenna footprint, has swaths of W_x and W_y in azimuth and ground range direction, respectively, and can be approximated by

$$\begin{aligned} W_x =& 2r_0 \tan\left(\frac{\phi_a}{2}\right) \approx r_0\phi_a \\ W_y =& H\left(\tan\left(\theta_c + \frac{\theta_a}{2}\right) - \tan\left(\theta_c - \frac{\theta_a}{2}\right)\right) \end{aligned} \tag{2.21}$$

2.4.2 2-D SAR focusing

The existing limitations in azimuth resolution present challenges when attempting to discriminate between two scatterers, denoted as P_1 and P_2, falling within the antenna footprint. Specifically, the constraint $|d_1(x_{a_0}) - d_1(x_{a_0})| < d_0$ holds, which implies that a single acquisition at position x_{a_0}. To address this critical limitation in azimuth resolution without the need for hardware modifications in the radar system, the approach of SAR measurements, leveraging azimuth spatial diversity, is a viable solution, as depicted in Fig. 2.9a.

As the radar moves along the $\hat{x}$ axis, the radar-target distances $d_i\,(x_a)$ follow distinct

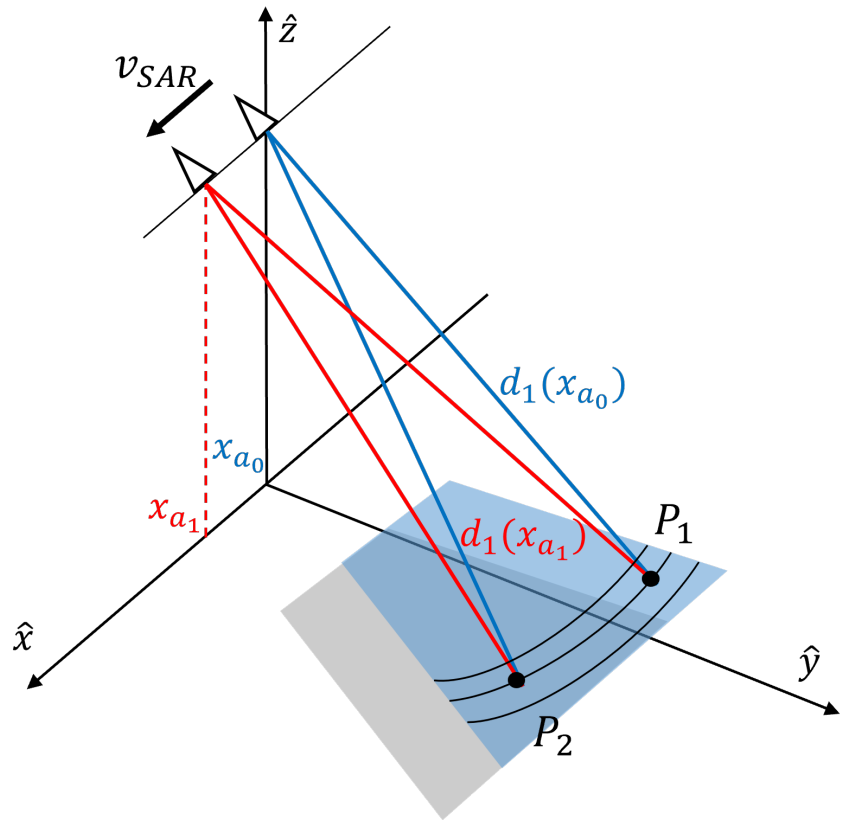

(a) Geometry of a SAR measurement

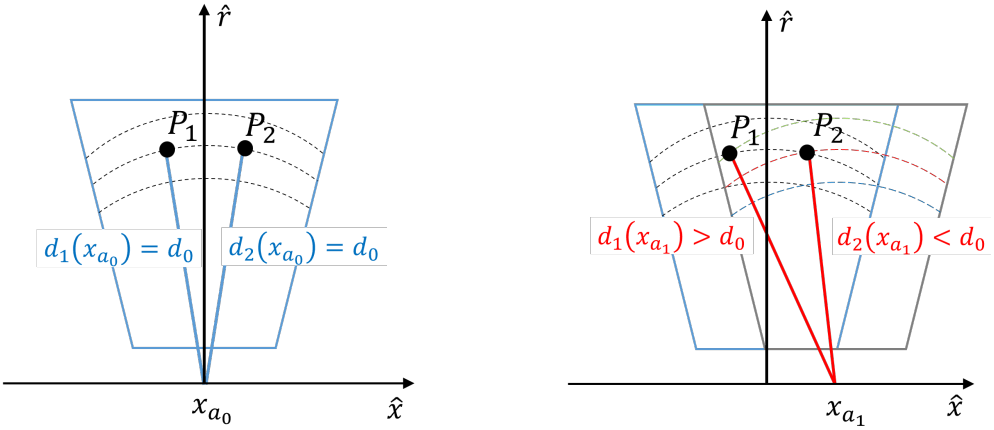

(b) Discrimination through spatial diversity in azimuth

FIGURE 2.9 – SAR measurement of multi scatterers [FP16a]

paths that facilitate the discrimination of the two responses, illustrated in Fig. 2.9b. By utilizing the expression for the range-focused target response for each measurement position x_a :

$$s_{rf_i}(x_a, d) = a_{c_i} h(d - d_i(x_a)) \exp(-jk_c d_i(x_a)) \operatorname{rect}\left(\frac{x_i - x_a}{w_x(r_i)}\right) \tag{2.22}$$

where rect $\left(\frac{x_i - x_a}{W_x(r_i)}\right)$ signifies that the target belongs to the illuminated zone, it becomes evident that differentiation can be accomplished in two distinct ways. The incoherent approach, as denoted by $|s_{rf_i}(x_a, d)| \propto |h(d - d_i(x_a))|$, permits the identification of $d_i(x_a)$ with a precision on the order of the range resolution δd. Alternatively, the coherent approach, relying on the term $\exp(-jk_c d_i(x_a))$, achieves a precision much finer than $d_i(x_a)$. The coherent approach estimates $d_i(x_a)$ through the term $\exp(-jk_c d_i(x_a))$, with a precision better than $\frac{\lambda_c}{2} \ll \delta d$.

Radar systems are typically installed on platforms that undergo continuous motion along the azimuth axis at a velocity represented by $\vec{v}_{SAR} = v_{SAR}\hat{x}$, as shown in Fig. 2.10. The emission of signals follows a regular pattern with a period denoted as $T_r = PRF^{-1}$, where PRF stands for Pulse Repeat Frequency, expressed in Hz. This measurement process can be viewed as a form of spatial sampling, characterized by an interval of $\mathrm{d}x = \frac{v_{SAR}}{T_r}$, assuming the radar system remains stationary both during the transmission and reception of signals.

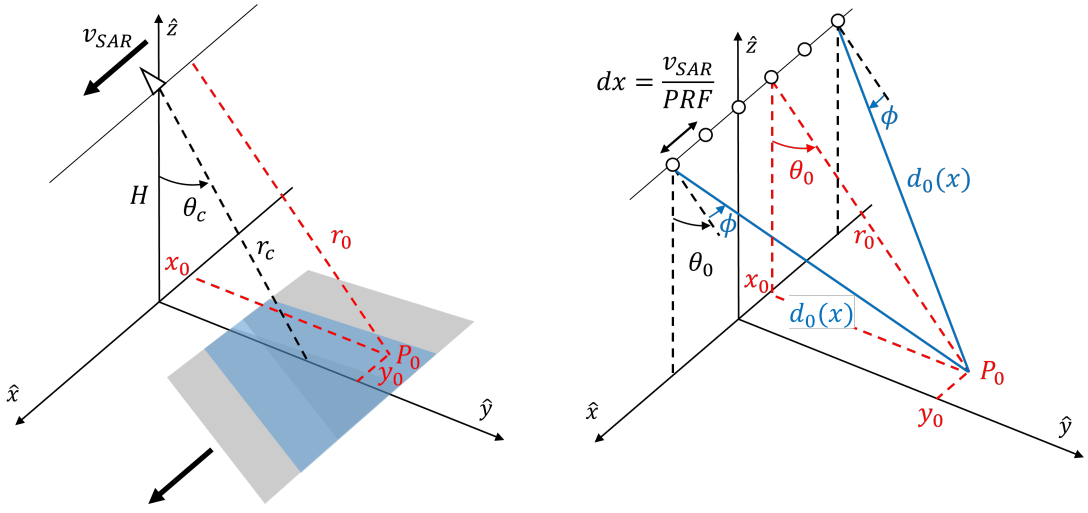

FIGURE 2.10 – Geometry of a rectilinear SAR measurement with regular sampling [FP16a]

The process of SAR imaging involves the utilization of a 2-D adapted filter to focus the measured receiving signal $s_r(x_a, \tau)$, leveraging both spectral and spatial diversity. This facilitates the construction of an observed scene, represented by the reflectivity distribution of $s_{arf}(x, r)$, relying on the response of an ideal scatterer. This ensures an optimal statistical character for the imaging operation.

he 2-D SAR response of a scatterer characterized by coordinates (x_0, r_0) and an equivalent complex reflectivity a_c is given by

$$s_r\left(x_a, \tau\right) = a_c \operatorname{rect}\left(\frac{x_0 - x_a}{W_x\left(r_0\right)}\right) \exp\left(jk_c d\left(x_a; x_0, r_0\right)\right) u\left(\tau - \frac{2d\left(x_a; x_0, r_0\right)}{c}\right) \tag{2.23}$$

where rect $\left(\frac{x_0 - x_a}{W_x(r_0)}\right)$ ensures the target belongs to the illuminated zone.

$d\left(x_a; x_0, r_0\right) = \sqrt{r_0^2 + \left(x_0 - x_a\right)^2}$ assumes constant propagation losses on the azimuth aperture, that is $d^2\left(x_a; x_0, r_0\right) \approx r_0^2$. This signal model can be expressed as a 2-D convolution product with respect to x and τ, denoted $*_{x,\tau}$, as

$$s_r\left(x_a, \tau\right) = a_c \exp\left(jk_c r_0\right) \delta\left(x - x_0\right) \delta\left(r - r_0\right) *_{x,\tau} u_{ar}\left(x, \tau; r_0\right) \tag{2.24}$$

where $u_{ar}\left(x, \tau; r_0\right)$ signifies the ideal response of a scatterer, and can be expressed as

$$u_{ar}\left(x, \tau; r_0\right) = \operatorname{rect}\left(\frac{x}{W_x\left(r_0\right)}\right) \exp\left(jk_c \tilde{d}\left(x; r_0\right)\right) u(\tau) \tag{2.25}$$

where $\tilde{d}\left(x; r_0\right) = d\left(x_a; 0, r_0\right) - r_0$ accounts for the varying distance between the radar and the target during the radar's motion along the azimuth axis.

The range focused signal at arbitrary coordinates (x, r) is derived by applying an adapted linear filtering to the ideal scatterer's response, represented as $s_{arf}(x, r) = s_r\left(x_a, \tau\right) *_{x,\tau} u_{ar}^*(-x, -\tau; r)$. The evaluation of the convolution operation according to τ leads to a simple expression of $s_{arf}(x, r)$ range focused by using $s_{rf}\left(x_a, d\right)$ as

$$s_{arf}(x, r) = \exp\left(-jk_c r\right) \int_{-\infty}^{+\infty} s_{rf}\left(x_a, d\left(x_a; r, x\right)\right) \exp\left(jk_c d\left(x_a; x, r\right)\right) \operatorname{rect}\left(\frac{x - x_a}{W_x(r)}\right) dx_a \tag{2.26}$$

The focusing of a 2-D SAR image can be decomposed in two elementary phases :

— Range focusing of $s_r(x_a, \tau)$ with (2.12) for each position x_a.

— Phase compensation along the whole azimuth aperture by using $\exp\left(jk_c d(x_a; x, r)\right)$.

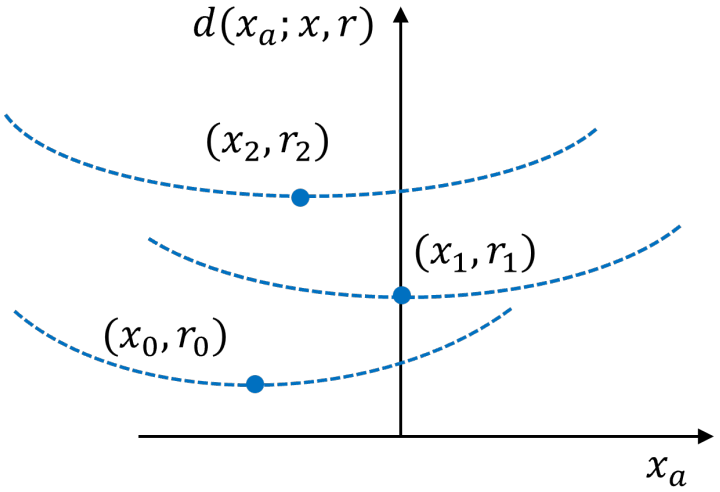

FIGURE 2.11 – Range migration

The signal processed exclusively along the azimuth direction, using the measured signal $s_{rf}(x_a, d(x_a; r, x))$ and the dependency of $d(x_a; r, x)$, at the position of x_a, introduces a phenomenon known as range migration. as shown in Fig. 2.11. This is illustrated in Fig. 2.11 and is caused by the variation in distance between the radar and the target, $d(x_a; r, x) - r$, as x_a changes. Range migration can span the equivalent of several range cell resolutions and exhibits a range curvature contingent on the value of r, thereby necessitating distinct processing strategies for (2.26) across different range coordinates.

Moreover, range focusing is typically accomplished via a FFT, resulting in the definition of the focused signal at evenly spaced range coordinates. For the evaluation of (2.26), a 1-D interpolation of s_{rf} at irregular coordinates and a numerical summation are required. The intricacies of the SAR image focusing algorithm through 2-D adapted filtering are expounded in the overview depicted in Fig. 2.12.

The employed focusing technique, as delineated in (2.26) and illustrated in Fig. 2.12, is back projection [DJ92 ; KS01 ; FP16a]. This technique operates in either the spatial or time domain, and it attains an exceptionally high accuracy. In comparison to other methods in the spectral domain, the back projection emerges as a precise and versatile approach to focusing. It retains the capability to accommodate various acquisition configurations without necessitating modification or approximation. This method's relatively straightforward implementation calls for a standard level of computational power, which is readily available with conventional computing resources.

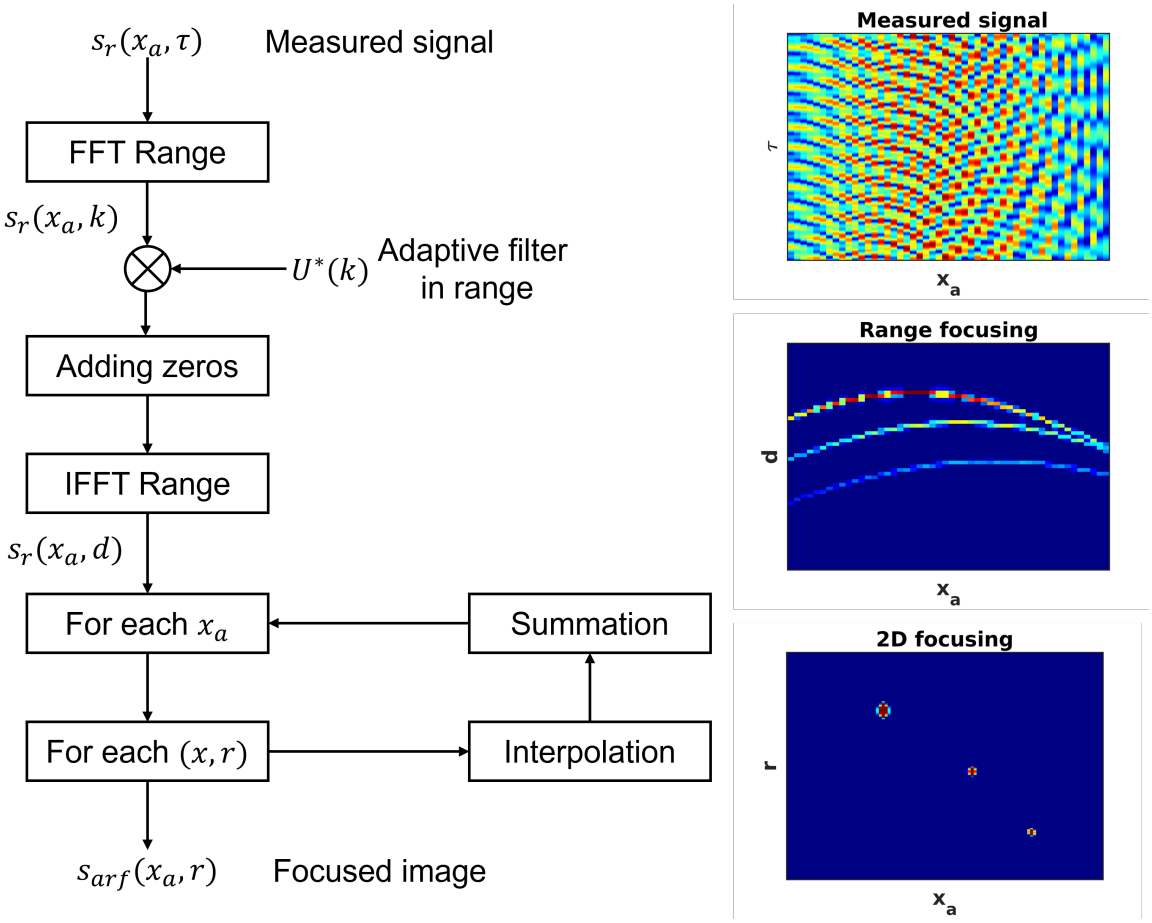

FIGURE 2.12 – SAR focusing using back projection

2.4.3 Properties of focused signal in azimuth

Azimuth resolution

In a SAR measurement, as exemplified in Fig. 2.10, a scatterer undergoes radar measurements along a segment of the flight path, denoted by $L_x = W_x$, which constitutes the synthetic aperture defined by the azimuth aperture of the antenna ϕ_a. Employing (2.23), the expression for the range focused 2-D SAR response of a target with coordinates (x, r), characterized by a constant magnitude and a phase that varies with the radar position in the azimuth direction, over a segment of the track with length L_x, is described by :

$$s_{rf}\left(x_a, d\left(x_a\right)\right) = a_c h(0) \exp\left(-jk_c d\left(x_a\right)\right) \operatorname{rect}\left(\frac{x - x_a}{W_x(r)}\right) \propto \exp\left(j\varphi\left(x_a\right)\right) \operatorname{rect}\left(\frac{x - x_a}{W_x(r)}\right) \tag{2.27}$$

In azimuth, the spectral diversity, arising from the phase variation along the swath, can be quantified using the instantaneous wave number in the $\hat{x}$ direction as :

$$k_x\left(x_a\right) = -k_c \frac{\partial d\left(x_a\right)}{\partial x_a} = k_c \frac{x - x_a}{d\left(x_a\right)} = k_c \sin\phi\left(x_a\right), \text{ with } \left|\phi\left(x_a\right)\right| \leq \frac{\phi_a}{2} \tag{2.28}$$

The signal exhibits an azimuth spectrum characterized by a uniform amplitude over a centered range, with a width of $\Delta k_x = 2k_c \sin\left(\frac{\phi_a}{2}\right)$. The azimuth resolution, denoted as δx, can be calculated by

$$\delta x = \frac{2\pi}{\Delta k_x} = \frac{\lambda_c}{4\sin\left(\frac{\phi_a}{2}\right)} \tag{2.29}$$

By introducing (2.19), the azimuth resolution can be related to the physical length of antenna, approximately represented by

$$\delta x \approx \frac{L_\phi}{2} \tag{2.30}$$

One may note, a smaller antenna size leads to a superior resolution in SAR measurements. However, the necessity for high-gain antennas with large apertures arises due to the requirement for a high SNR. Consequently, a trade-off between resolution and SNR must be taken into account when designing antenna systems.

Azimuth sampling

For a motion with a constant speed v_{SAR}, the spatial sampling is conducted with a periodicity of $\mathrm{d}x = \frac{v_{SAR}}{PRF}$, which must satisfy $\mathrm{d}x \leq \delta x$ in order to avoid spectral ambiguities. The selection of PRF is determined by the duration it takes for the signal to travel from the radar to the target and return, a measure encapsulated by the temporal dispersion of the scene's range response. As a result, the azimuthal sampling frequency is bound by the following limitations

$$\frac{v_{SAR}}{\delta x} \leq PRF \leq \frac{c}{2\Delta d} \quad \text{with} \quad \Delta d \approx \Delta r \approx \frac{W_y}{\sin\theta_c} \tag{2.31}$$

2.5 TomoSAR imaging techniques

Tomographic SAR (TomoSAR) imaging is an advanced 3-D technique that leverages the principles of radar interferometry and tomography to generate detailed three-dimensional reconstructions of landscapes, objects, or structures. Unlike traditional SAR systems that produce 2-D images, TomoSAR extends this capability by incorporating multiple baselines and exploiting the angular diversity. This innovative technology has found applications in a wide range of fields, including environmental monitoring, infrastructure assessment, and disaster management, revolutionizing our ability to analyze and understand dynamic and complex environments [FLS05 ; RM00].

2.5.1 Tomographic SAR geometry

To achieve vertical focusing and generate a three-dimensional SAR image, an additional aperture is synthesized in the vertical direction $\hat{z}$ with a mean value corresponding to the off-nadir angle θ_m and an angular aperture of $\Delta\theta$. The radar is situated at coordinates (x_t, y_t, z_t), while the target is positioned at (x_0, y_0, z_0) in Cartesian coordinates. By utilizing the 2-D SAR response given in (2.23), the expression for the received signal in TomoSAR can be formulated as follows :

$$s_r(z_t, \tau) = a_c \,\mathrm{rect}\left(\frac{z_0 - z_t}{W_z(r_0)}\right) \exp\left(jk_c d(z_t; z_0, r_0)\right) u\left(\tau - \frac{2d(z_t; z_0, r_0)}{c}\right) \tag{2.32}$$

where $d(z_t; z_0, r_0) = \sqrt{(z_t - z_0)^2 + r_0^2}$, with $r_0^2 = x_0^2 + y_0^2$.

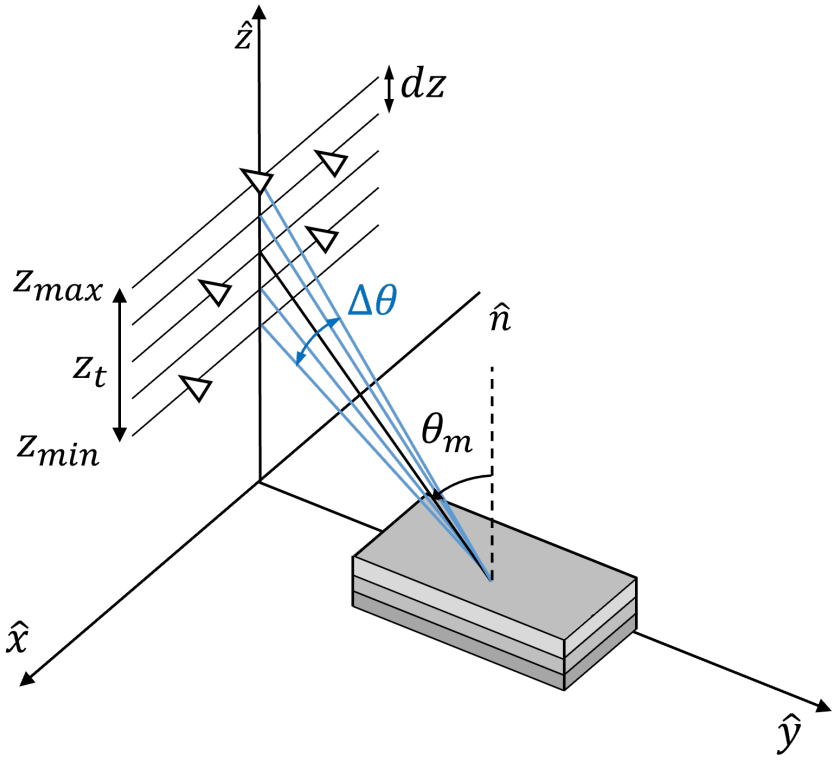

FIGURE 2.13 – Geometry of a TomoSAR acquisition

In elevation, the spectral diversity, arising from the phase variation along the vertical aperture can be quantified using the instantaneous wave number in the $\hat{z}$ direction as :

$$k_z\left(z_t\right) = -k_c \frac{\partial d\left(z_t\right)}{\partial z_t} = k_c \frac{z - z_t}{d\left(z_t\right)} = k_c \sin\theta\left(z_t\right) \tag{2.33}$$

where $z_t \in [z_{\min}, z_{\max}]$ and $\Delta\theta = \theta(z_{\max}) - \theta(z_{\min})$. The vertical resolution, denoted as δz, can be calculated by

$$\delta z = \frac{2\pi}{\Delta k_z} = \frac{2\pi}{k_c(\sin\theta(z_{\max}) - \sin\theta(z_{\min}))} \approx \frac{\lambda_c \sin\theta_m}{4\sin(\Delta\theta/2)} \tag{2.34}$$

Consequently, the vertical ambiguity z_{amb} can be expressed by

$$z_{amb} = \frac{2\pi}{\delta k_z} \approx \frac{2\pi d_0 \sin\theta_m}{k_c \mathrm{d}z} = \frac{\lambda_c d_0 \sin\theta_m}{2\mathrm{d}z} \tag{2.35}$$

where $\mathrm{d}z$ indicates the sampling interval in elevation, and δk_z represents the minimum spacing with two consecutive equivalent vertical wavenumbers, correspondingly.

Assuming that the tracks are uniformly distributed with a baseline distance of $\mathrm{d}z$, the tomographic resolution δz is directly proportional to the number of acquisitions N, following the relation $\delta z \propto \frac{1}{N}$, with $N = \frac{L_{\mathrm{tomo}}}{\mathrm{d}z} + 1$. This establishes a constraint on the geometric tomographic resolution, as a large number of acquisitions demands substantial experimental resources. Moreover, in practical scenarios, tracks are often unevenly distributed, leading to potential height ambiguities. To address these challenges, advanced spectral analysis techniques are employed in SAR tomography, enabling the attainment of high tomographic resolution with a moderate number of acquisitions, even in cases of non-uniform baseline distributions.

2.5.2 3-D tomographic focusing

The 3-D SAR focusing process is demonstrated to be akin to a spectral estimation challenge. This encompasses a range of methodologies, including both nonparametric approaches like beamforming and Capon, as well as parametric techniques such as MUSIC [Hua11]. An essential, universally followed procedure in spectral estimation techniques for tomographic focusing is to first independently apply a 2-D azimuth-range SAR focusing to the signals acquired from parallel tracks. These signals are subsequently synchronized to a unified elevation position. Then, the spectral estimation techniques are employed on

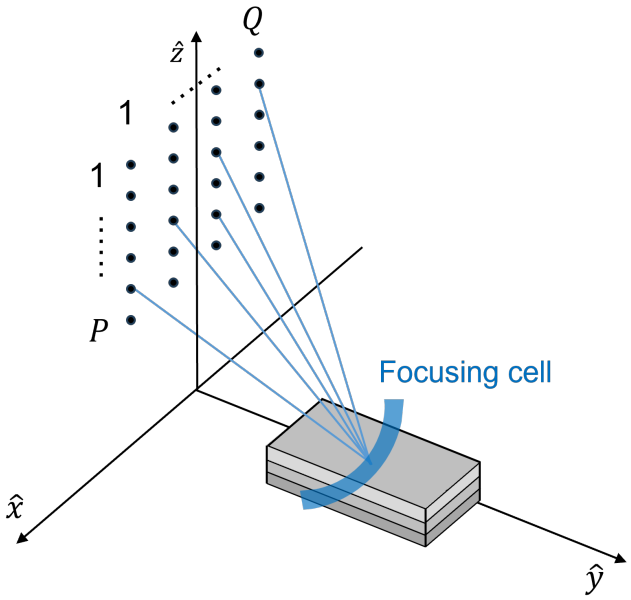

FIGURE 2.14 – Schematic of TomoSAR 3-D focsuing

the set of 2-D azimuth-range focused images. This process enables the reconstruction of scene information in the third dimension. [Yit+16].

The 3-D signal is focused through the joint processing of multiple SAR acquisitions using a time-domain back projection algorithm. The signal received by the considered SFCW radar system can be formally expressed as follows. The 2-D synthetic array, as depicted in Fig. 2.14, is constructed from Q acquisition positions in azimuth and P parallel baselines in the elevation direction. Let the antenna position of each transmitted pulse be represented by $\mathbf{A}_{p,q}$, where $p = 1, \ldots, P$, and $q = 1, \ldots, Q$. Within the SFCW waveform, the selected frequency bandwidth of the system is sampled at frequencies k_n, where $n = 1, \ldots, N$, the wave propagation distance is denoted by $d_{pq}(\mathbf{r}) = \|\mathbf{A}_{p,q} - \mathbf{r}\|$. Consequently, for each antenna position, the received signal, denoted as $s_r\left(d_{pq}(\mathbf{r}), k_n\right)$ in the frequency domain, can be modeled as the summation of the responses attributable to individual scatterers within the 3-D volume as

$$s_r\left(d_{pq}(\mathbf{r}), k_n\right) = \int_V a_c(\mathbf{r}, k_n) \exp\left(-jk_n d_{pq}(\mathbf{r})\right) d\mathbf{r} \tag{2.36}$$

with $V \in \mathbb{R}^3$ denotes the 3-D space in the considered volume, $\mathbf{r}$ signifies the scatterer position in the volume, $a_c(\mathbf{r}, k_n)$ represents frequency- and angle-dependent complex reflectivity of the medium, and $d_{pq}(\mathbf{r})$ is the sensor-scatterer distance.

The 3-D matched filter response of a target at a given focusing position $\mathbf{r}_0\,(x_0, y_0, z_0)$ in a 3-D focusing grid can be expresses as

$$s_{ar}\left(\mathbf{r}_0\right) = \sum_{p=1}^{P}\sum_{q=1}^{Q}\sum_{n=1}^{N} s_r\left(d_{pq}(\mathbf{r}), k_n\right)\exp\left(jk_n(\mathbf{r}_0)\right) \tag{2.37}$$

In the process of back projection focusing, the frequency domain measurements of the target's spectral profile $s_r\left(d_{pq}(\mathbf{r}), k_n\right)$ undergo an inverse Fourier transformation. Subsequently, for every 3-D coordinate within the focusing grid, the contributions from all parallel tracks are aggregated to reconstruct comprehensive 3-D scene information. The resulting 3-D focused signal is expressed as :

$$s_{ar}\left(\mathbf{r}_0\right) = \sum_{p=1}^{P} s_p\left(\mathbf{r}_0\right)\exp\left(j\phi_p\left(\mathbf{r}_0\right)\right) \tag{2.38}$$

where $s_p\left(\mathbf{r}_0\right)$ denotes the focused signal from the p th parallel track at each 3-D position $\mathbf{r}_0$ within the focusing grid. The term $\phi_i\left(\mathbf{r}_0\right)$ represents the phase compensation factor employed in the back projection algorithm.

2.6 Conclusion

In this chapter, a comprehensive foundation in SAR imaging techniques is presented, spanning from the core principles of radar operation to advanced multidimensional imaging methodologies. A detailed explanation of radar mechanisms is explored, covering the propagation of electromagnetic waves and introducing a simplified model for radar signals. The concept of 1-D range focusing is then expounded upon, employing spectral diversity and offering insightful comparisons with commonly used waveforms, i.e. classical pulse, chirp, SFCW and FMCW. Building on this, the chapter extends its focus to 2-D SAR imaging techniques, emphasizing the pivotal role of spatial diversity in achieving high-quality imaging results. The culmination of this chapter lies in the exploration of TomoSAR utilizing multi-baseline data, enabling the estimation of 3-D reflectivity profiles within observed environments. This theoretical foundation lays the groundwork for the understanding and implementation of advanced SAR methodologies in subsequent chapters.

Chapitre 3

Comparison of SAR imaging configurations for roadway characterization

Contents

3.1 Introduction 51
3.2 Comparison of imaging modes 53
3.2.1 Nadir-looking ground penetrating radar 53
3.2.2 Off-nadir synthetic aperture radar 54
3.3 Experiment configuration for roadway characterization . . . 59
3.3.1 Ground-based SAR system operated in BSC and FSC configuration 59
3.3.2 Experiment setup and scene description 61
3.4 Measurement campaign results 64
3.4.1 Comparison of configurations 64
3.4.2 Tomography correction with refraction compensation 71
3.5 Result analysis and advanced feature extraction of roadways 75
3.5.1 Analysis of imaging configurations 75
3.5.2 Permittivity estimation with polarization response 77
3.5.3 Roughness estimation 80
3.6 Conclusion 82

3.1 Introduction

Roadways represent an essential kind of infrastructure for transportation systems, and their safe and efficient operation is critical for society. However, over time, they can

experience degradation due to a variety of factors, including climate, traffic loads, and material quality [Bar+20]. Invisible defects, caused by embedded and structural cracks are serious issues that can lead to costly repairs or even accidents. Therefore, there is a need for effective techniques to evaluate the structural integrity and maintain the durability of roadways.

Microwave remote sensing devices have proven to be valuable tools for detecting and characterizing subsurface features. In particular, Ground Penetrating Radar (GPR) B-scan measurements have been extensively used for roadway inspection [SPF21 ; Jol08 ; Mas96] using incoherent series of high-resolution vertical radar profiles sampled along scanning paths. Efficient techniques, based on such acquisitions, have been developed for characterizing the structure of complex underground media [**rasol2022n** ; SS00 ; Cha+07 ; Ras+20 ; Liu+23]. Advanced signal processing methods may be used to retrieve high-precision vertical information and estimate the structural properties of the observed roadways [Sun+22 ; Sun+18 ; Le +14 ; Pan+21 ; Sun+19 ; Le +19].

Synthetic Aperture Radar (SAR) imaging is a coherent signal processing technique which uses spatial and spectral diversities to synthesize a 2-D map of the reflectivity of a scene [Sou99 ; FP16a]. SAR imaging is generally operated in a side-looking configuration which allows to estimate important geophysical parameters such as roughness or humidity using different modes of diversity [UMF81 ; FP16b]. Classical 2-D SAR mapping is affected by a cylindrical ambiguity and cannot discriminate scatterers located at different elevation positions and whose response fall into the same azimuth-range resolution cell. Tomographic SAR (TomoSAR) imaging represents a solution to this limitation, and may be employed to estimate the 3-D reflectivity of environments [RM00 ; KS01]. This technique relies on the acquisition of multi-baseline interferometric SAR data from slightly shifted trajectories [RM00 ; FHP16a ; FP16b], which are coherently combined in order to generate 3-D images. TomoSAR was used to investigate the characteristics and scattering mechanisms of complex 3-D media such as snow [Rek+17 ; Fre+17], ice [Yit+17 ; Teb+16] and forest [TR12 ; HFR12 ; Agh+20 ; HZF21]. Practical studies used near range TomoSAR imaging to explore detailed structure properties by employing ground-based SAR (GB-SAR) systems [Fre+17 ; Yit+16 ; Yit+17 ; Rek+17 ; Abd+21 ; Har+20].

In a typical back-scattering (BSC) configuration, TomoSAR imaging is usually implemented using several acquisition passes involving co-located transmitters and receivers. The length of the additional aperture determines the vertical resolution of the resulting 3-D image. This study also considers SAR tomography performed in a forward-scattering

(FSC) configuration, i.e. with transmitting and receiving antennas located on opposite sides of the scene. In such a mode, the vertical resolution is fixed by the signal bandwidth, whereas the aperture length set the resolution in the horizontal direction. FSC mechanisms are known to have a much higher energy than their BSC counterparts, due to the fact that waves travel along nearly specular paths. These facts make FSC SAR tomography a very interesting technique for the refined characterization of roadways.

This chapter is based on a recently published paper [Wu+23b], and proposes a comparative analysis of underground characterization techniques with imaging radar techniques. Three radar modes, nadir-looking B-scan, BSC TomoSAR, and FSC TomoSAR are described and their advantages and drawbacks are presented in Section 3.2. Measurements conducted with a GB-SAR operated in all three configurations over a pavement fatigue test circuit are described in Section 3.3. Section 3.4 discusses and compares the performances of the radar modes over pavement defects corresponding with three artificially debonded areas. Further analysis and the estimation of advanced roadway features, such as dielectric permittivity and roughness, are investigated in Section 3.5.

3.2 Comparison of imaging modes

3.2.1 Nadir-looking ground penetrating radar

A classical nadir-looking GPR system uses a pair of transmitting and receiving antennas, to measure waves in the direction perpendicular to the air-ground interface. The vertical resolution δz of such an acquisition depends on the frequency bandwidth B_f, which is given by

$$\delta z = \delta d = \frac{v}{2B_f} \tag{3.1}$$

where v is the propagation velocity of EM waves in the considered medium, and δd represents the range resolution. The azimuth resolution over distributed environments is given by the width of the Fresnel region of the antenna system, as explained in [Jol08]. A nadir-looking GPR radar can be operated to acquire B-scans which contain a series of echos at different positions along the scanning path. The ability of GPR devices to localize heterogeneities and discontinuities makes such systems well-adapted to applications related to road characterization and diagnosis.

Nevertheless, such a system has a very limited resolution in the azimuth direction,

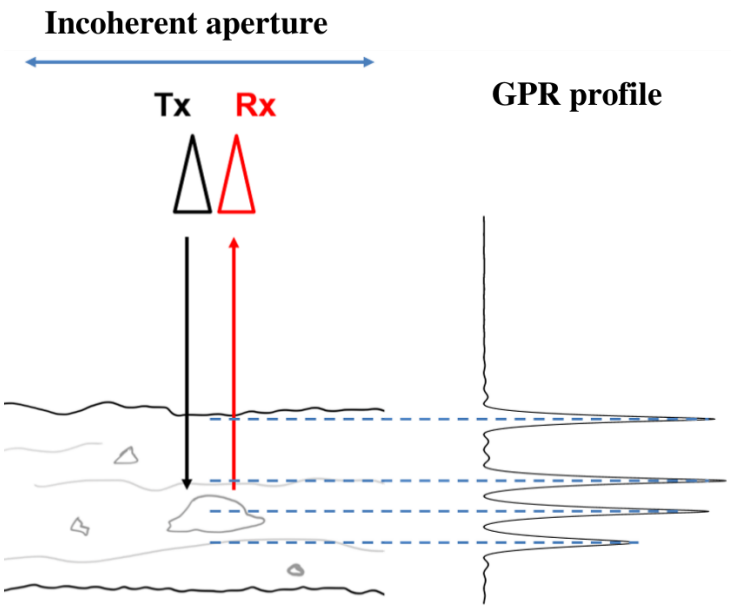

FIGURE 3.1 – Geometry of a nadir-looking GPR acquisition

as B-scans are affected by migration effects, which reduces the possibilities of analysis. GPR systems being operated in the nadir direction generally do not exploit angular and polarization diversities.

3.2.2 Off-nadir synthetic aperture radar

Compared with a nadir-looking GPR achieving 1-D imaging along a track, an off-nadir SAR system utilizes a side-looking configuration to perform 2-D and 3-D focusing using horizontal and vertical spatial diversities, as shown in Fig. 3.2. The back-projection algorithm is used to perform 3-D tomography, in order to discriminate embedded cracks and to characterize dispersive media [DJ92 ; KS01 ; FP16a].

Single-channel monostatic SAR

BSC is the natural observation mode of monostatic SAR, and provides measurements that are sensitive to roughness and polarization diversity. In the case of horizontal layers, the resolutions of a single-channel BSC image are given by

$$\delta z_B|_{y=y_0} = \frac{\delta d}{\cos\theta_1},\ \delta y_B|_{z=z_0} = \frac{\delta d}{\sin\theta_1} \tag{3.2}$$

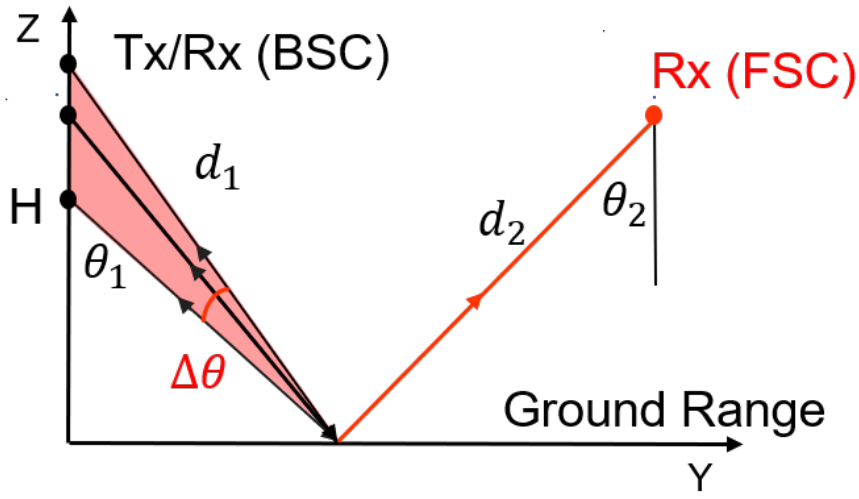

FIGURE 3.2 – Geometry of off-nadir SAR imaging in BSC and FSC modes

where (y_0, z_0) represent the ground range and elevation coordinates corresponding to $\theta = \theta_1$.

BSC imaging suffers from a deterioration of horizontal resolution at near range, i.e. when θ_1 reaches values close to 0 in (3.2), and is subject to a cylindrical ambiguity. Cylindrical ambiguity is illustrated in Fig. 3.3, with scatterers located at Cartesian coordinates y_i and z_i which cannot be separated in a BSC configuration, whatever the signal bandwidth, as they are located on a cylinder, centered at the radar position, whose radius verifies $d_1 = \sqrt{(H - z_i)^2 + y_i^2}, \quad \forall i$. This ambiguity is a strongly limiting factor for the characterization of volumetric media.

Single-channel bistatic SAR

In order to meet the requirements of road inspection, FSC mode of bistatic SAR is proposed to enhance longitudinal detection capability [Dub+06]. Forward-scattered signals traveling along a quasi-optical specular path are much more energetic than back-scattered ones, significantly improving the signal-to-noise ratio (SNR) and detection capability. The range resolution δd is converted into quasi-constant vertical resolution δz_F, whereas the ground range resolution δy_F is very coarse

$$\delta y_F|_{z=z_0} = \frac{2\delta d}{|\sin\theta_1 - \sin\theta_2|}, \quad \delta z_F|_{y=y_0} = \frac{2\delta d}{|\cos\theta_1 + \cos\theta_2|} \approx \sqrt{2}\delta d \ \forall y \tag{3.3}$$

where the expression is given at a certain case with incident and reflecting angles of 45°.

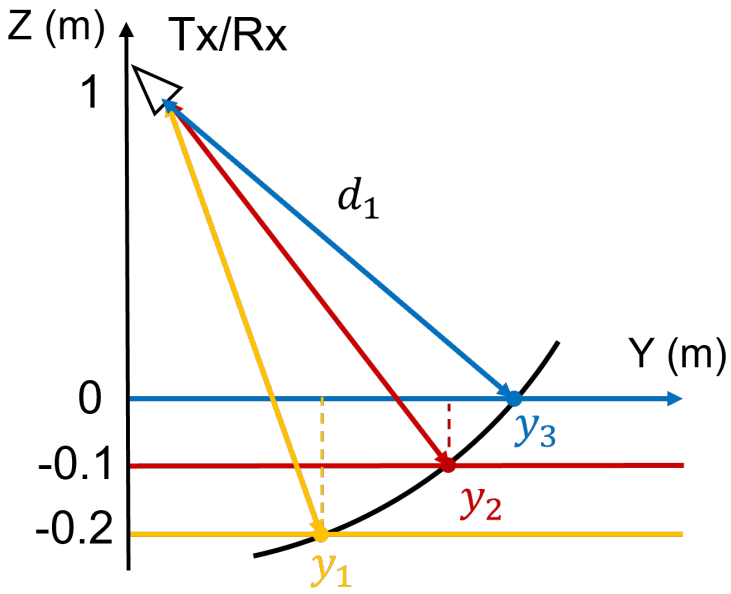

(a) Ground-range elevation plane

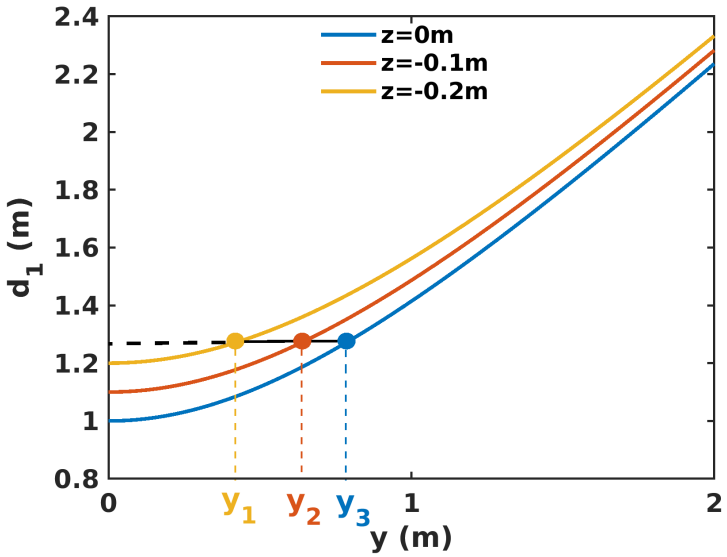

(b) Ground-range distance plane

FIGURE 3.3 – Illustration of cylindrical ambiguity when measuring 3 superimposed layers in BSC mode

Considerable information in the vertical direction can be obtained from a single channel, i.e. with only one pair of antennas. One may note that in such a configuration, the estimated ground-range location is ambiguous, as illustrated in Fig. 3.4. Indeed, considering a scatterer lying on a horizontal layer, there are always to ground-range locations, y_1 and y_2 leading to equal traveled FSC distances, $d(y_1) = d(y_2)$, with

$$d(y) = d_1(y) + d_2(y) \tag{3.4}$$

Tomographic monostatic SAR

A synthetic aperture in the vertical direction can be introduced to implement BSC tomographic imaging, which allows to solve the cylindrical ambiguity.

The tomographic vertical resolution component related to angular diversity only is called $\delta z_{BT\infty}$ as it corresponds to the value obtained under the assumption of an infinite signal bandwidth, or $\delta d \ll \delta\perp$ in Fig. 3.5a. The expression of the vertical resolution is given by

$$\delta z_{BT\infty} = \frac{\lambda_c \sin\theta_1}{4\sin(\Delta\theta/2)} \tag{3.5}$$

where λ_c is the carrier signal wavelength.

Computing effective resolution values, such as those reported in Tab. 3.3, may require to account for the signal bandwidth, as δd and $\delta\perp$ reach comparable levels.

Tomographic bistatic SAR

Tomography is introduced in FSC mode to resolve the ambiguity problem in the range direction of a single-channel acquisition. The displacement of the transmitting antennas in the vertical direction synthesizes an antenna aperture, which focuses an equivalent beam, as indicated with the transparent red zone in Fig. 3.2. The corresponding ground-range resolution, δy_{FT}, is given by

$$\delta y_{FT} = \frac{\lambda_c}{2\cos\theta_1 \sin(\Delta\theta/2)} \tag{3.6}$$

The features of the discussed imaging modes are summarized and compared in Tab. 3.1. GPR operated in the nadir-looking configuration achieves great resolution in the vertical direction but has limited discrimination in the azimuth direction. Tomography brings improved resolutions and solves ambiguity in both BSC and FSC modes, at a cost

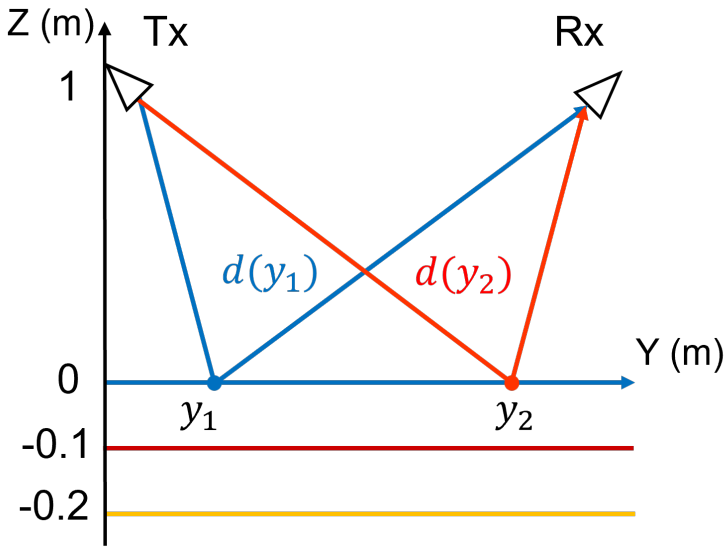

(a) Ground-range elevation plane

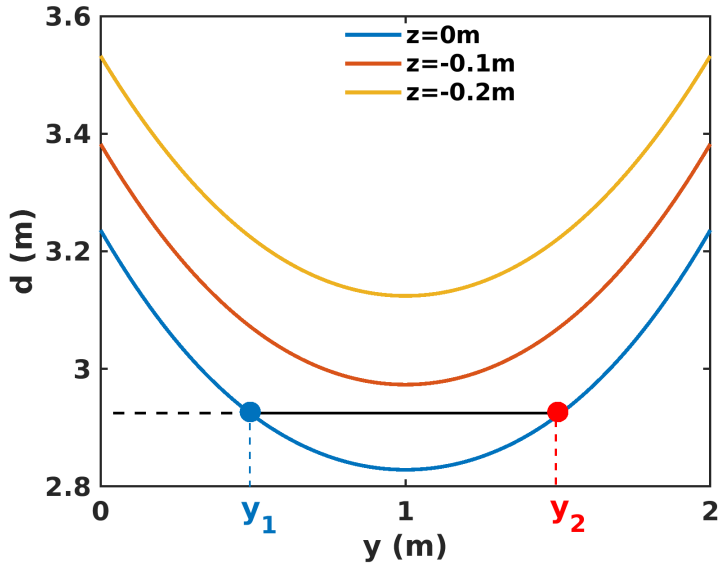

(b) Ground-range distance plane

FIGURE 3.4 – Illustration of ground-range ambiguity when measuring 3 superimposed layers in FSC mode

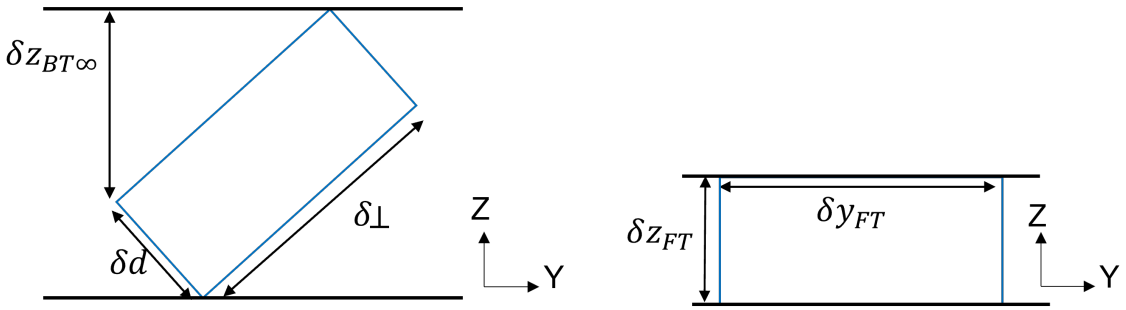

(a) BSC mode **(b)** FSC mode

FIGURE 3.5 – Graphical representation of tomographic resolution cells separating two horizontal layers with $\theta_1 = \theta_2 = 45°$

of increased complexity. By implementing a single channel, FSC can obtain comparable vertical discrimination while keeping a simple structure.

TABLE 3.1 – Comparison of imaging modes

Imaging Modes	Advantage	Drawback
Nadir-looking	Excellent vertical resolution	No focusing on AZ, low polarimetric sensitivity
BSC-tomo	Polarimetry, good resolution, sensitive to roughness	Complex, long time
FSC-tomo	Polarimetry, good resolution both $\hat{y}$ and $\hat{z}$	Complex, long time
FSC single-channel	Polarimetry, good vertical resolution	Poor horizontal discrimination

3.3 Experiment configuration for roadway characterization

3.3.1 Ground-based SAR system operated in BSC and FSC configuration

A GB-SAR system operated in BSC and FSC configurations, and depicted in Fig. 3.6b, has been developed at the IETR laboratory, University of Rennes [WFW21 ; Fer+22], in order to acquire data in both BSC and FSC modes at different frequency bands. The

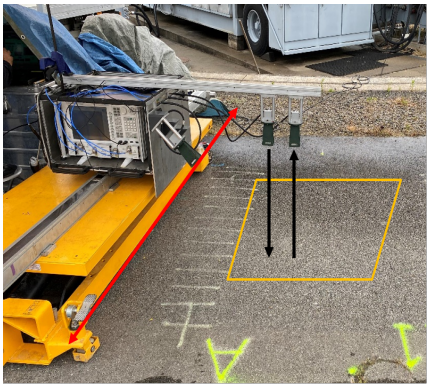

(a) GPR system operated in nadir-looking configuration

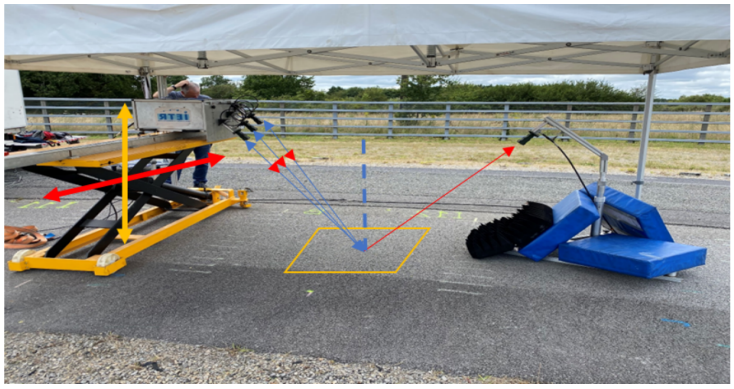

(b) GB-SAR system operated in BSC and FSC configurations

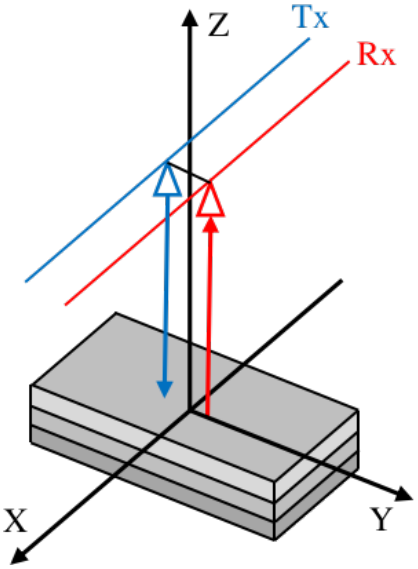

(c) Nadir-looking acquisition geometry

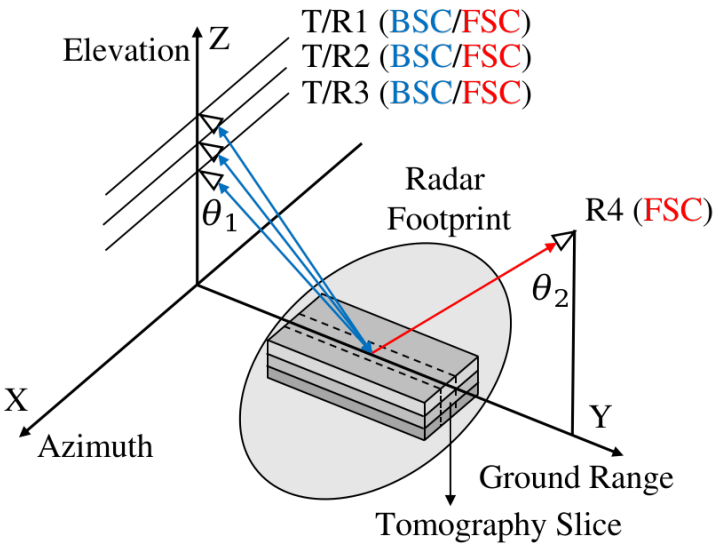

(d) BSC and FSC acquisitions geometries

FIGURE 3.6 – Configurations used during the experiment

SAR device is based on a Vector Network Analyzer (VNA) having four bidirectional ports, connected to horn antennas. The VNA generates Stepped Frequency Continuous Waveforms (SFCW) over a wide spectral domain and measures the response of the scene with high accuracy. Three antennas are fixed on the platform facing the scene to be illuminated, whereas another one is deported on the other side of the scene, in order to acquire signals in FSC mode. The set of three antennas can be moved along a 2-D aperture in azimuth and elevation with a high-accurate servo system and a high-precision lifting platform. In the present study, the system is operated at C and X bands, in both BSC and FSC modes, and at HH and VV polarizations. The experiment parameters are summarized in Tab. 3.2, where N_f is the number of frequency steps, L_x and L_z are the aperture lengths in azimuth and vertical directions, respectively.

TABLE 3.2 – GB-SAR system parameters

	C Band	**X Band**
f_c	5.85 GHz	10 GHz
B_f	2.3 GHz	4 GHz
N_f	1001	2001
L_x	2 m	2 m
L_z	0.8 m	0.72 m
$\mathrm{d}z_B$	0.04 m	0.03 m
$\mathrm{d}z_F$	0.08 m	0.06 m
Polarization	HH/VV	HH/VV

As explained in [Abd+21 ; Har+20], by combing transmitting and receiving channels together with adequate physical antenna spacing and platform motion in the vertical direction, it is possible to generate a quasi-uniform equivalent array of antennas in elevation, with an effective inter-element spacing in elevation denoted by $\mathrm{d}z$ in Tab. 3.2. The values of the equivalent spacings $\mathrm{d}z_B$ and $\mathrm{d}z_F$ differ in BSC modes, as all three antennas on the same side are used as transmitters and receivers.

3.3.2 Experiment setup and scene description

Measurement campaigns were carried out at the roadway test center of UGE, Nantes, France. The fatigue-test facility consists of a ring of full-scale asphalt paved road constructed with four load-bearing robotic arms rolling in a circle, in order to create naturally deteriorated road conditions. One section of a 25 m loop road is built to simulate de-

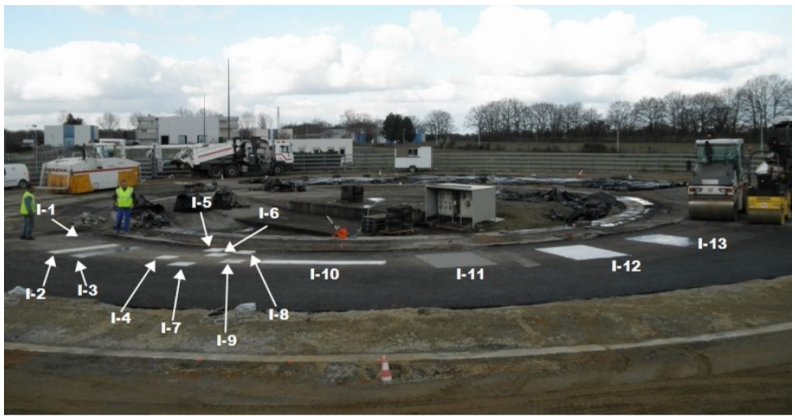

(a) Fatigue-test circuit

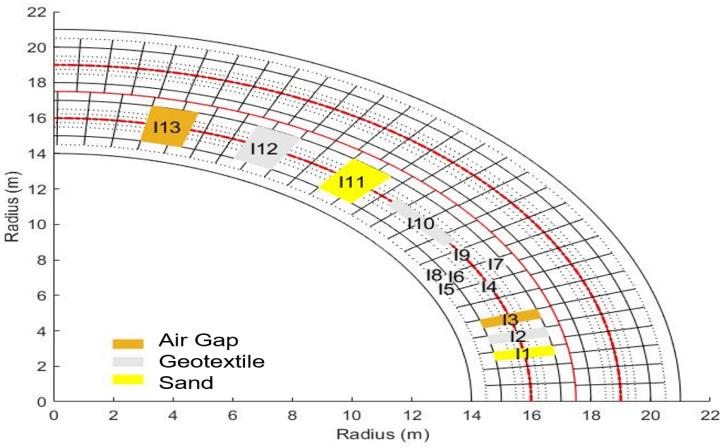

(b) Locations of defects on the circuit ring

FIGURE 3.7 – Overview of the fatigue-test facility [Dér+21]

bonded areas by inserting artificial defects between two asphalt layers. Three types of materials, sand, geotextile, and air gap are used to construct thirteen test zones as shown in Fig. 3.7, zones I11, I12, and I13 are associated with this experiment.

(a) Sand-defect zone **(b)** Geotextile-defect zone **(c)** Air-gap zone

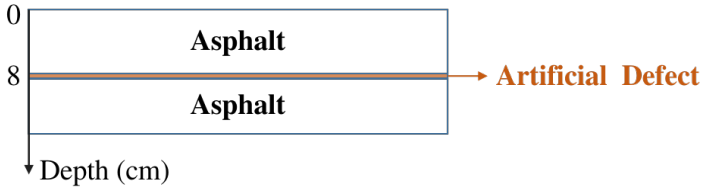

(d) Structure of a debonded zone

FIGURE 3.8 – Description of the debonded roadway zones

As shown in Fig. 3.8a a layer of sand is inserted to simulate a light defect at zone I11 [Sim+14]. A serious defect is created at I12 using a rectangular patch of geotextile in Fig. 3.8b. Figure. 3.8c represents a defect having the shape of a horizontal crack corresponding to an air gap. It is important to know that the defects represent very shallow layers with few millimeter-thickness buried at a depth of approximately 8 cm below the upper ground interface as indicated in Fig. 3.8d.

The experiment is implemented with two groups of the nadir-looking GPR and the GB-SAR operated in FSC and BSC modes as shown in Fig.3.6. The nadir-looking configuration uses a pair of antennas moved in the X direction to get an incoherent B-scan with vertical resolution δz. Off-nadir GB-SAR configurations synthesize a vertical aperture L_z by lifting the antenna array from 0.56 m and 0.64 m to 1.36 m, at C and X band,

respectively.

Spatial resolutions obtained for different configurations are calculated using the experimental setup illustrated in Tab. 3.2, at the scene center, i.e. with $\theta_1 = 45°$. These calculations consider angular apertures of $\Delta\theta = 10°$ and $\Delta\theta = 20°$, at both C and X bands. The detailed results provided in Tab. 3.3 confirm that FSC mode maintains a constant vertical resolution δz_{FT}, independently of the angular aperture, which surpasses the resolution δz_{BT} in BSC mode with a full angular aperture. On the other hand, BSC mode reaches refined ground-range resolution values than the FSC mode. Increasing the angular aperture allows to improve vertical resolution in BSC mode and the horizontal one in the FSC mode.

TABLE 3.3 – Special resolutions for $\theta = 45^o$ and considering propagation in free space (unit : cm)

		$\Delta\theta = 10°$				$\Delta\theta = 20°$			
	δd	δz_{BT}	δy_{BT}	δz_{FT}	δy_{FT}	δz_{BT}	δy_{BT}	δz_{FT}	δy_{FT}
C Band	6.52	15.01	9.22	9.22	41.57	9.82	9.22	9.22	20.85
X Band	3.75	8.73	5.3	5.3	24.32	5.71	5.3	5.3	12.21

3.4 Measurement campaign results

3.4.1 Comparison of configurations

Imaging results are given for all the investigated modes, in Fig. 3.9 in nadir-looking profiling, in Fig. 3.10 for BSC 2-D, in Fig. 3.11 for BSC tomo, in Fig. 3.12 for FSC single-channel, and in Fig. 3.13 for FSC tomo, over three defect zones of geotextile, sand and air gap.

Over the geotextile zone, the nadir-looking incoherent profile measured at C band and depicted in Fig. 3.9a, shows a strong echo for the air-asphalt interface, and a lower intensity one corresponding to the geotextile layer. The peak of the geotextile response is not located at the actual interface depth of 8 *cm* due to the slower propagation of electromagnetic waves in the host medium. By taking the dielectric permittivity of asphalt, $\varepsilon_r \approx 5$ as reported in [Dér+21], into account, the depth axis can be scaled by $\sqrt{\varepsilon_r}$, shifting back the response of the layer to approximately 20 *cm*. Profiles measured at C and X band exhibit a comparable ratio between the reflectivities of the ground surface

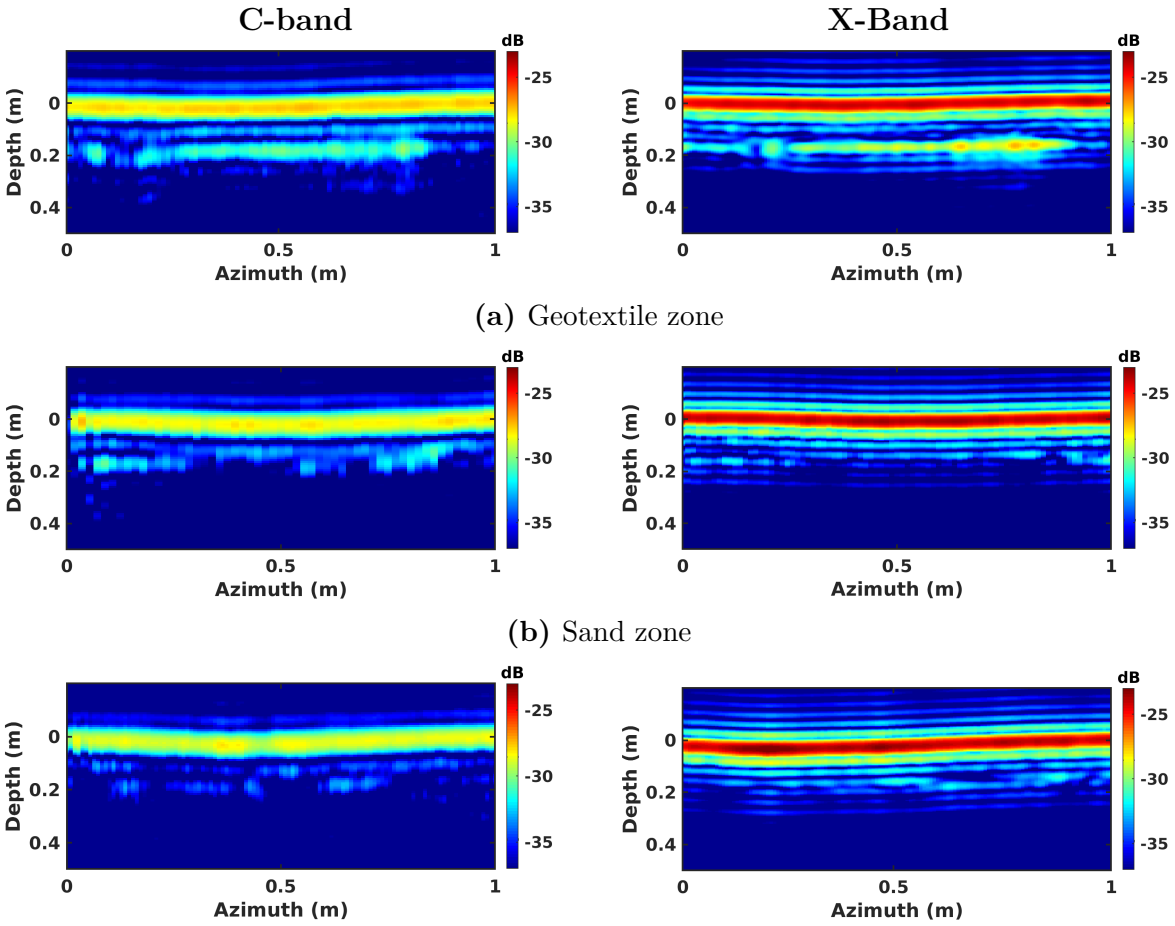

(a) Geotextile zone

(b) Sand zone

(c) Air-gap zone

FIGURE 3.9 – Nadir-looking focusing results obtained over different zones

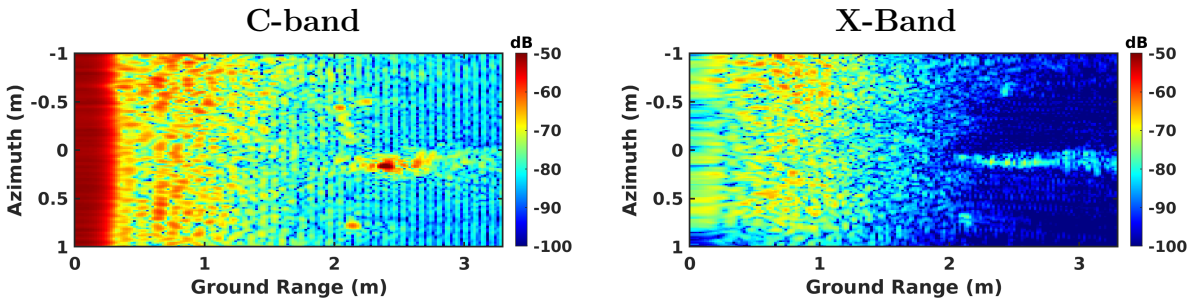

(a) Geotextile zone

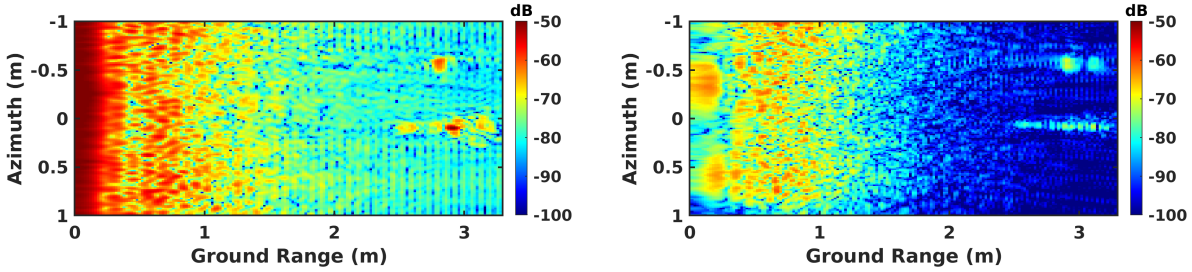

(b) Sand zone

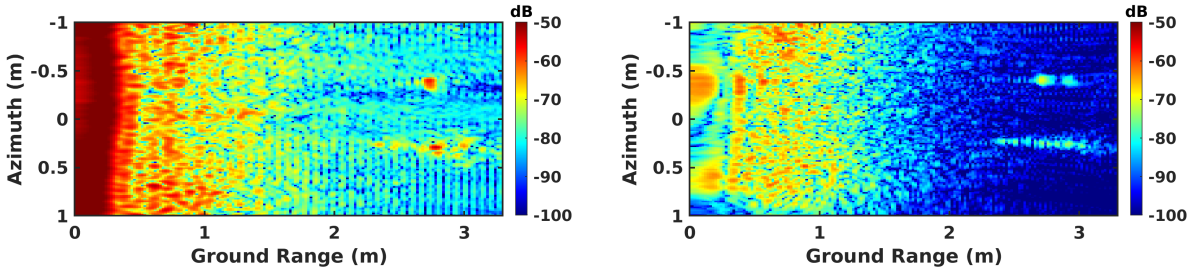

(c) Air-gap zone

FIGURE 3.10 – BSC 2-D focusing results obtained over different zones

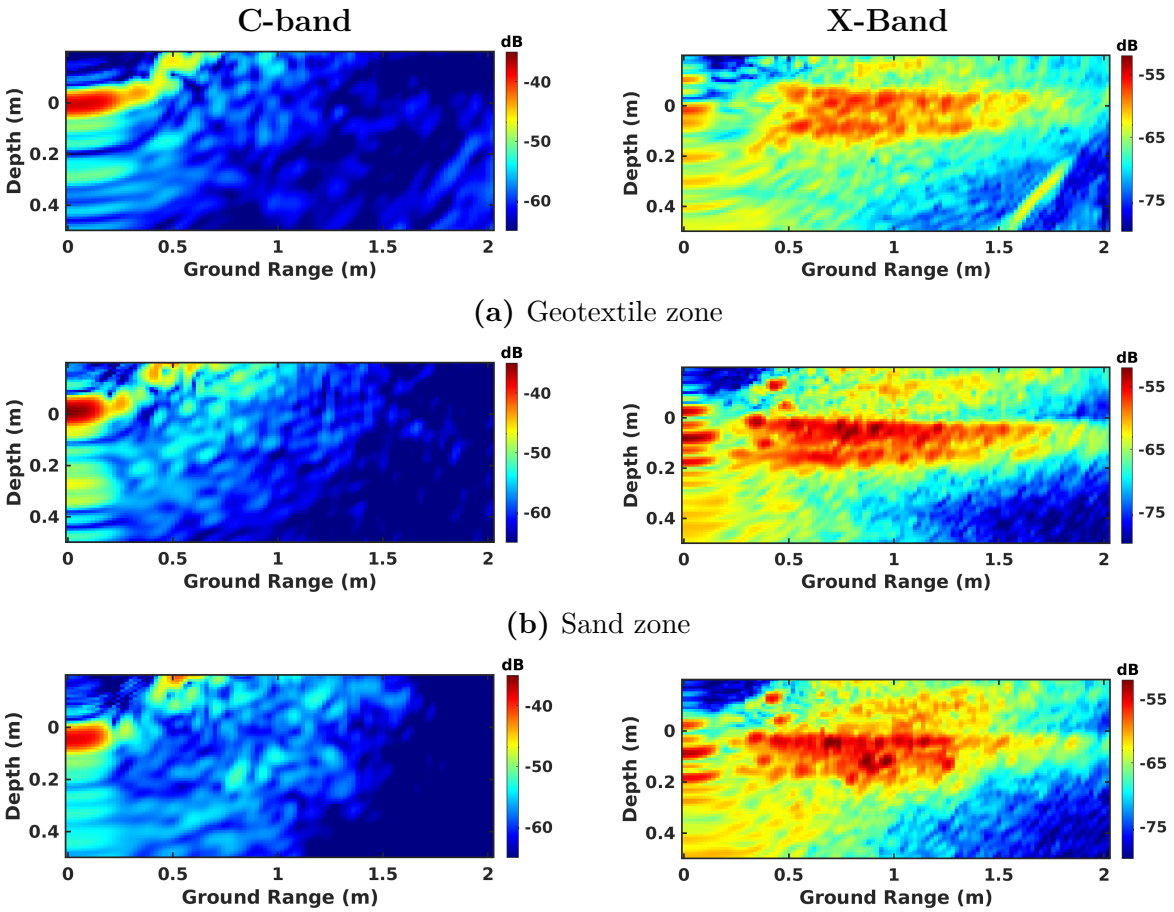

(a) Geotextile zone

(b) Sand zone

(c) Air-gap zone

FIGURE 3.11 – BSC tomographic imaging results over different zones

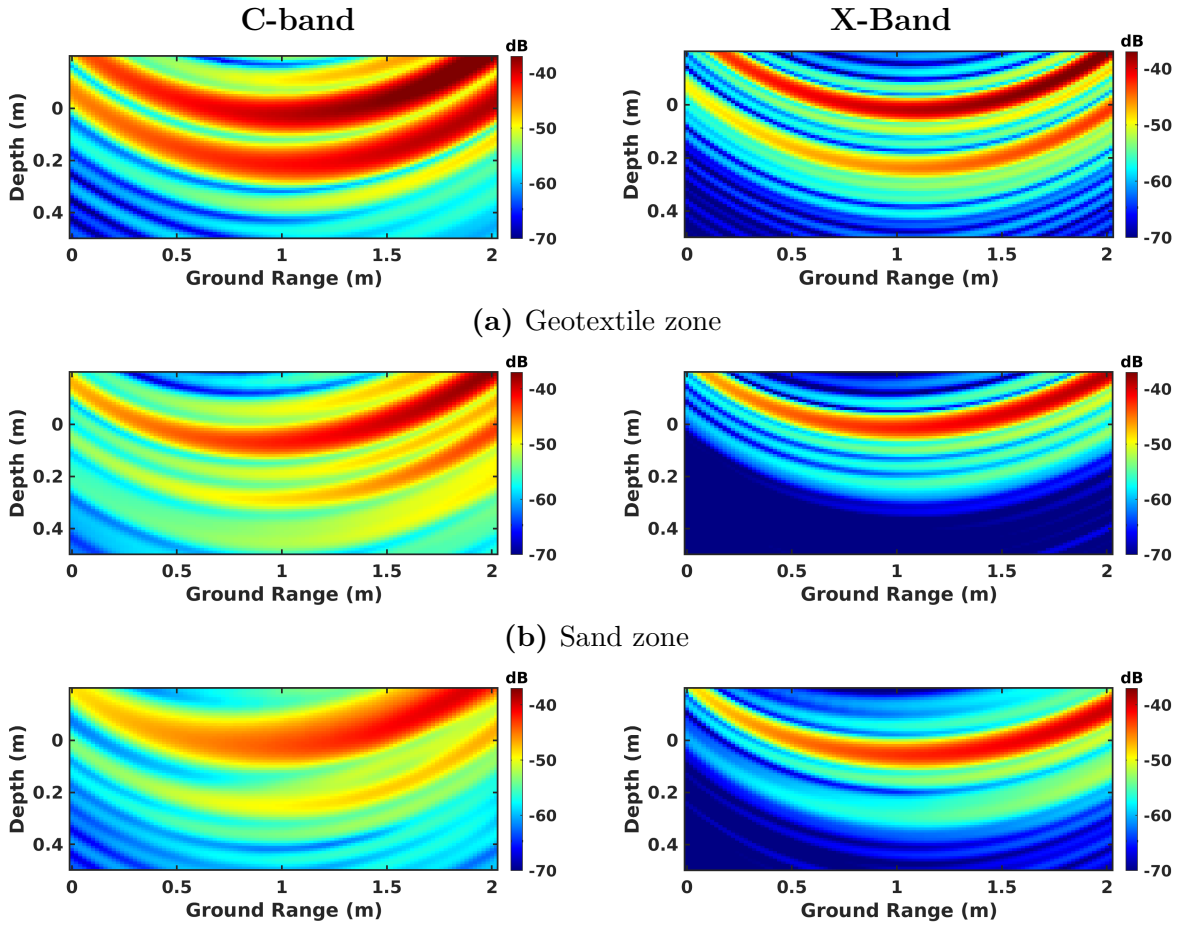

(a) Geotextile zone

(b) Sand zone

(c) Air-gap zone

FIGURE 3.12 – FSC single-channel focusing results over different zones

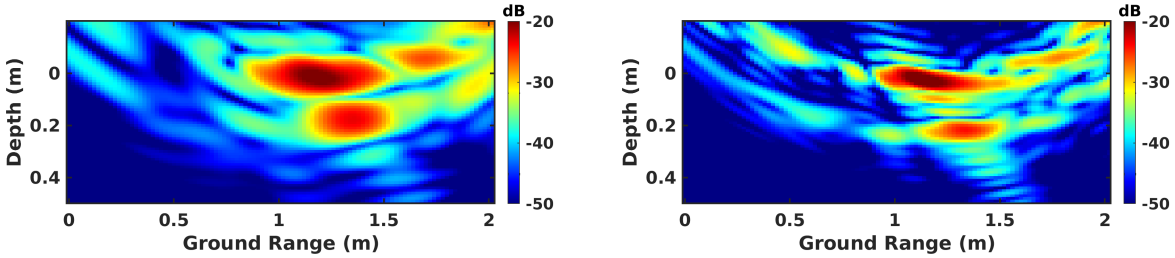

(a) Geotextile zone

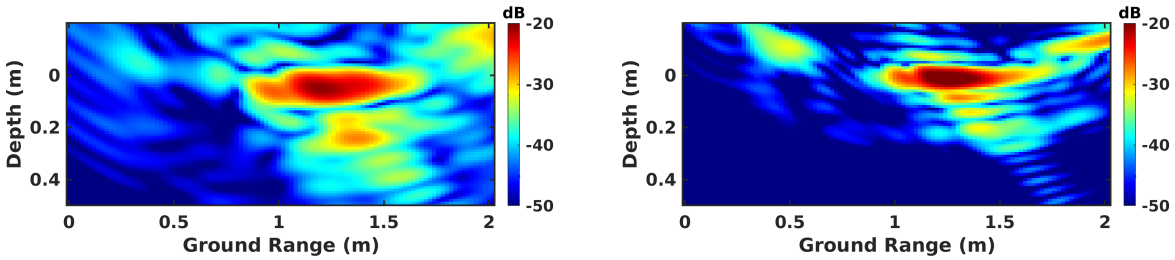

(b) Sand zone

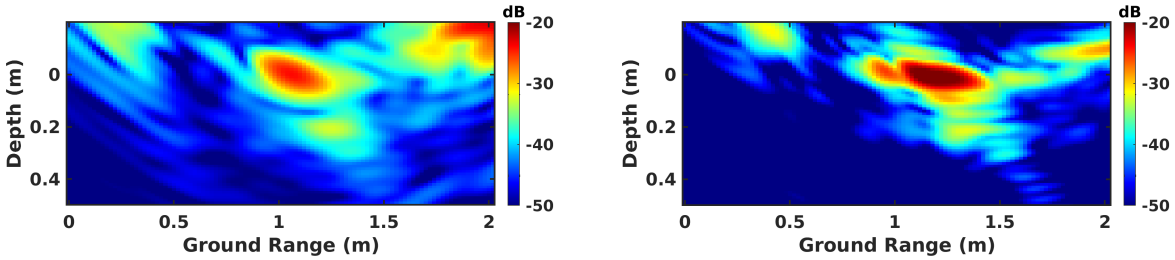

(c) Air-gap zone

FIGURE 3.13 – FSC tomographic imaging results over different zones

and of the defect layer. The dielectric properties, being, in dry conditions, relatively stable over the microwave region [JGB03], the linear increase of wave attenuation with the signal frequency is somehow compensated by the larger reflectivity of the measured interfaces, which appear rougher at shorter wavelengths. One may note that due to the larger bandwidth of the acquired signals, the vertical resolution at X band is much more refined than the one observed at C band. Over sand and air-gap areas, in Fig. 3.9b and 3.9c, the echo from the defect has a very weak amplitude at C band due to a lower reflectivity with respect to the geotextile layer. At X band, the echo is almost invisible, and can not be localized.

The BSC 2-D results, i.e. classical SAR imaging in BSC mode, illustrated in Fig. 3.10a, 3.10b and 3.10c, show that the expected structure of the underlying ground medium can not be appreciated using this kind of measurement, due to the aforementioned cylindrical ambiguity. One may notice the strong decrease of reflectivity in the ground-range direction, due to both the change in incident angle and the antenna pattern of the system. The strong reflectivity area located at the ground range position of 2.5 m corresponds to the response of the acquisition mast depicted in Fig. 3.6b. No reliable information can be extracted from this kind of intensity image for defect discrimination at both C and X bands.

On the other hand, results obtained from BSC tomography, i.e. Fig. 3.11a, 3.11b, and 3.11c, possess interesting features at X band for all the measured media. One can neatly discriminate an upper interface having strong a reflectivity and a lower one corresponding to the defect layer. The response of a underlying defect is focused along a bent shape. This phenomenon is due to the refraction effect as explained in [Har+20 ; Rek+17 ; Yit+16 ; Yit+17]. Interestingly, the application of the same processing steps to C band data leads to a lack of response from volume. This miss focusing is due to the decorrelation between the echos. Indeed, at C band, the roadway appears as a very smooth surface. Most of the emitted energy is reflected away in the forward direction, and the back-scattered signals have a small amplitude, and hence a non-adapted SNR. In such conditions, SAR tomography gives very poor results as the signal cannot be correctly focused.

The single-channel FSC results, shown for the geotextile layer observed in Fig, 3.12a, lead to conclusions that are similar to those raised for the nadir-looking experiments. A strong reflection is observed from the underlying defect at C band, whereas a weaker response is measured at X band. Concerning sand and air gap areas, the detection of the defect layer is extremely difficult in Fig. 3.12b and 3.12c. This result is interesting as it shows that, at lower frequency, it is possible to detect underlying defects by a single pair

of Tx and Rx antennas with 1-D focusing in distance only.

As shown in Fig. 3.13a, tomographic FSC is well adapted to the detection of underlying structures, as it measures strong scattering contributions from both the air-asphalt interface and the subsurface defect, at both frequencies in the case of geotextile. The responses of the defects remain significant at C band for sand and air gap, and are still perceivable at X band as depicted in Fig. 3.13b and 3.13c. One may note the reduced resolution at C band compared with the one at X band, and also the absence of speckle patterns in FSC mode. This is due to the nature of scattering mechanisms in the forward direction, which are composed of coherent terms related to specular reflections.

3.4.2 Tomography correction with refraction compensation

Electromagnetic waves exhibit different propagation characteristics in free space and soil. At the interface of different layers, a refraction phenomenon occurs and the propagation velocities vary according to the permittivity of the media [JZ07; Mir+04]. The positions and shapes of underground targets may be distorted if calculating the distance directly. To focus images accurately, the propagation trace and distance must be corrected and compensated.

In a 3-D Cartesian coordinate system where the antenna's phase center is located at $(0, 0, H)$, the received signals $S_{i,f}$ of the ith point-like scatterer in the frequency domain can be expressed as :

$$S_{i,f} = s_i e^{-j4\pi f d_i/c} \tag{3.7}$$

where s_i represents the complex echo amplitude, f is the working frequency. The equivalent distance from the antenna to the i th point scatter $P_i(x_i, y_i, z_i)$ is denoted by d_i.

Under common free-space conditions, this distance can be directly calculated using Euclidean distance. However, for underground detection, the propagation trace is not straightforward due to the refraction phenomenon. To simplify the model, the geometry configuration is represented using 2-D (ρ, z) coordinates, where $\rho = \sqrt{x^2 + y^2}$ indicates the horizontal distance. The antenna is set at $(0, H)$ and the interface is at $z = 0$ as shown in Fig. 3.14. The equivalent distance d_i is given by :

$$d_i = d_{air} + d_{soil} = \sqrt{\rho_{i0}^2 + H^2} + n_r \sqrt{(\rho_i - \rho_{i0})^2 + z_i^2} \tag{3.8}$$

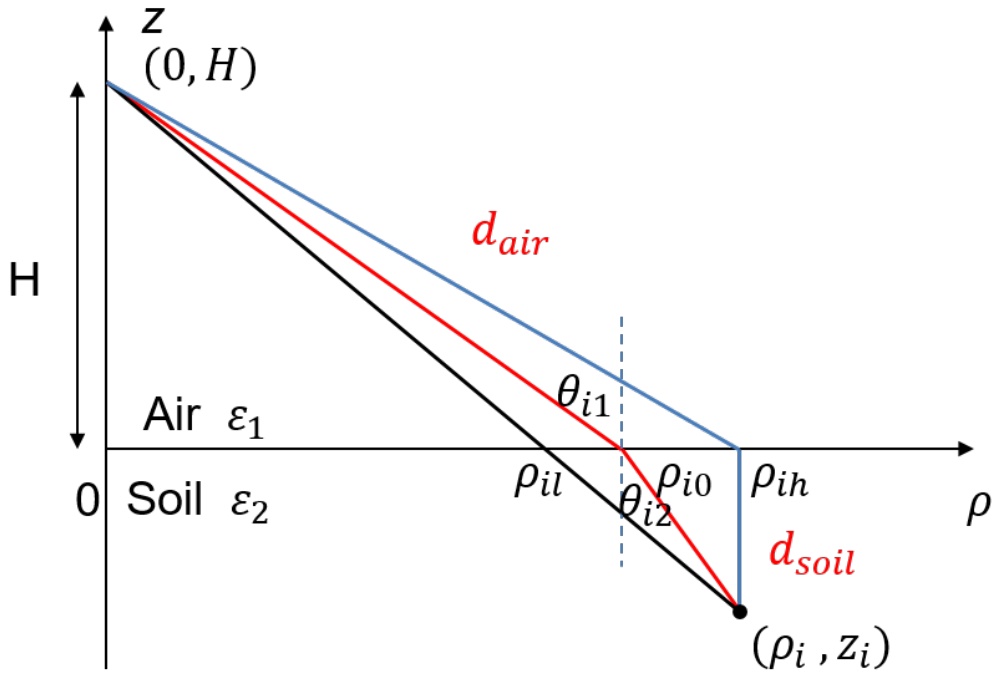

FIGURE 3.14 – Schematic of refraction compensation

where the refraction coefficient $n_r = \sqrt{\varepsilon_2/\varepsilon_1}$ and the horizontal distance of refraction point is ρ_{i0}, which is estimated by a binary searching algorithm in the range of (ρ_{il}, ρ_{ih}).

During the focusing, the distance between the antenna and each pixel in the focusing zone needs to be recalculated as the antenna moves in both azimuth and elevation directions. The amount of computation increases dramatically, due to the refraction compensation incorporated in each calculation. In order to optimize the computational flow, an array of equivalent distance $\mathbf{d}$ is calculated as a function of $(\boldsymbol{\rho}, \mathbf{z})$ for a given antenna height H

$$\mathbf{d} = f(\boldsymbol{\rho}, \mathbf{z}|H) \tag{3.9}$$

where $(\mathbf{d}, \boldsymbol{\rho}, \mathbf{z})$ is the set of (d_i, ρ_i, z_i). The equivalent distance is calculated only once for each antenna pass. For an imaging grid of 13*800*10000 pixels, the improved compensated approach saves 62% time as compared in Tab. 3.4.

The influence of refraction on tomographic and its compensation are illustrated using signals simulated for a specific configuration shown in Fig. 3.15a and system configuration described in Section 3.3.2. The ground layer is located at elevation 0 and the defect layer is buried in the asphalt at the depth of 8 *cm*. The asphalt is considered as a homogeneous

TABLE 3.4 – Comparison of computation time over 13*800*10000 pixels

Focusing Method	Time
Raw focusing without compensation	8 s
Focusing with compensation	82 s
Focusing with optimized compensation	36 s

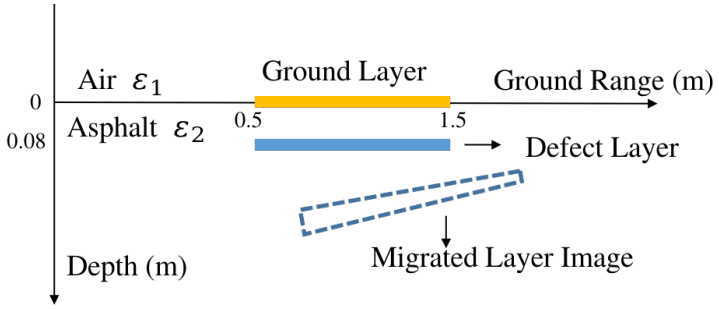

(a) Schematic description of the simulated medium

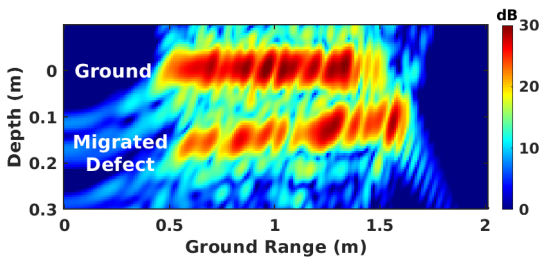

(b) Uncompensated BSC tomo

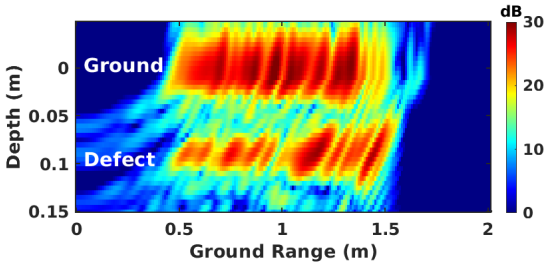

(c) Compensated BSC tomo

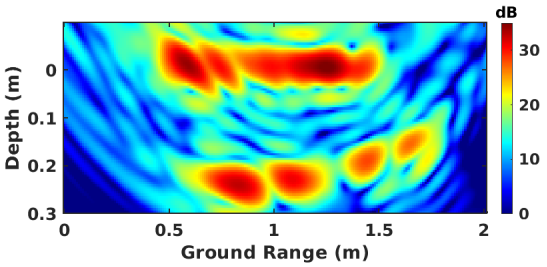

(d) Uncompensated FSC tomo

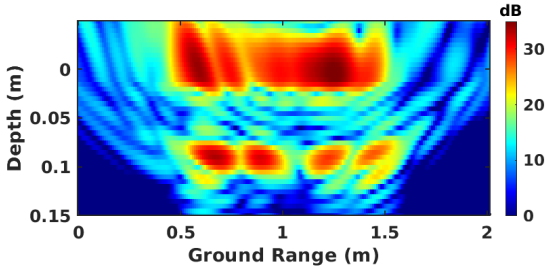

(e) Compensated FSC tomo

FIGURE 3.15 – Illustration of refraction effect and its compensation with the simulated medium

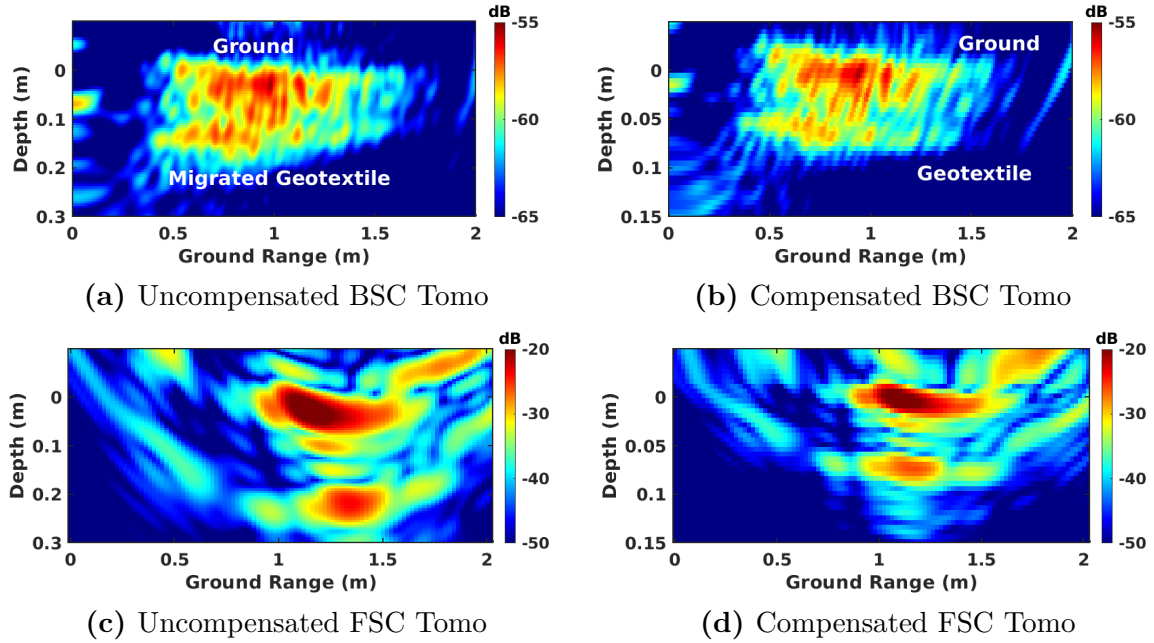

(a) Uncompensated BSC Tomo

(b) Compensated BSC Tomo

(c) Uncompensated FSC Tomo

(d) Compensated FSC Tomo

FIGURE 3.16 – Results comparison before and after compensation over geotextile zone at X band

medium, whose dielectric permittivity is equal to 5, which is equivalent to a refractive index n_r of 2.2.

The uncompensated focusing of the simulated signals in the BSC configuration is shown in Fig. 3.15b. The upper interface is correctly represented as a straight stripe at $z = 0$ over the ground range specified in the simulation configuration. Whereas the defect layer is mislocated at the depth, which is larger than its actual one and varies according to the ground range value. This non-linear delocalization effect has been illustrated and explained in previous works [Har+20 ; Rek+17 ; Yit+16]. In FSC configuration, the delocalization has a larger magnitude due to the specific geometry configuration of bistatic acquisition depicted in Fig. 3.15d. And the originally straight buried layer appears as bent on the resulting tomogram. One can observe on the compensated tomograms of Fig. 3.15c and 3.15e, that the proposed compensation techniques successfully relocate the buried layer at its original location.

The effectiveness of this reconstruction technique is verified over geotextile area in both BSC and FSC modes at X band as shown in Fig. 3.16. The conclusion raised in using simulated signals also applies in this case, that from the corrected tomogram, we can estimate the actual depth of the defect layer, and again in the focusing accuracy. In

FSC mode, the response of the buried layer appears right below the upper layer after compensation in Fig. 3.16d. Whereas in an uncompensated tomogram Fig. 3.16c, it appears slightly shifted to larger ground values. The application of refraction compensation corrects the position and geometrical features of underground layers.

3.5 Result analysis and advanced feature extraction of roadways

3.5.1 Analysis of imaging configurations

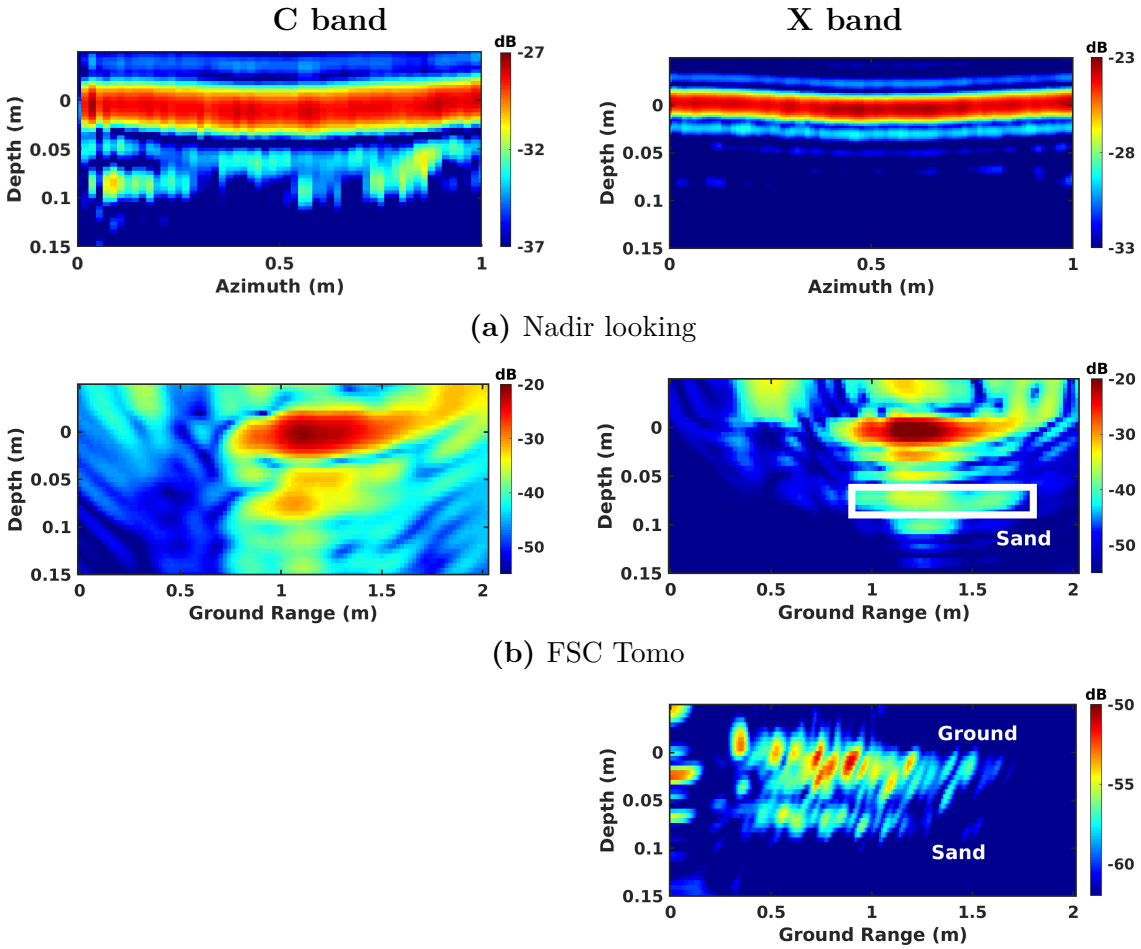

(a) Nadir looking

(b) FSC Tomo

(c) BSC Tomo

FIGURE 3.17 – Compensated imaging results over the sand zone

Over geotextile zones, corresponding to severely debonded roadways, nadir-looking

GPR and FSC allow to discriminate the defect layer at both C and X bands. In BSC tomographic mode, the use of X-band signals permits to reach satisfying performance too. As illustrated in Fig. 3.9a and 3.12a, nadir- and forward-looking configurations can both lead to high-level results, even when using a single channel only.

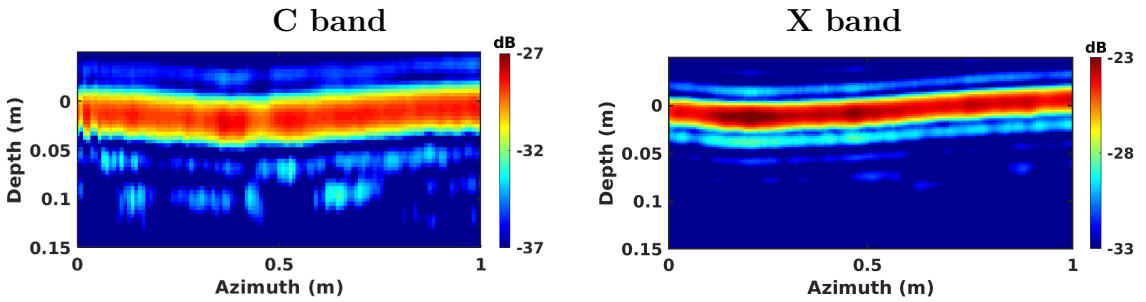

(a) Nadir looking

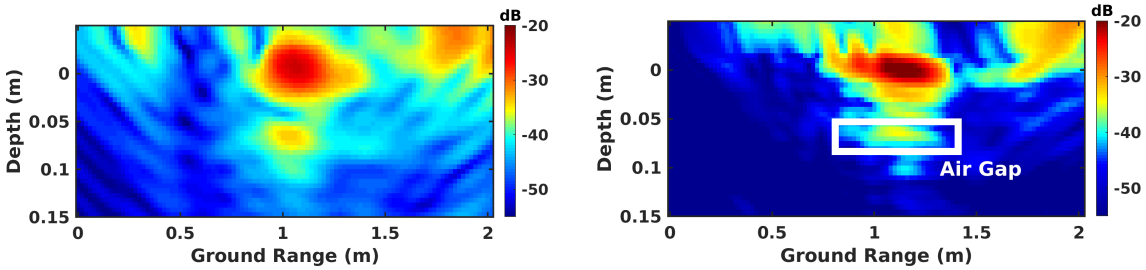

(b) FSC Tomo

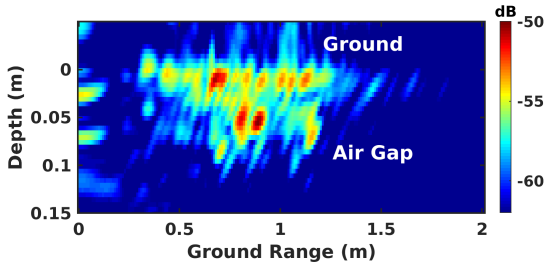

(c) BSC Tomo

FIGURE 3.18 – Compensated imaging results over the air-gap zone

In more complex situations involving sand defects, the nadir-looking mode requires to use lower frequency signals in order to obtain a measurable response from the sand layer, whose response is not observable at X band. At C band, echos are not well-localized and may be confused with the sidelobe of the ground interface, as shown in Fig. 3.17a. In FSC mode, tomographic scattering intensity is high at C band and is still detectable at X band, as depicted in Fig. 3.17b. Interestingly, Figure. 3.17c indicates that the sand layer behaves as a rough surface at X band, and leads to a significant scattering in BSC mode,

although affected by speckle.

Over the air-gap zone, sidelobe and discontinuities in the host medium bring confusion in the analysis of nadir-looking results, even at C band, as indicated in Fig. 3.18a. In comparison, the air gap can be accurately localized in FSC at both C and X bands, as displayed in Fig. 3.18b. Figure. 3.18c also shows a back-scattering source of reflectivity at the location of the air gap, with a lower amplitude compared with the sand defect due to a reduced apparent roughness.

In conclusion, FSC provides satisfactory features over all three debonded areas at C and X bands. Nadir-looking mode operated with a moderate bandwidth works well for geotextile, but in the case of light defects, such as sand and air gap, results indicate a deteriorated detection potential. Interesting roughness-induced features can be measured in BSC mode over all defects at X band.

3.5.2 Permittivity estimation with polarization response

Unlike nadir-looking mode, side-looking configurations such as FSC and BSC may be used to naturally estimate the roughness and moisture of rough surfaces of slightly rough surfaces. Indeed, the radar response of rough surfaces or interfaces, observed at the incident angle, is sensitive to the polarization of the incoming wave. The sensitivity, which is modulated by the dielectric permittivity of the observed medium is enhanced by its moisture content. On the other hand, the analysis of the response of surfaces observed at different incident angles may be used to estimate its roughness property. In the considered cases, the small-perturbation model (SPM), whose application is valid when observing roadway surfaces at C and X bands, may be used to efficiently simulate the reflectivity of such environments [Ric51 ; UMF81 ; TKD04]. This model has the particularity to characterize the roughness-dependent part of the response from the one related to the dielectric properties.

The expression of the scattering coefficient σ_{pq} for the polarimetric channels p and q, which are equal to V or H, is given by

$$\sigma_{pq} = 8 \left| k^2 \sigma_h \cos\theta_1 \cos\theta_2 \alpha_{pq} \right|^2 W(k_x) \tag{3.10}$$

where $W(k_x) = \frac{1}{2} l^2 \exp(-k_x^2 l^2/4)$ is the power spectrum function, k is the wave number, σ_h denotes the surface-height standard deviation and l is the correlation length.

The polarization amplitude α_{pq} can be represented as a function of the relative dielec-

tric constant ε_r, the incident angle θ_1 and scattering one θ_2, and for the relative magnetic permeability $\mu_r = 1$, as

$$\begin{aligned}
\alpha_{HH} &= \frac{-\cos\phi(\varepsilon_r - 1)}{(\cos\theta_2 + \sqrt{\varepsilon_r - \sin^2\theta_2})(\cos\theta_1 + \sqrt{\varepsilon_r - \sin^2\theta_1})} \\
\alpha_{VV} &= \frac{(\varepsilon_r - 1)(\sqrt{(\varepsilon_r - \sin^2\theta_2)(\varepsilon_r - \sin^2\theta_1)}\cos\phi - \varepsilon_r \sin\theta_1 \sin\theta_2)}{(\varepsilon_r \cos\theta_2 + \sqrt{\varepsilon_r - \sin^2\theta_2})(\varepsilon_r \cos\theta_1 + \sqrt{\varepsilon_r - \sin^2\theta_1})}
\end{aligned} \tag{3.11}$$

where $\phi = 0$ in FSC mode, whereas $\phi = \pi$ and $\theta_1 = \theta_2$ in BSC mode. The cross-polarization coefficient $\alpha_{HV} = 0$ at order 1.

TABLE 3.5 – Comparison of polarization ratio and estimated permittivity of experimental scenes

Zone	Geotextile Zone		Sand Zone		Air-Gap Zone	
Marker	L_1	L_2	L_1	L_2	L_1	L_2
FSC Tomo $\frac{\sigma_{HH}}{\sigma_{VV}}$	6.26	0.29	7.55	2.9	8.15	4.63
ε_{r_tomo}	5.8	$\gg 80$	4	9.5	4.1	6.3
FSC Single-Channel $\frac{\sigma_{HH}}{\sigma_{VV}}$	6.16	0.26	8.85	0.07	9.72	3.17
ε_{r_single}	6.1	$\gg 80$	3.7	$\gg 80$	3.7	7.8

From the expression of the reflectivity model by SPM given in (3.10) and (3.11), one realizes that the components related to the dielectric permittivity ε_r of the scattering coefficient can be isolated by computing the ratio $\frac{\sigma_{HH}}{\sigma_{VV}}$, which is equal to the polarization ratio $|\frac{\alpha_{HH}}{\alpha_{VV}}|^2$. For known incident and scattering angles, the estimated dielectric permittivity is the one fits the ratio value. This approach is run on 3-D refraction-compensated tomograms, as shown in Fig. 3.19a, 3.19c and 3.19e, where the black boxes indicate the limits of the areas used to estimate the reflectivity values, with L_1 and L_2 corresponding to the asphalt and defect layer, respectively. The ratio values are calculated based on the angles (θ_1, θ_2) corresponding to the maximum point inside the box.

The estimated permittivity values of asphalt over three zones, as indicated in Table. 3.5, fall within the commonly encountered range for road asphalt [PK15 ; CA21] and are consistent with results reported in [Dér+21] over the same test circuit. The similar ε_r of asphalt over sand and air-gap zones are estimated from measurements acquired during the same sunny day, whereas over the geotextile zone, the measurement took place after a rain event, resulting in a high estimated permittivity value. One may know that the dielectric permittivity of the buried defects can be modulated by humidity related to

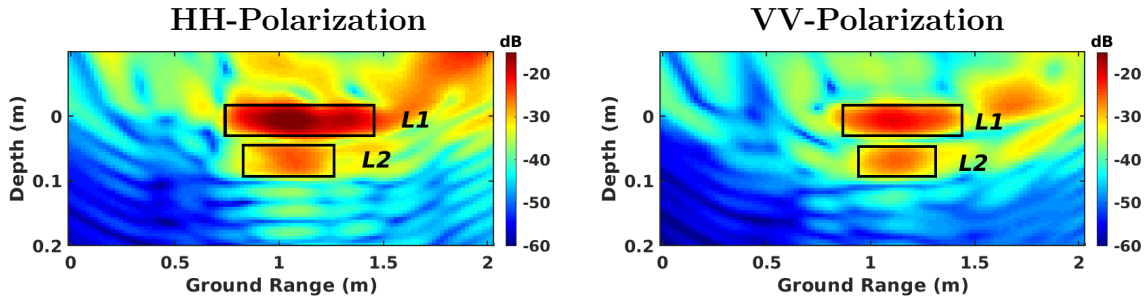

(a) FSC Tomo intensity in geotextile Zone

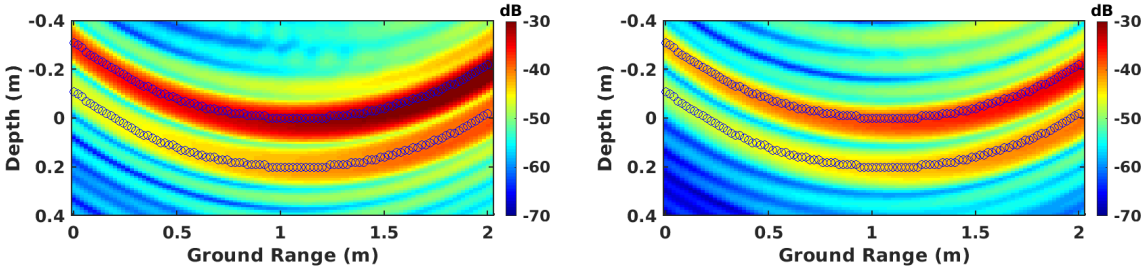

(b) FSC single-channel intensity in geotextile Zone

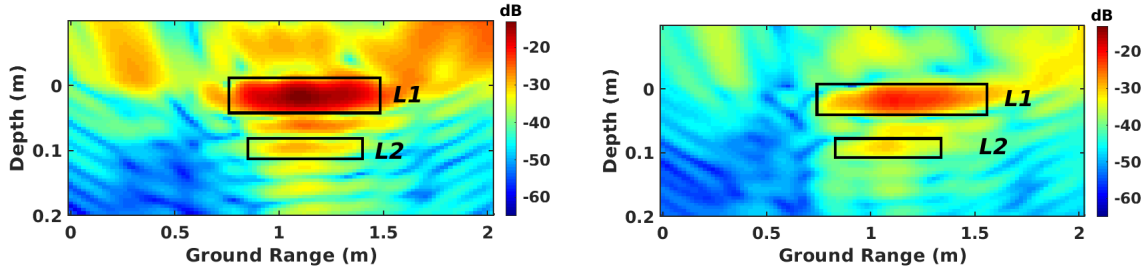

(c) FSC Tomo intensity in sand zone

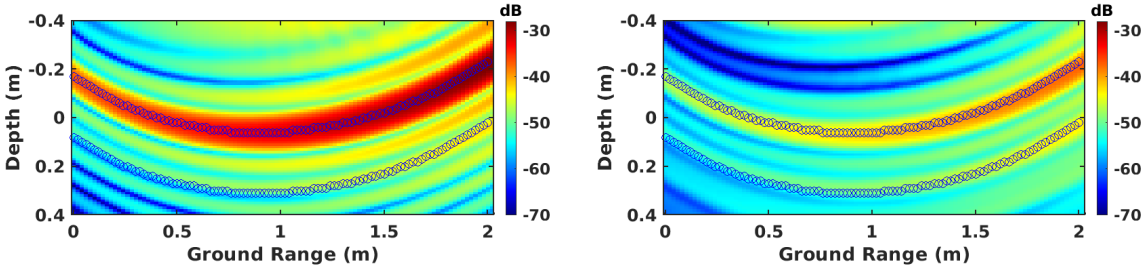

(d) FSC single-channel intensity in sand Zone

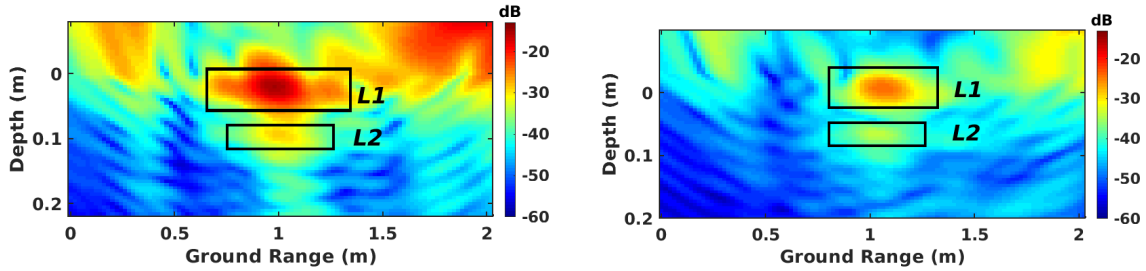

(e) FSC Tomo intensity in air-gap zone

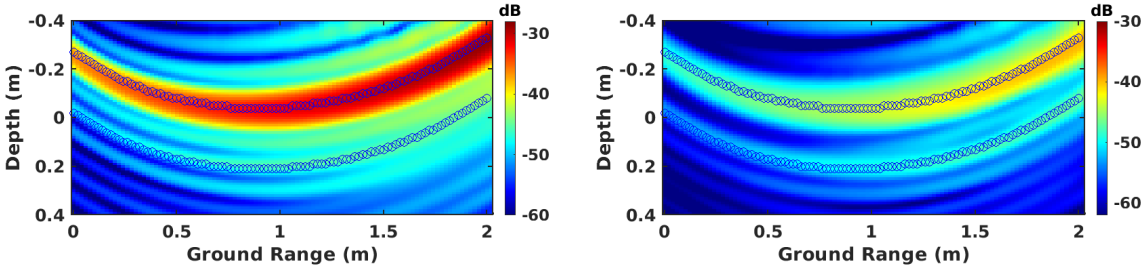

(f) FSC single-channel intensity in air-gap zone

FIGURE 3.19 – Parametric reflectivity of different zones

preceding rain events, with water infiltrated and remained for a long time within the cavity of the defect. This is the certain reason for the extremely high permittivity value of the geotextile, which was soaked with water, with $\varepsilon_r \gg 80$.

Interestingly, this approach could be implemented by a single channel without focusing, as shown in Fig. 3.19b, 3.19d and 3.19f. The reflectivity is calculated with the summation along two curves, corresponding to the responses of the asphalt and defect layers. The dielectric permittivity is estimated under the certain condition, assuming that the targets are located in the middle of the transmitting and receiving antennas in the ground range direction. Similar results are obtained and compared in Table. 3.5, except the ratio value of L_2 in the sand zone, where the reflectivity is small in single-channel mode, and 3-D focusing permits to enhance SNR value by combining channels. Hence, single-channel observations are not sufficient enough for defects with very small responses.

3.5.3 Roughness estimation

The roughness features of both the ground surface and the embedded sand layer are estimated using the aforementioned SPM scattering model and imaging results obtained at X band using the VV-polarization channel. The BSC mode is selected due to its well-known sensitivity to roughness properties when operated at different incident angles. The

express for the scattering coefficient given in (3.10) can be rewritten in BSC mode, with $k_x = 2k \sin\theta_1$ and $\theta_1 = \theta_2$, as

$$\sigma_{vv\_BSC} = 4(k\sigma_h)^2(kl)^2 \cos\theta_1^4 |\alpha_{vv}|^2 \exp(-(kl \sin\theta_1)^2) \tag{3.12}$$

where the roughness parameters are estimated using a fit between the expression of (3.12) and average profiles estimated from the imaging results for different incident angles. As one may note, the surface-height standard deviation $k\sigma_h$ contributes only to the amplitude of σ_{vv_BSC}, and cannot be estimated with our system, as it is not absolutely calibrated. The correlation length kl is hence estimated by normalizing the simulated profiles, that is to the best fit with the measured ones. This procedure is applied to 2-D and 3-D focusing results, after compensating for the attenuation related to the distance between the radar and the considered 3-D location.

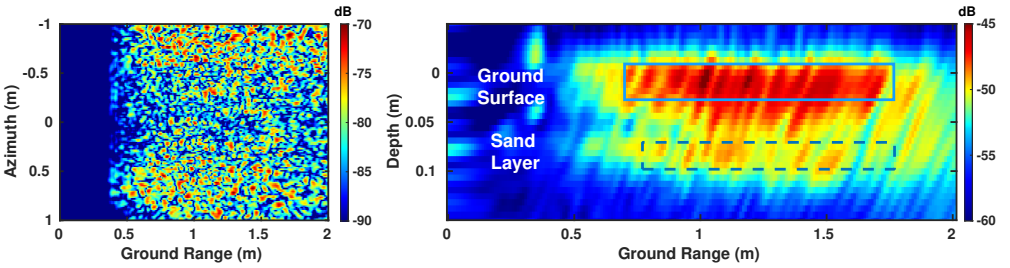

(a) Distance compensated BSC 2-D image

(b) Distance compensated BSC tomogram

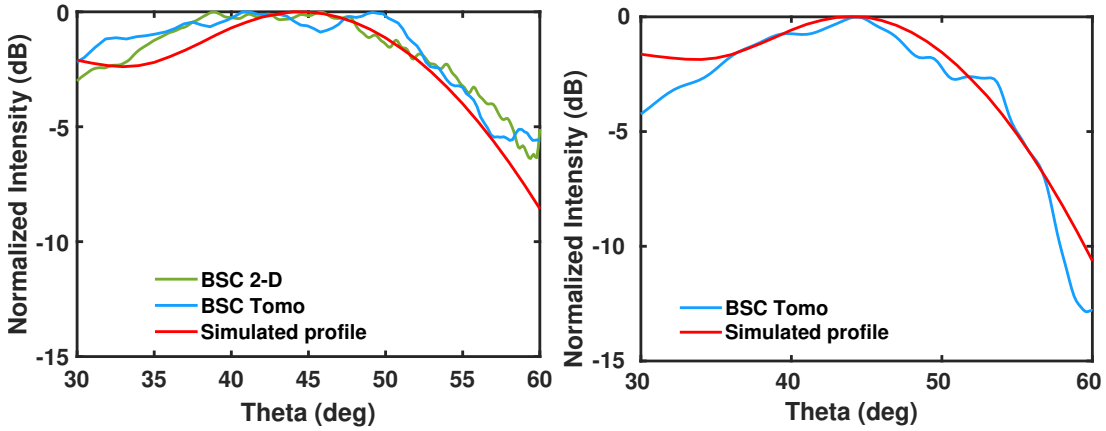

(c) Measured and simulated profiles Ground surface

(d) Measured and simulated profiles Sand Layer

FIGURE 3.20 – Roughness estimation

For the ground surface, one may observe in Fig. 3.20c that, despite the fact that 2-D

focusing results are from the sum of both the ground surface response and that of the underlying sand layer, the scattering features are similar to those obtained in 3-D imaging when selecting only the response of the ground surface. This is due to the fact that the response of the sand layer is significantly smaller than the one of the ground surface. 3-D imaging can then be used to characterize the apparent roughness of the sand layer by applying the SPM model at the corresponding depth with $\theta \in [30°, 60°]$, and the fitting results are shown in Fig. 3.20d. The obtained correlation length values are 3.5 for the ground surface and 4 for the sand layer, indicating slightly rough surfaces.

3.6 Conclusion

This chapter compares three ground penetrating radar modes, nadir-looking B-scan, BSC TomoSAR and FSC TomoSAR, for the characterization and diagnostic of roadways. Measurements conducted with a GB-SAR operated at C and X bands over a pavement fatigue carousel are used to evaluate the ability of the investigated configurations for detecting artificial defects corresponding to very thin layers, or cracks, filled with a geotextile, sand or with air.

Analysis results show that the nadir-looking configuration, when operated with a large but limited bandwidth, i.e. not in ultra large bandwidth conditions, fails to discriminate defects with a very weak signature, such as sand-filled cracks or air gaps at both C and X bands. The BSC TomoSAR mode correctly discriminates the geotextile and the sand defect, but does not sufficiently detect the presence of an air gap, whose interface is too smooth to create a sufficiently large response. FSC TomoSAR successfully isolates all three kinds of defects, due to the large amplitude of the scattered signals in this configuration. Results obtained at X band show an improved resolution that help to discriminate the defects. The gain of performance observed with the SAR-based configuration is probably due to the coherent integration of several range profiles to create an image. The use of polarimetric diversity with the side-looking modes allows to estimate the dielectric permittivity and to correct geometric distortions induced by the refraction of the signal when propagating through the 3-D medium. The angular diversity of the SAR modes is used to estimate some roughness indicators for the imaged interfaces using a scattering model.

The experimental results and theoretical analysis proposed in this chapter show the advantages and inconveniences of the proposed configurations and methodologies, and

their ability to the detect defects hidden inside the roadway pavement.

Chapitre 4

Sliding bistatic TomoSAR imaging

Contents

4.1 Introduction 85
4.2 Investigation of the sliding FSC mode 86
4.2.1 Sliding forward-scattering 87
4.2.2 Resolution comparison of imaging modes 88
4.3 Measurement configuration 90
4.3.1 Sliding Off-Nadir System 90
4.3.2 Bituminous slabs designed for measurements 92
4.4 Measurement campaign results and polarization analysis . . 95
4.4.1 Illustration of COSBis scattering mechanisms 95
4.4.2 Standard monolayer slabs 95
4.4.3 Horizontal crack 98
4.4.4 Vertical crack 100
4.4.5 Analysis of polarimetric responses 104
4.5 Conclusion 108

4.1 Introduction

A side-looking bistatic SAR configuration has been studied in Chapter 3 and published in [WFW21 ; Fer+22 ; Wu+23b], showing good capability for characterizing roadways. Constant vertical resolution, which depends on the signal bandwidth, and a much higher SNR are achieved in FSC tomographic configuration, compared with its BSC counterpart. But, as a trade-off, the horizontal resolution is limited by the vertical aperture of the antenna array. Its application to operational tasks is still limited by the high complexity of the system and the long acquisition duration.

This chapter, based upon the foundation laid in the recently published work [Wu+23a], proposes a new sliding bistaic SAR configuration, keeping the advantages of FSC mode and overcoming the mentioned drawbacks, i.e. high complexity, long acquisition time, and restricted horizontal resolution in the previous chapter. A single pair of opposite-side looking transmitting and receiving antennas are employed, reducing the system complexity to a minimal level, and a horizontal aperture described by a moving platform is synthesized using a focusing algorithm, resulting in an improved ground-range resolution. We analyze the features of the new configuration and perform an experiment over pavement containing cracks to be discriminated, which are simulated with asphalt materials used in French roadways. Results demonstrate the feasibility and the overall good performance of a constant offset sliding bistatic radar configuration with SAR imaging techniques for pavement diagnosis.

4.2 Investigation of the sliding FSC mode

Classical GPR systems operated in a nadir-looking configuration use a pair of transmitting and receiving antennas to characterize the buried structures from B scans. An off-nadir SAR system allows to perform 3-D focusing by using a side-looking configuration, known to be sensitive to interface roughness and polarimetric diversity and discontinuities, to measure BSC and FSC responses, as shown in Fig. 4.1a, where θ_1 and θ_2 are central illumination angles in BSC and FSC modes, respectively. The BSC mode monostatic SAR mode suffers from a loss of horizontal resolution at near range and is subject to cylindrical ambiguity. A solution consists in implementing an additional synthetic aperture in the vertical direction, using an equivalent array, consisting of acquisitions performed at different elevations, resulting in tomographic imaging with improved resolution due to angular diversity [WFW21 ; Fer+22 ; FHP16b]. Bistatic SAR imaging operated in FSC mode is able to obtain a quasi-constant vertical resolution from a single channel with one pair of Tx and Rx antennas at the cost of range ambiguity. By introducing a synthetic aperture in elevation, tomographic FSC brings improved resolutions and solves ambiguity with an increased complexity.

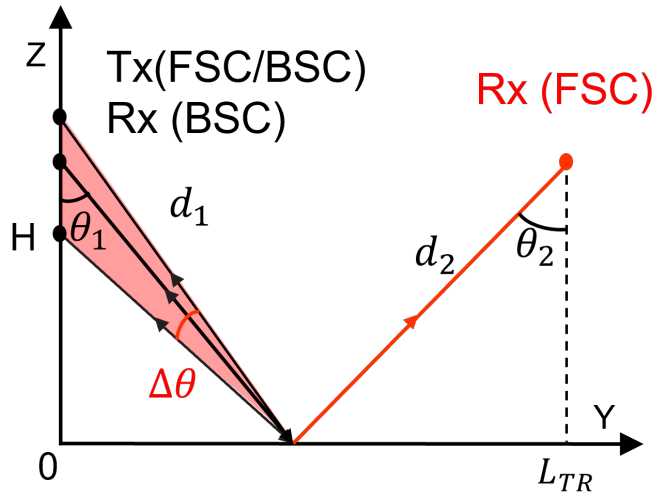

(a) Off-Nadir SAR operated in BSC and FSC modes

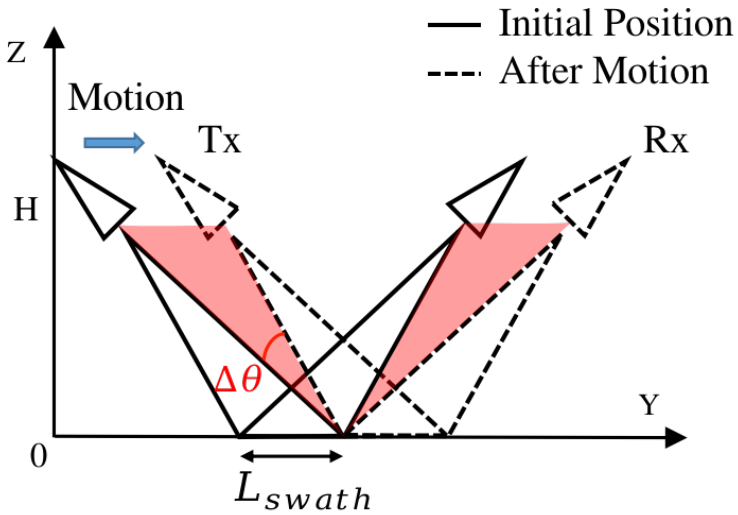

(b) Sliding FSC configuration

FIGURE 4.1 – Geometrical configuration of imaging modes

4.2.1 Sliding forward-scattering

A sliding FSC configuration is proposed in this chapter, as illustrated in Fig. 4.1b, which emulates the angular diversity of tomographic FSC mode with a minimal complexity system, introduces an angular aperture of $\Delta\theta$ by using a single pair of antennas moving

in the ground-range direction. The corresponding resolutions are given by

$$\begin{aligned} \delta z &= \frac{2\delta d}{|\cos\theta_1 + \cos\theta_2|} \approx \sqrt{2}\delta d \\ \delta y &= \frac{\lambda_c}{2(\cos\theta_1 + \cos\theta_2)\sin(\Delta\theta/2)} \approx \frac{\lambda_c}{2\sqrt{2}\sin(\Delta\theta/2)} \end{aligned} \tag{4.1}$$

where $\delta d = \frac{v}{2B_f}$ represents the natural range resolution based on the propagation velocity v and the frequency bandwidth B_f, and λ_c is the carrier signal wavelength.

This simple configuration can be easily mounted on the front of a moving carrier to efficiently generate high-resolution images of volumetric environments. The sampling interval along the motion direction, denoted by dy, is considered to satisfy the following requirement

$$\mathrm{d}y < \frac{\lambda_{min}}{2\sqrt{2}\sin(\Delta\theta_{eff}/2)} \tag{4.2}$$

where λ_{min} represents the minimum wavelength, and θ_{eff} is defined as the effective angular aperture. Considering a system sampling at Pulse Repetition Frequency (PRF) of 1 KHz, the maximum moving velocity, at X band, is estimated to be 200 km/h in ideal conditions, with λ_{min} and $\Delta\theta$ used in the studied experiment, as outlined in Table 4.2. This renders the configuration well-suited for potential implementation on a practical moving platform in the future.

4.2.2 Resolution comparison of imaging modes

The response of a scatterer is simulated with three imaging modes, i.e. nadir-looking GPR, single-channel BSC and single-channel FSC modes, at X-band with a signal bandwidth of 4 GHz. For a scatterer, the classical migration phenomenon is observed with nadir-looking GPR, as shown in Fig. 4.2c. The cylindrical ambiguity is noticed in single-channel BSC mode, and range ambiguity is observed in single-channel FSC mode, as indicated in Fig. 4.2a and Fig. 4.2b, respectively, as compared in [Wu+23b ; WFW21].

The simulation is further performed with the sliding FSC mode, employing the angular apertures of $\Delta\theta$ of 9.93° and 19.58°. In comparison, tomograms are focused in BSC and FSC modes with 6 and 12 images, corresponding to $\Delta\theta$ of 8.98° and 18.02°, respectively, using the configuration described in [WFW21 ; Wu+23b].

The response of the scatterer is focused in BSC mode with 6 images, as depicted in Fig. 4.2d, with sidelobes distributed along the cylindrical ambiguity locus. Figure. 4.2e

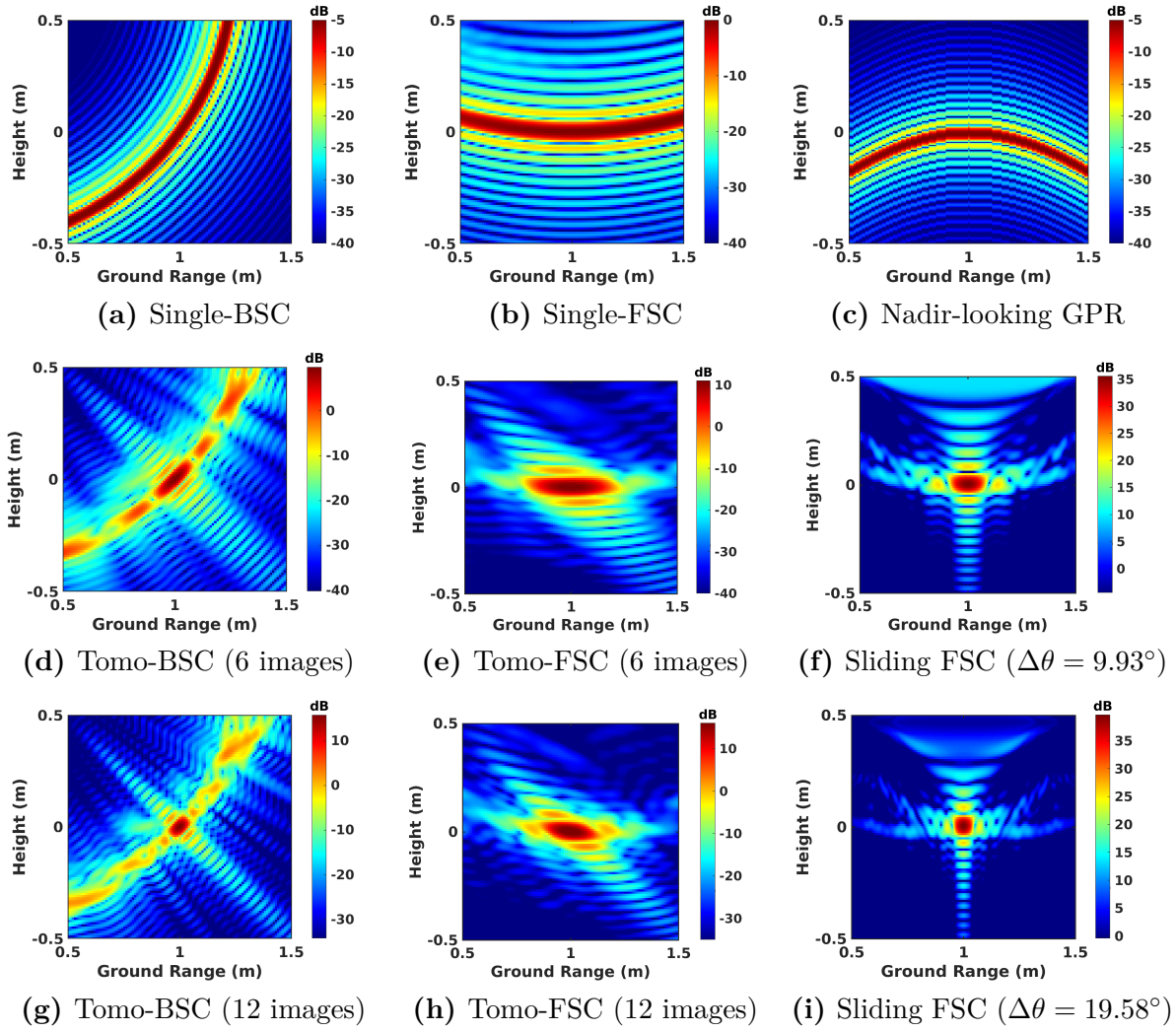

(a) Single-BSC **(b)** Single-FSC **(c)** Nadir-looking GPR

(d) Tomo-BSC (6 images) **(e)** Tomo-FSC (6 images) **(f)** Sliding FSC ($\Delta\theta = 9.93°$)

(g) Tomo-BSC (12 images) **(h)** Tomo-FSC (12 images) **(i)** Sliding FSC ($\Delta\theta = 19.58°$)

FIGURE 4.2 – Resolution comparison simulated over single scatter at (1, 0)

illustrates that the focused target exhibits better vertical resolution in FSC mode than the one in BSC mode, albeit with limited ground-range resolution. In the sliding FSC mode, a regular rectangular pattern is obtained with significantly enhanced horizontal resolution, due to the aperture in the ground-range direction, as displayed in Fig. 4.2f. By the utilization of a double-size aperture, the cross-range resolution is improved, as shown in Fig. 4.2g. A similar conclusion is reached concerning the FSC mode, as depicted in Fig. 4.2h and 4.2i.

Table 4.1 provides a comprehensive summary and comparison of the resolutions obtained in the discussed scenarios. Here, the vertical and horizontal resolutions are represented by δz and δy, respectively, whereas $\delta_p z$ and $\delta_p y$ tend for the projected resolution

in elevation and ground range, respectively. An evident disparity between resolution and its projected counterpart is observable in BSC mode with a limited aperture due to the orientation of the resulting signal spectrum around the mean direction of observation. Conversely, in Tomo-FSC mode, this difference is negligible, as the orientation of the spectrum is less pronounced depending on the focused ground-range position, whereas the spectrum is aligned with the elevation and ground-range axes in the sliding FSC mode. It is noteworthy that the sliding FSC mode leverages a single pair of antennas, achieving consistent and satisfactory vertical resolution akin to that of Tomo-FSC, owing to the inherent advantages of FSC mode. Additionally, it achieves superior horizontal resolution compared with Tomo-BSC when employing a similar aperture.

TABLE 4.1 – Special resolution for single scatter at X band (unit : cm)

Imaging Mode	$\Delta\theta$ (deg)	δz	δy	$\delta_p z$	$\delta_y y$
Nadir-looking	/	3.5	/	/	/
Single-FSC	/	4.75	/	/	/
Tomo-BSC (6 images)	8.98	8.65	8.7	7.85	7.85
Tomo-FSC (6 images)	8.98	4.85	20.05	4.75	19.7
Sliding FSC	9.93	4.9	6.25	4.8	6.05
Tomo-BSC (12 images)	18.02	4.7	4.7	3.96	3.96
Tomo-FSC (12 images)	18.02	4.8	11.85	4.6	11.1
Sliding FSC	19.58	4.85	4.25	4.8	4.45

4.3 Measurement configuration

4.3.1 Sliding Off-Nadir System

A Constant Offset Sliding Bistatic (COSBis) SAR system, depicted in Fig. 4.3a, has been developed at the IETR laboratory, University of Rennes, in order to characterize vertical and horizontal cracks embedded in road pavement. The device is based on a moving platform, driven by a servo moving along a rail in the ground-range direction, with a VNA and a pair of opposite-side-looking antennas. The VNA produces a SFCW signal over an extensive spectral range, precisely records the scene's response, and is connected to horn antennas with bidirectional ports. Three antennas are distributed with equal intervals on one side, working as transmitter and receiver in BSC mode, whereas

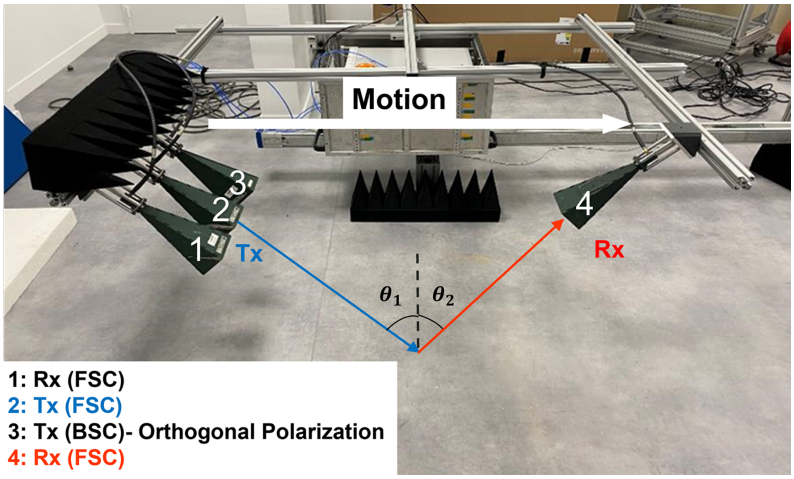

(a) COSBis SAR System operated in the sliding FSC mode

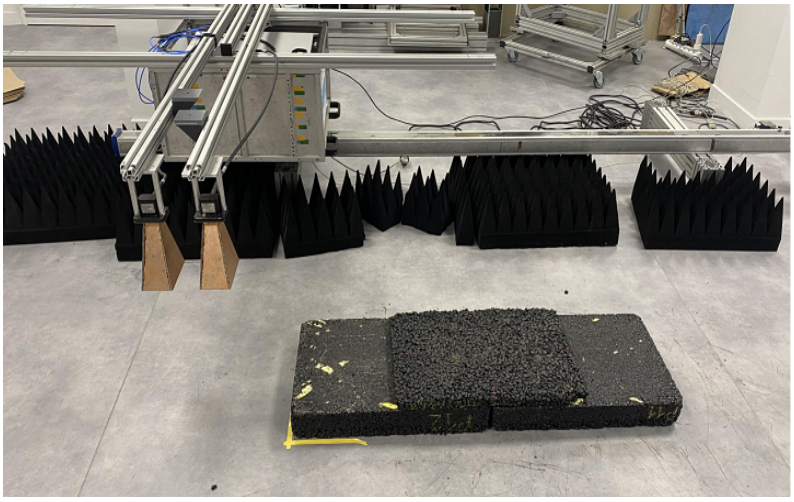

(b) GPR system operated in nadir-looking mode

FIGURE 4.3 – Configurations used during the experiment

another one is placed on the opposite side, in order to receive signals in FSC mode. In the present study, COSBis is operated at C band (4.9 GHz - 7 GHz) and X band (8.4 GHz - 12.4 GHz), measuring both BSC and FSC responses at HH and VV polarizations. The experiment parameters are summarized in Table 4.2, where N_f is the number of frequency points, and L_{TR} represents the distance separating FSC Tx and Rx antennas. The GPR mode is shown in Fig. 4.3b, and uses a pair of nadir-looking antennas pointing toward the ground.

TABLE 4.2 – COSBis system parameters

	Unit	C-Band	X-Band
f_c	GHz	5.95	10
B_f	GHz	2.1	4
N_f		101	201
H	m	0.45	0.435
L_{TR}	m	1.03	0.99
θ_1	deg	45	45
θ_2	deg	45	45
dy	cm	1.5	1
θ_{ap}	deg	20	20
$\Delta\theta$	deg	14.28	14.71

4.3.2 Bituminous slabs designed for measurements

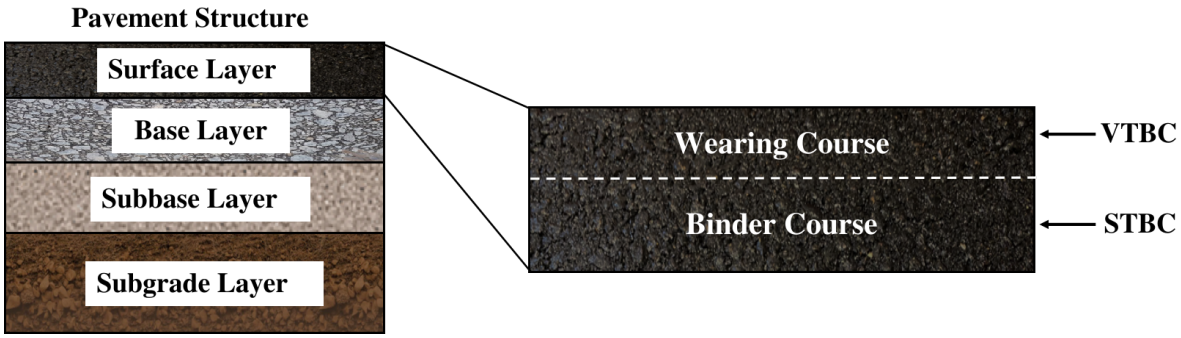

FIGURE 4.4 – Structure of the surface layer in a flexible pavement

A road pavement is a multi-layer structure, as shown in Fig. 4.4, where the surface layer is of most concern for inspection and maintenance [SET94]. Bituminous samples used for measurements are constructed with a plate compactor device adhering to French standards EN 12697-33 [Sta19], at CEREMA, Angers, as shown in Fig. 4.5a. Two kinds of samples, Very Thin Bituminous Concrete (VTBC) and Semi-Thin Bituminous Concrete (STBC), are fabricated for the test and widely used as the surface layer of French pavements [SET94].

— VTBC, known as Béton Bitumineux Très Mince (BBTM) in French, refers to a type of very thin asphalt concrete and is usually exploited for the wearing course. As shown in Fig. 4.5b, the monolayer slab of VTBC, is fabricated with a grain size

(a) Devices for compacting asphalt plates

(b) Wearing course - VTBC

(c) Binder course - STBC

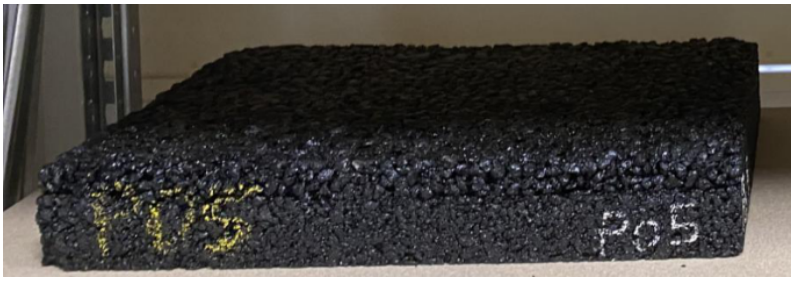

(d) Surface layer - Bilayer HMA
VTBC compacted on STBC with a tack coat

FIGURE 4.5 – Description of asphalt samples used in experiments

of 0/10 mm with discontinuities of 2/6 mm, designed to provide a durable surface while minimizing the thickness of the pavement structure.

(a) Horizontal detachment inside a surface layer simulated with VTBC placed on STBC without a tack coat

(b) Vertical crack within a surface layer simulated as horizontal discontinuity between two bilayer HMAs

FIGURE 4.6 – Illustration of the artificial cracks used in experiments

— STBC, also named Bétons Bitumineux Semi Grenus (BBSG), is a type of asphalt concrete mixture that contains a coarser aggregate compared to the standard dense-graded asphalt mixes. The STBC slab, as illustrated in Fig. 4.5c, is constructed with a grain size of 0/10, smooth and compacted, exploited as the binder course. This material is often used in areas with high traffic loads or in specific pavement layers to meet specific engineering requirements.

Both VTBC and STBC are fabricated with aggregates mixture of rhyolite ($\varepsilon_r = 4.8 - 5.7$) and gneiss ($\varepsilon_r = 4.9 - 5.5$) [Zhe+20 ; Ara+16]. The bilayer slabs of Hot-Mix Asphalt (HMA), as depicted in Fig. 4.5d, representing the pavement surface layer, are compacted by superimposing VTBC on STBC with a tack coat. The dimensions of the slabs are summarized in Table 4.3.

TABLE 4.3 – Dimensions of bituminous slabs (unit : cm)

	Length	Width	Height
VTBC	60	40	2.5
STBC	60	40	6
HMA	60	40	8.5

Standard tests are performed by scanning along the longitudinal direction of monolayer slabs, i.e. VTBC and STBC, on the ground. Horizontal cracks in HMA, consisting as the

detachment of the wearing and binder courses, are simulated by placing VTBC on STBC without a tack coat, as shown in Fig. 4.6a. Another condition is addressed with vertical cracks in the surface layer, as illustrated in Fig. 4.6b, which is implemented by placing two bilayer slabs with a horizontal gap in the longitudinal direction.

4.4 Measurement campaign results and polarization analysis

4.4.1 Illustration of COSBis scattering mechanisms

A preparatory experiment is implemented to illustrate the scattering mechanisms of FSC and BSC modes, by placing metal handles on the ground, as shown in Fig. 4.7a.

The ground floor is clearly discriminated in FSC mode at both X and C bands, as illustrated in Fig. 4.7b and 4.8a, owing to the pronounced specular reflection arising from its smooth surface. Conversely, the reflectivity of the ground surface remains low in BSC mode, as depicted in Fig. 4.7c and 4.8a, due to the diminished backward reflection. In contrast, multiple scattering over metal handles, particularly double-bounce scattering, leads to a strong response in BSC mode, whereas a low intensity may be observed in FSC mode [UMF81 ; Abd+21].

One may note, that the test is conducted over a 5 cm-thick ground floor, composed of two thin layers with an intermediate filling. At X band, the echoes originating from the top and bottom layers are distinctly discernible in FSC mode, as indicated in Fig. 4.7b, whereas the separation of two layers can not be distinguished at C band, due to the limited vertical resolution induced by the smaller signal bandwidth

4.4.2 Standard monolayer slabs

Standard measurements are implemented over two monolayer slabs, VTBC and STBC, as shown in Fig. 4.9a and 4.10a, in order to create reference results for subsequent tests with complex pavement conditions.

One may observe in Fig. 4.9c, that the echo from the ground appears at a slightly lower elevation beneath the slab. This is due to the additional delay introduced by the propagation of the EM waves through the asphalt, whose dielectric permittivity is $\varepsilon_r \approx 5$ [Ado06]. The delayed ground echo in nadir looking, as depicted in Fig. 4.9b, exhibits a

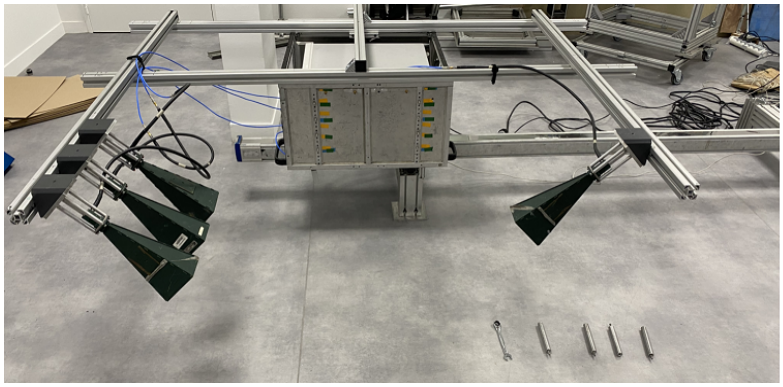

(a) Metal handles

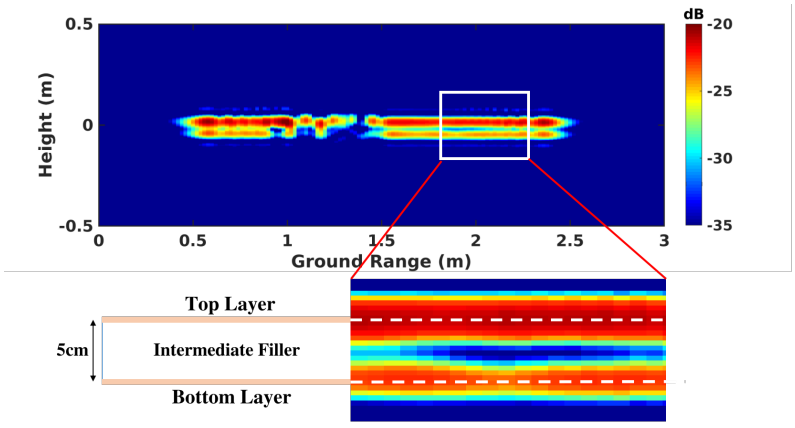

(b) FSC mode

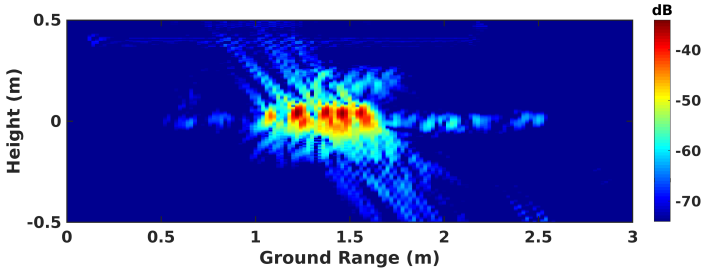

(c) BSC mode

FIGURE 4.7 – Illustration of FSC and BSC scattering mechanisms with focused images of metal handles lying on a wooden floor at X band

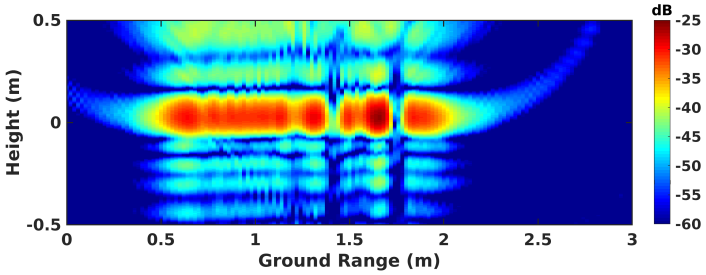

(a) FSC

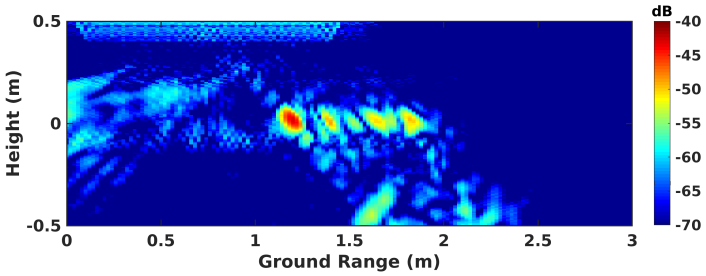

(b) BSC

FIGURE 4.8 – Illustration of FSC and BSC scattering mechanisms with focused images of metal handles lying on a wooden floor at C band

non-uniform profile, attributed to the variations of transmission delay induced by the uneven shape and varying density of VTBC. One may note that the presence of the delayed ground echo is specific to the test environment, which features wooden floors in this study. In practical experiments conducted over real pavement in [Wu+23b], the response of the ground echo is not observed. Figure 4.9d shows that unlike nadir looking and FSC modes, in BSC mode, the measured echos are affected by the speckle effect.

Compared with VTBC, STBC has more homogeneous characteristics and stable geometry. The delayed ground echo is located at a lower elevation with reduced reflectivity, due to the larger thickness of STBC, as illustrated in Fig. 4.10b and 4.10c. In BSC mode, double bounce effects are observed at the edges of STBC, resulting in two pronounced scattering centers, as indicated in Fig. 4.10d.

For monolayer slabs, FSC mode achieves comparable performance compared with nadir-looking GPR for characterizing vertical structures. Images obtained in BSC mode are affected by speckle and the double-bounce effect and may be considered unusable by themselves. These results for monolayer slabs provide references for the following experiments involving complex pavement conditions with bilayer slabs and artificial cracks

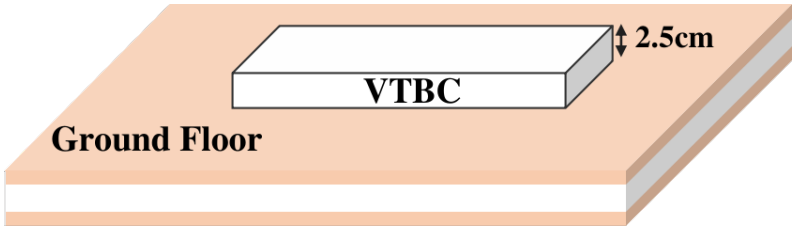

(a) Geometrical configuration

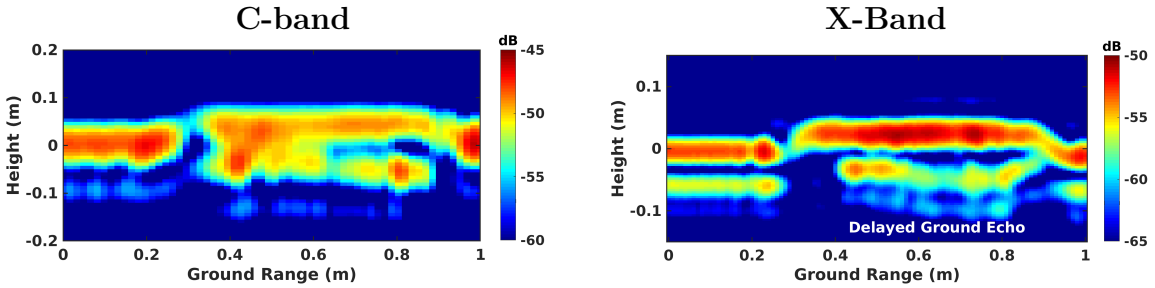

(b) Nadir looking

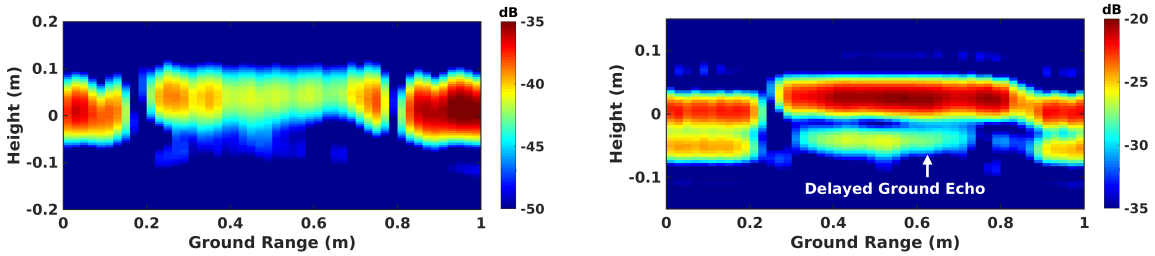

(c) FSC mode

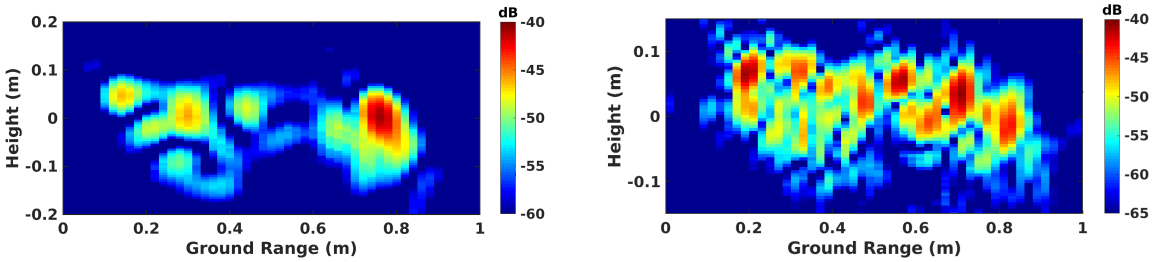

(d) BSC mode

FIGURE 4.9 – Focusing results over VTBC

4.4.3 Horizontal crack

The bilayer HMA, made of compacted VTBC and STBC slabs, appears as a uniform medium without a crack, in the image displayed in Fig. 4.11b. A horizontal crack, represented as a detachment at the tack-coat interface, is modeled by directly placing VTBC on top of STBC, as shown in Fig. 4.12a. In comparison to the response of the HMA, the

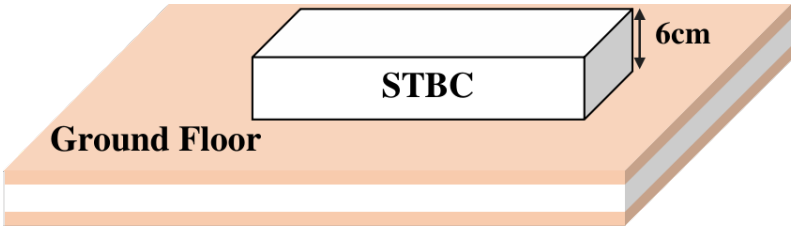

(a) Geometrical configuration

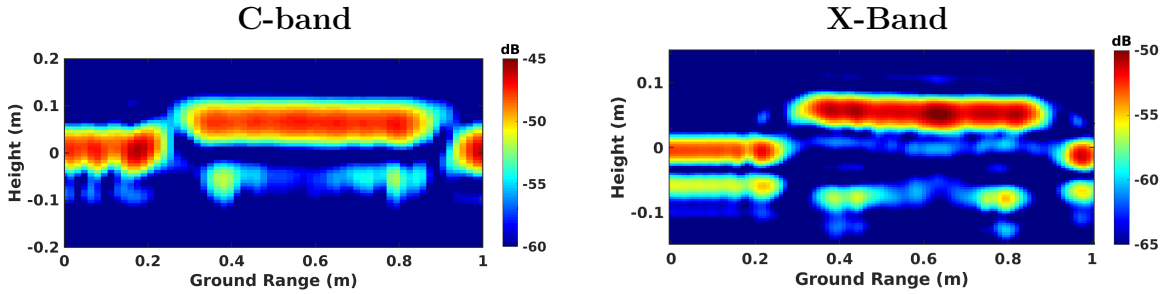

(b) Nadir looking

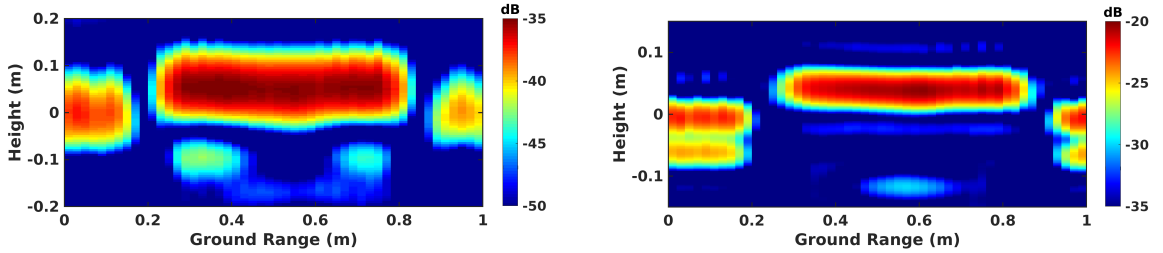

(c) FSC mode

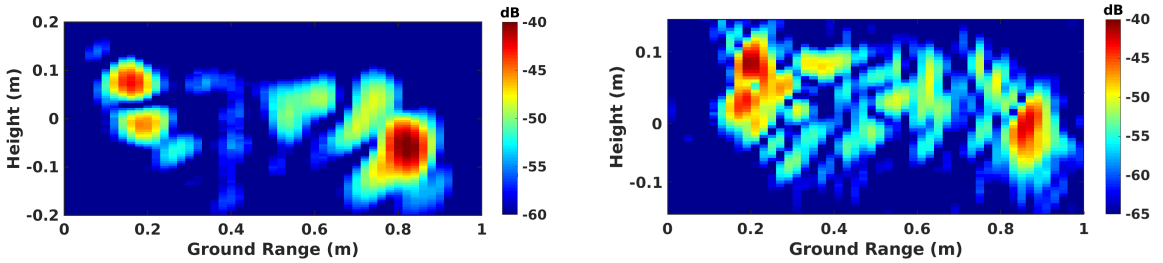

(d) BSC mode

FIGURE 4.10 – Focusing results over STBC

vertical gap is clearly perceived in both nadir-looking GPR and FSC modes at X band, as shown in Fig. 4.12b and 4.12c, respectively. However, at C band, the two slabs may not be distinguished, due to a lack of resolution.

It is important to note that the gap does not appear as a void space, but rather as a line with a pronounced reflectivity in both nadir-looking and FSC modes. The irregular

shape of the lower scattering horizon is attributed to the spatial variation of the density of VTBC. In this specific scenario, BSC mode only provides a basic profile of the slabs without depicting the gap, as illustrated in Fig. 4.12d.

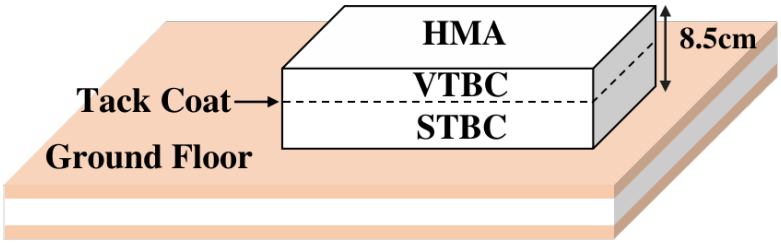

(a) Geometrical configuration

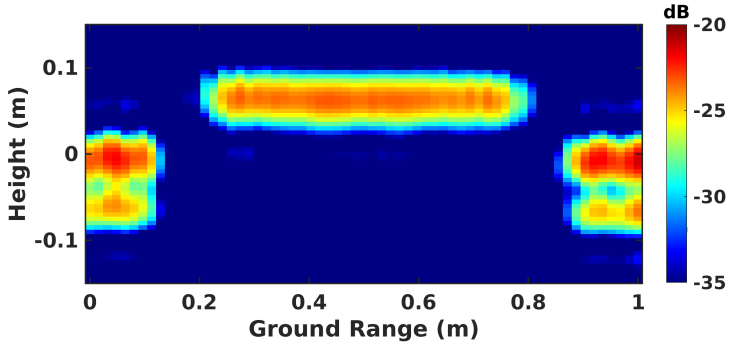

(b) FSC mode

FIGURE 4.11 – Focusing results over HMA

An expanding crack of 5 mm width is built by inserting plastic tabs into the gap, as shown in Fig. 4.13a, rendering it perceptible in the C band images. In both nadir-looking GPR and FSC modes, a stronger contrast between the void space and the response of the bottom layer can be observed in Fig. 4.13c and 4.13b.

FSC mode obtains comparable vertical discrimination with nadir-looking GPR in characterizing horizontal cracks, whose responses are sensitive to variations of the gap width, whereas BSC mode can not provide an effective inspection due to speckle effects.

4.4.4 Vertical crack

A vertical crack is created between two adjacent HMA slabs, as shown in Fig. 4.14a. The horizontal discontinuity is not well detected in the nadir-looking mode, in the image displayed in Fig. 4.14c. A double-bounce scattering mechanism appears at the discontinuity, as illustrated in Fig. 4.14b, resulting in a strong scattering in nadir-looking mode.

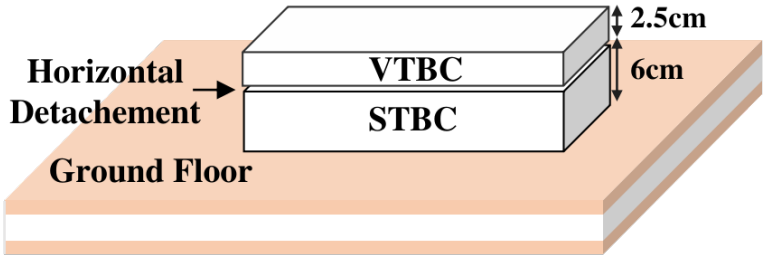

(a) Geometrical configuration

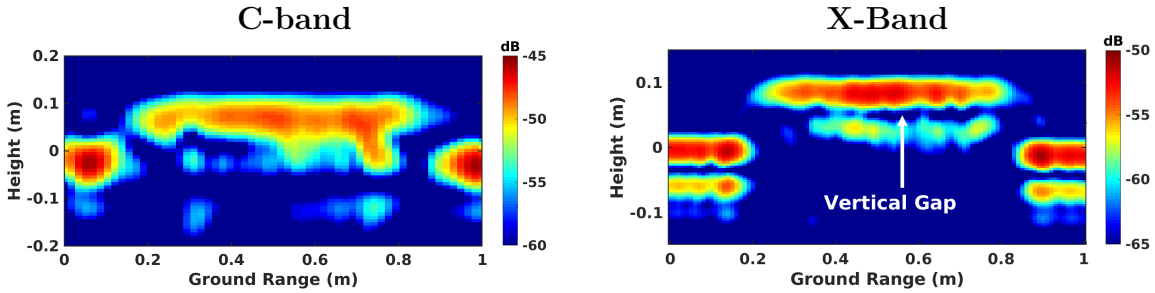

(b) Nadir looking

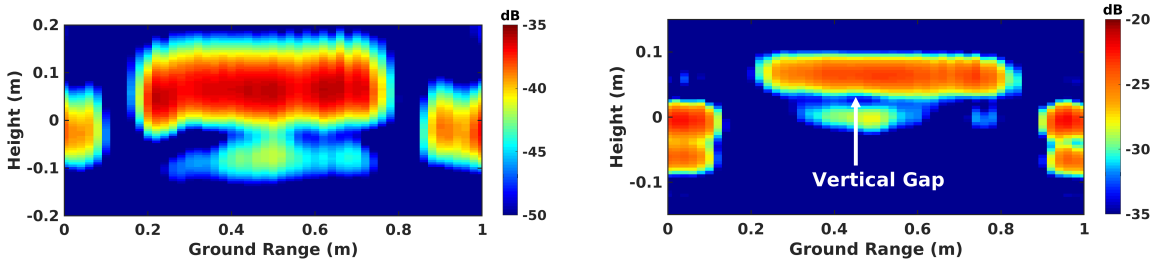

(c) FSC mode

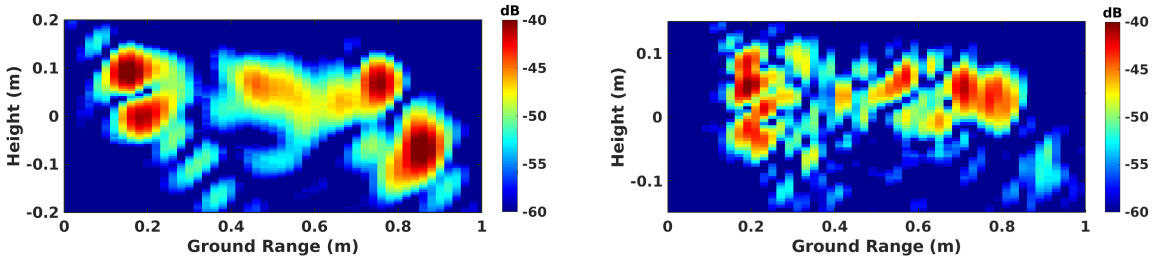

(d) BSC mode

FIGURE 4.12 – Focusing results over a horizontal detachment with <1 mm vertical space

In FSC mode, the vertical crack can be clearly detected and localized at its true position, as depicted in Fig. 4.14d, due to the lack of transmission of waves through the crack within the slab.

Figure. 4.14e displays interesting features obtained in BSC mode, horizontal discon-

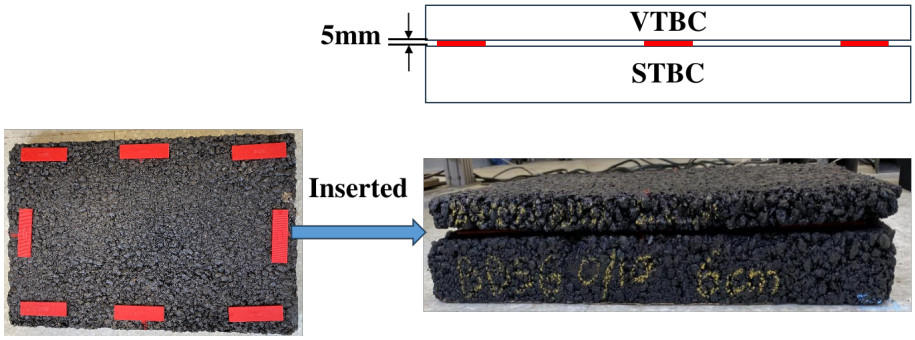

(a) Expanding vertical space by inserting tabs

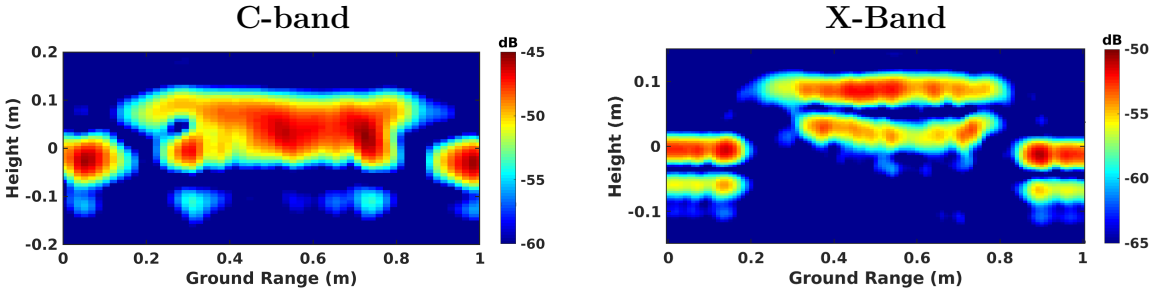

(b) Nadir looking

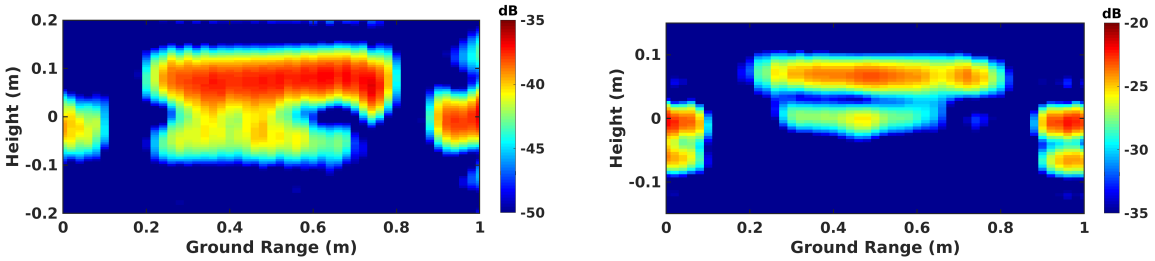

(c) FSC

FIGURE 4.13 – Focusing results over a horizontal detachment with 5mm vertical space

tinuities are clearly localized by the corresponding responses of scatterers, indicating the positions of the gap and slab edges, due to the double bounce effect induced by the vertical crack which explains the low transmitted power in FSC mode [Abd+21]. One may note that the two scatterers on the right side are focused at a slightly lower elevation than the one on the left, due to the transmission delay through the slab.

With the gap width increasing to 5 mm, no observable change can be noticed in nadir-looking and BSC modes, whereas a slight variation can be perceived in FSC mode, and represented by the reduced reflectivity of the void space, as indicated in Fig. 4.15b.

This series of experiments prove that the sliding FSC mode leads to good capability for detecting horizontal discontinuities, while keeping comparable vertical resolution as nadir-

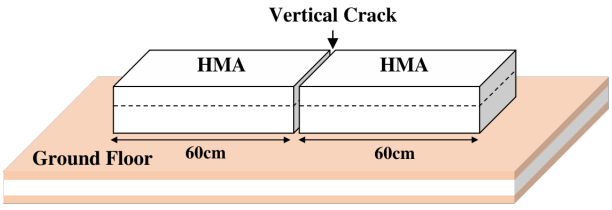

(a) Geometrical configuration

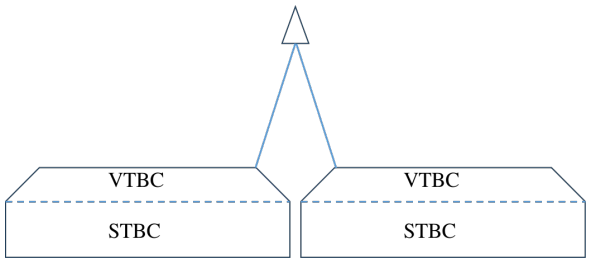

(b) Special geometrical configuration in nadir-looking mode

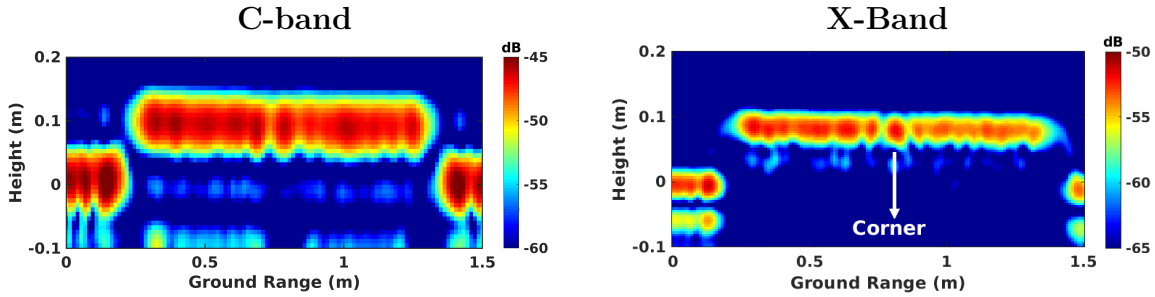

(c) Nadir looking

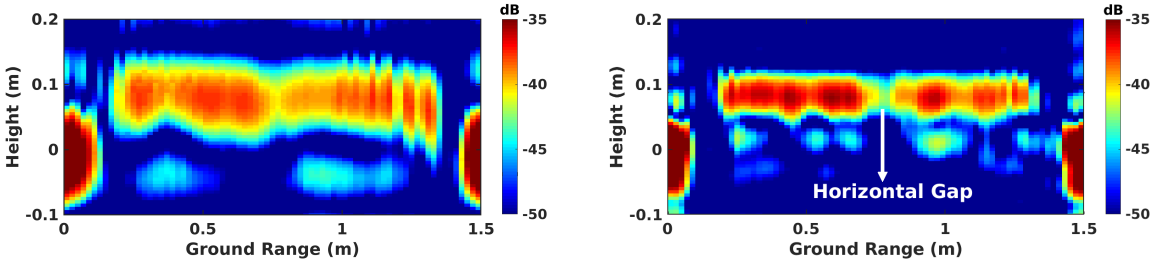

(d) FSC

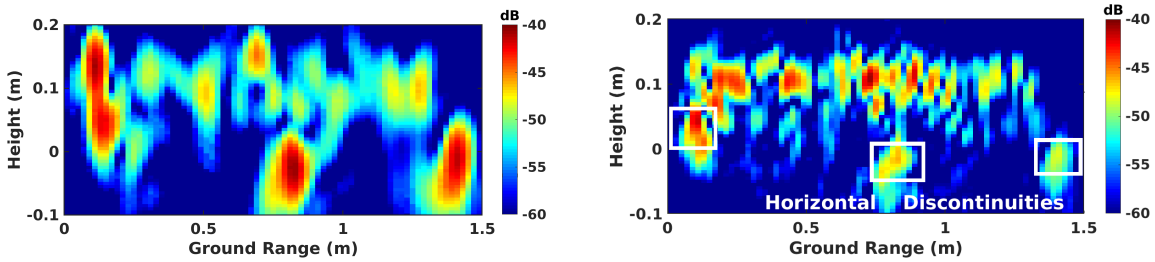

(e) BSC

FIGURE 4.14 – Focusing results over a vertical crack of <1mm width

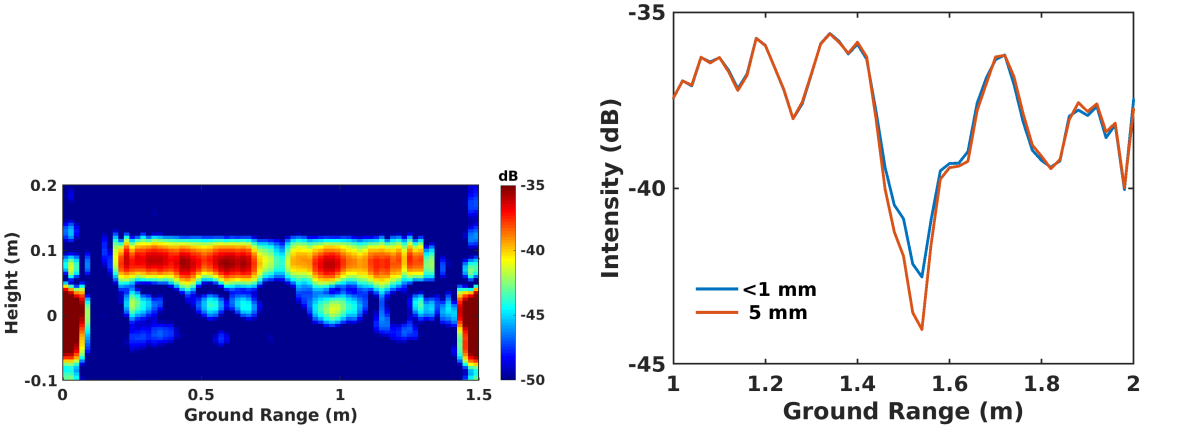

(a) FSC

(b) Comparison of horizontal profiles over the gap

FIGURE 4.15 – Focusing results over a vertical crack of 5mm width

looking GPR, and speckle-free scattering patterns related to quasi-specular scattering mechanisms.

4.4.5 Analysis of polarimetric responses

With HH and VV polarization channels, COSBis system, operated in BSC and FSC modes, can be utilized to investigate the scattering mechanisms and material characteristics using polarimetric diversity.

Permittivity estimation

The radar response of a rough surface, observed at certain angles, exhibits sensitivity to the polarization of incoming waves [UMF81 ; TKD04]. In the context of roadways, which can be regarded as a homogeneous medium with a slightly rough surface, SPM has proven to be a valid approach for estimating their scattering characteristics with respect to polarimetric responses, as demonstrated in [Wu+23b ; WFW21].

SPM characterizes the polarization amplitude α_{HH} and α_{VV} in relation to the relative dielectric permittivity ε_r in FSC mode, with $\phi = 0$ and the relative magnetic permeability $\mu = 1$, as used in (3.11).

The ratio of polarization scattering intensity can be represented by $|\frac{\alpha_{HH}}{\alpha_{VV}}|^2$, as a function of relative dielectric constant ε_r, the incidence angle θ_1 and the scattering one θ_2. In

the sliding FSC mode, θ_1 and θ_2 correspond to the antenna physical orientation as the processed angular aperture remains small.

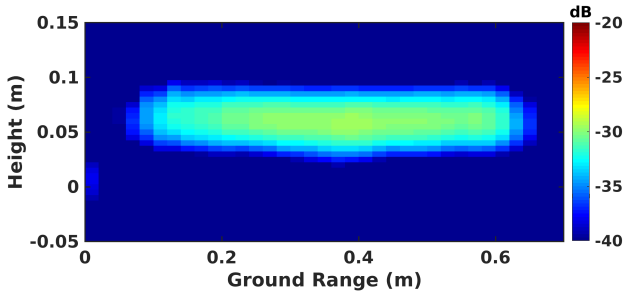

(a) FSC mode in VV polarization over STBC

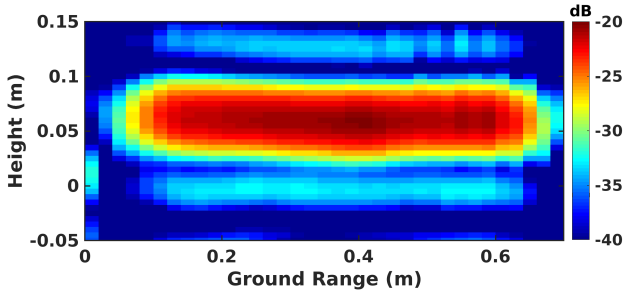

(b) FSC mode in HH polarization over STBC

FIGURE 4.16 – Permittivity estimation with FSC focusing results in HH and VV polarizations over STBC

The approach is implemented at X band on the STBC slab, due to its homogeneous dispersive properties, as shown in Fig. 4.16. In the considered case, the value of the polarization ratio is estimated to be 9.45 dB at observing angles ($\theta_1 = 45°, \theta_2 = 45°$). The estimated relative permittivity of STBC is $\varepsilon_r = 5$, which is consistent with both the value of the constituent aggregates mentioned in 4.3.2 and the electromagnetic characterization reported in [Ado06].

Analysis of discrimination disparities under different polarizations

The capabilities of HH and VV COSBis images for discriminating vertical and horizontal structures are investigated in the following. The echos corresponding to the top and bottom layers of the ground floor can not be separated in VV polarization, whereas they are clearly distinguished in HH polarization, as shown in Fig. 4.17a and 4.17c. This

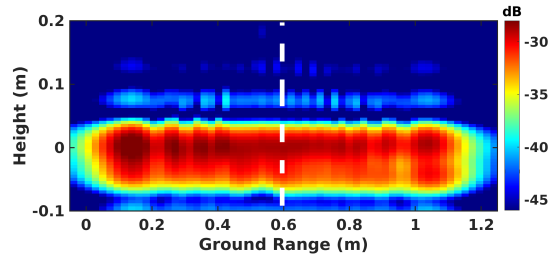

(a) VV polarization over the ground floor

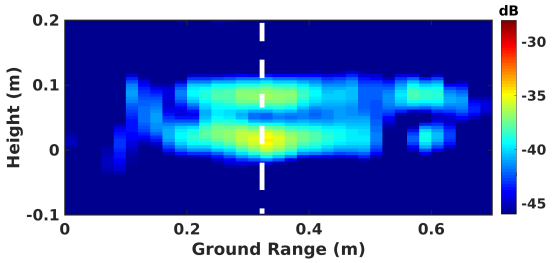

(b) VV polarization over the vertical gap

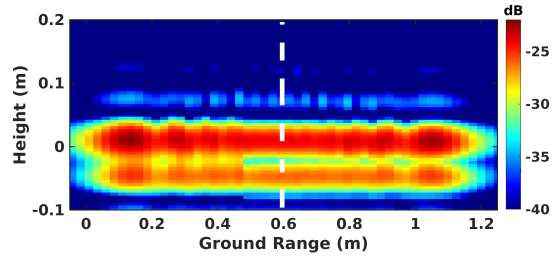

(c) HH polarization over the ground floor

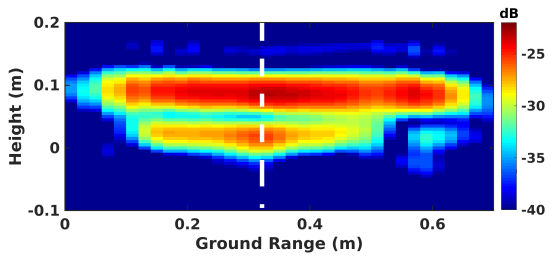

(d) HH polarization over the vertical gap

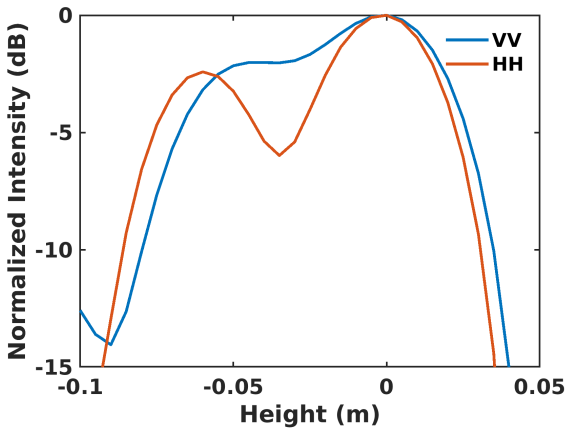

(e) Normalized vertical profiles over the ground floor

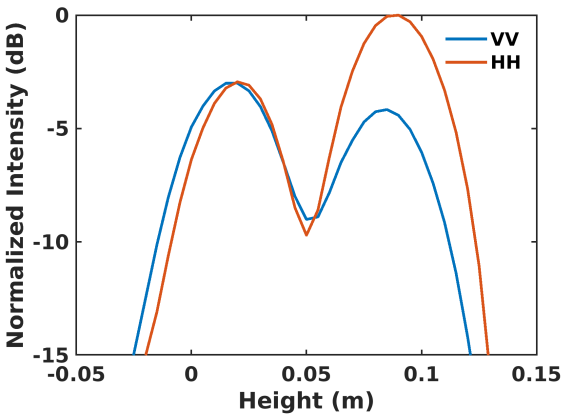

(f) Normalized vertical profiles over the vertical gap

FIGURE 4.17 – HH and VV polarization images in FSC mode. 1-D normalized profiles (e) and (f) are acquired along the white dash lines in (a)(c) and (b)(d), correspondingly.

difference of vertical discrimination is clearly illustrated with the normalized vertical profiles over the floor, acquired along white dashed lines in Fig. 4.16a and 4.16b, as depicted in Fig. 4.17e.

Similarly, in the case of a horizontal detachment between VTBC and STBC, as illustrated in Fig. 4.17b and 4.17d, the presence of a vertical gap is well discerned in HH polarization, whereas VV polarization yields a less obvious features. Figure. 4.17f exhibits a 10-dB contrast between responses from the slabs and the void space by employing HH channels, providing better discrimination than the one with a contrast of 6 dB in VV channel.

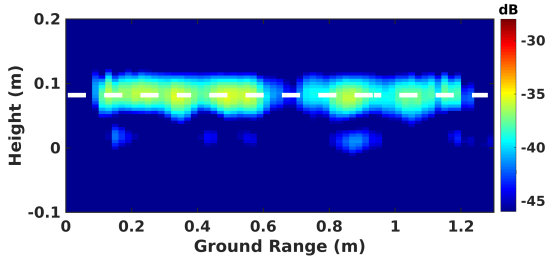

(a) VV polarization over the horizontal gap

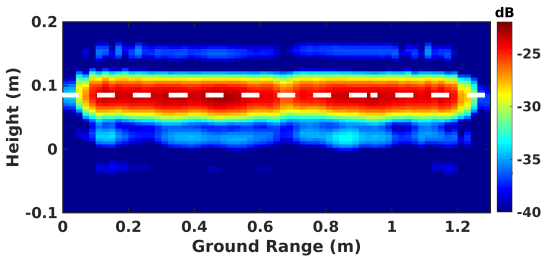

(b) HH polarization over the horizontal gap

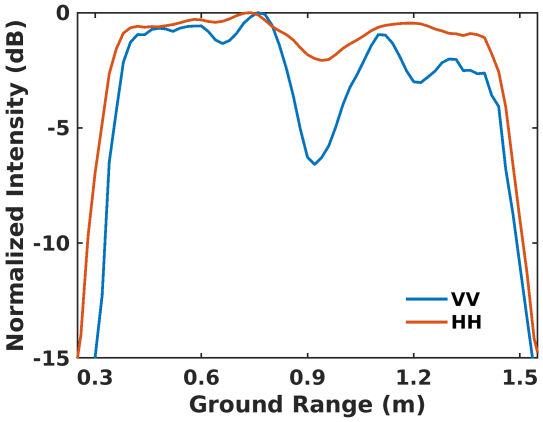

(c) Normalized horizontal profiles over the horizontal gap

FIGURE 4.18 – HH and VV polarization images in FSC mode. 1-D normalized profiles in (c) are acquired along the white dash lines in (a) and (b).

In contrast, a distinct phenomenon may arise in the case of a vertical crack between two HMA slabs, as shown in Figs. 4.18a and4.18b. The discontinuity is distinctly perceived in VV polarization, demonstrating better horizontal discrimination than the one relative HH response, as depicted in Fig. 4.18c. In the sliding FSC mode, HH polarization demonstrates

superior sensitivity to vertical discrimination, while VV polarization excels in detecting horizontal discontinuities.

Double-bounce effect

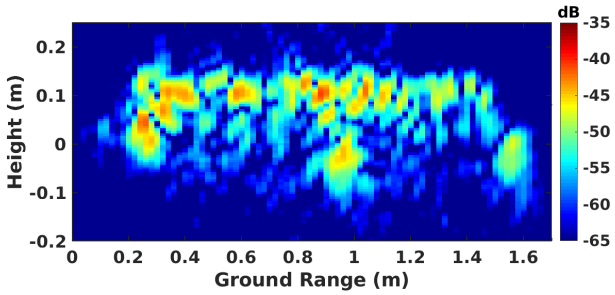

(a) VV polarization

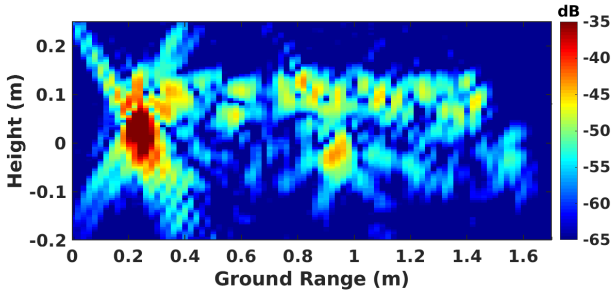

(b) HH polarization

FIGURE 4.19 – Comparison of BSC focusing results in HH and VV polarizations over the horizontal gap

In BSC mode, a much stronger response is observed at the first discontinuity in HH polarization, as indicated in Fig. 4.19b, whereas the reflectivity of other parts remains equivalent to the one in VV polarization, as depicted in Fig. 4.19a. This is due to a typical double-bounce effect of BSC mode at the boundary between the ground and the volume [Abd+21].

4.5 Conclusion

In this chapter, a novel imaging technique of sliding bistatic SAR for pavement inspection and characterization is presented, through the utilization of a simple structure consisting of a single pair of opposite-side looking Tx and Rx antennas, sliding along the

ground-range direction. This configuration achieves good horizontal discrimination by exploiting the created angular aperture, while maintaining a constant vertical resolution. The evaluation of the proposed configuration using measurements from a GB-SAR system, COSBis, operated in both VV and HH polarizations, focuses on detecting underground targets and cracks in both vertical and horizontal orientations.

Results demonstrate that the sliding FSC mode effectively obtains a vertical resolution comparable to that of nadir-looking GPR over horizontal cracks, and is sensitive to the variation of the gap width. Moreover, the unique horizontal discrimination capability of FSC mode allows for clear perception and accurate localization of vertical cracks. The use of polarimetric diversity enables the estimation of dielectric permittivity over slightly rough asphalt layers. Notably, the observations revealed interesting differences in polarimetric channels, where the HH polarization response exhibits higher sensitivity to vertical discrimination, whereas VV polarization is more perceptive of horizontal discontinuities.

Based on the findings, COSBis proves to be a valuable alternative configuration for pavement characterization and diagnosis, offering a simple structure with good discrimination in both vertical and horizontal directions, and sensitivity to polarimetry diversity. Both measurement results and theoretical analysis confirm the feasibility of the proposed method, emphasizing its potential for further research and optimization of capabilities for various applications.

Chapitre 5

Bistatic imaging using high-resolution spectral estimation techniques

Contents

5.1 Introduction 111
5.2 Generic signal model 112
5.2.1 Simple model for a non dispersive medium 112
5.2.2 Stochastic aspects 113
5.2.3 Spectral smoothing 114
5.3 Spectral estimation methods 117
5.3.1 Nonparametric methods 118
5.3.2 Parametric methods 118
5.3.3 Spectral estimation applied to defects inspection using a nadir-looking GPR 119
5.4 High-resolution imaging techniques applied in the COSBis configuration 120
5.4.1 Principles of COSBis focusing using spectral estimation methods 120
5.4.2 Horizontal crack 123
5.4.3 Vertical crack 125
5.5 Conclusion 126

5.1 Introduction

The COSBis configuration, introduced in the preceding chapter, has emerged as a good solution and low complexity for the comprehensive characterization of pavement

structures and the thorough inspection of embedded defects, including both vertical and horizontal cracks.

This chapter aims to evaluate the capabilities of the COSBis mode when operated in conjunction with high-resolution techniques. This strategic integration seeks to extract even more intricate details through spectral estimation, while addressing the diminishing vertical discrimination encountered in VV polarization.

5.2 Generic signal model

5.2.1 Simple model for a non dispersive medium

Consider the 1-D imaging of multiple scatterers using a set of monochromatic acquisitions performed at N_ν regularly distributed spectral coordinates

$$\nu_k = \nu_0 + k\ \mathrm{d}\nu \quad \text{with} \quad k = 0, \ldots, N_\nu - 1 \tag{5.1}$$

The signal measured at a given spectral position, ν_k, when observing a set of N_s sources, may be written under the first order Born approximation, as

$$y(\nu_k) = \sum_{i=0}^{N_s-1} a_{c_i}\, \mathrm{e}^{j2\pi\nu_k \frac{2d_i}{c}} + w(\nu_k) = x(\nu_k) + w(\nu_k) \tag{5.2}$$

where a_{c_i} stands for the complex reflection coefficient of the i^{th} source, assumed to be constant over the whole spectral domain, whereas d_i represents its distance to the radar. The term $w(\nu_k)$ is the acquisition noise. The whole measurement may be represented under the form of an N_ν-element vector, given by $[\mathbf{y}]_k = y(\nu_k)$, as

$$\mathbf{y} = \mathbf{x} + \mathbf{w} = \sum_{i=0}^{N_s-1} s_i \mathbf{a}(f_i) + \mathbf{w} \tag{5.3}$$

where $s_i \triangleq a_{c_i}\, \mathrm{e}^{j4\pi\nu_0 \frac{d_i}{c}}$, and

$$\mathbf{a}^T(f_i) = [1, \mathrm{e}^{j2\pi f_i}, \ldots, \mathrm{e}^{j2\pi(N_\nu-1)f_i}] \quad \text{with} \quad f_i = 2\frac{d_i}{c}\mathrm{d}\nu \tag{5.4}$$

representing the steering vector. The model given in (5.3) can be expressed by using a steering matrix $\mathbf{A}$, as

$$\mathbf{y} = \mathbf{A}\mathbf{s} + \mathbf{w} \tag{5.5}$$

where

$$\mathbf{A} = \Big[\mathbf{a}(f_0), \ldots, \mathbf{a}(f_{N_s-1})\Big] \quad \text{and} \quad \mathbf{s}^T = [s_0, \ldots, s_{N_s-1}] \tag{5.6}$$

with $\mathbf{s}$ the complex source vector.

5.2.2 Stochastic aspects

Data covariance matrix

The stochastic behavior of a 1-D measurement is generally represented from (5.5) as

$$\mathbf{y}(l) = \mathbf{x}(l) + \mathbf{w}(l) = \mathbf{A}\mathbf{s}(l) + \mathbf{w}(l) \tag{5.7}$$

where l represents a specific realization of the acquisition. The stochastic model, as expressed in (5.7), makes the assumption that the distance of a scatterer d_i remains constant, and that its response s_i does not change over the spectral domain, but may vary from one realization to another. The characterization of the received signal is often performed using the non-centered covariance matrix of the acquired signal $\mathbf{R_{yy}} = \mathrm{E}(\mathbf{y}\mathbf{y}^H)$. The noise component is generally assumed to follow a central normal distribution, represented as $\mathbf{w} \sim \mathcal{N}(\mathbf{0}, \mathbf{R_{ww}})$, exhibiting a white covariance matrix.

$$\mathrm{E}(\mathbf{w}) = \mathbf{0},\ \mathbf{R_{ww}} = \sigma_w^2 \mathbf{I}_{N_\nu},\ \mathrm{E}([\mathbf{w}]_m [\mathbf{s}]_n^*) = 0\ \forall m, n \tag{5.8}$$

Under these conditions, the data covariance matrix can be written as

$$\begin{aligned}
\mathbf{R_{yy}} = \mathrm{E}(\mathbf{y}\mathbf{y}^H) &= \mathrm{E}\left(\sum_{m=0}^{N_s-1} s_m \mathbf{a}(f_m) \sum_{n=0}^{N_s-1} s_n^* \mathbf{a}^H(f_n)\right) + \sigma_w^2 \mathbf{I}_{N_\nu} \\
&= \sum_{m=0}^{N_s-1} p_m \mathbf{a}(f_m)\mathbf{a}^H(f_m) + \sum_{m=0}^{N_s-1} \sum_{n=0, n\neq m}^{N_s-1} \sqrt{p_m p_n}\rho_{mn} \mathbf{a}(f_m)\mathbf{a}^H(f_n) + \sigma_w^2 \mathbf{I}_{N_\nu} \\
&= \mathbf{A}\mathbf{R_{ss}}\mathbf{A}^H + \sigma_w^2 \mathbf{I}_{N_\nu}
\end{aligned} \tag{5.9}$$

where the source covariance matrix verifies

$$\mathbf{R_{ss}}(m,n) = \mathrm{E}(s_m s_n^*) = \sqrt{p_m p_n}\rho_{mn} \quad \text{with} \quad |\rho_{mn}| \leq 1,\ \rho_{mm} = 1 \tag{5.10}$$

Stochastic models

Conditional Model (CM) Under the CM assumption, the reflection coefficients remain constant over all realizations, i.e. $s_m(l) = s_m,\ \forall m$. Consequently, $\mathbf{y} \sim \mathcal{N}(\mathbf{As}, \sigma_w^2 \mathbf{I}_{N\nu})$. This situation can be accommodated by considering a unitary-rank source covariance matrix $\mathbf{R_{ss}} = \mathbf{ss}^H$, where $|\rho_{mn}| = 1,\ \forall m,n$. The term unitary rank signifies that only a single eigenvalue of $\mathbf{R_{ss}}$ is non-zero, precisely equal to $\mathbf{s}^H\mathbf{s}$. If the number of sources, N_s is known, as it cannot be estimated from $\mathbf{R_{yy}}$, the distinctive structure of $\mathbf{a}(f_i)$ allows for the separation of different components, for instance, through the application of the deterministic Maximum Likelihood (ML) estimation approach [KV96 ; Ott+93].

Unconditional Model (UM) In the UM condition, the reflection coefficients vary randomly over the realizations, and are generally assumed to follow a central normal distribution, characterized by a full-rank covariance matrix. Hence $\mathbf{y} \sim \mathcal{N}(\mathbf{0}, \mathbf{AR_{ss}A}^H + \sigma_w^2 \mathbf{I}_{N_\nu})$,. The separation of the various components must then be carried out based on the estimate of $\mathbf{R_{yy}}$, often through the application of the stochastic ML estimation approach [KV96 ; Ott+93 ; Mar+98].

5.2.3 Spectral smoothing

Forward Spectral Smoothing

In the 1-D imaging case studied in this chapter, the CM applies. Subspace orthogonality-based techniques, such as MUSIC, cannot be applied, due to the rank deficiency of $\mathbf{R_{ss}}$. One might attempt to find a compromise between rank improvement and Fourier-focusing resolution by splitting the original spectral range, or array, into subspectra, or subarrays. All of these subsets can then be considered as realizations of $\mathbf{y}$.

Consider a sub-vector covariance matrix estimated with Spectral Smoothing Preprocessing (SSP) as

$$\hat{\mathbf{R}}_{SSP} = \frac{1}{L}\sum_{l=0}^{L-1} \tilde{\mathbf{y}}(l)\tilde{\mathbf{y}}^H(l) \tag{5.11}$$

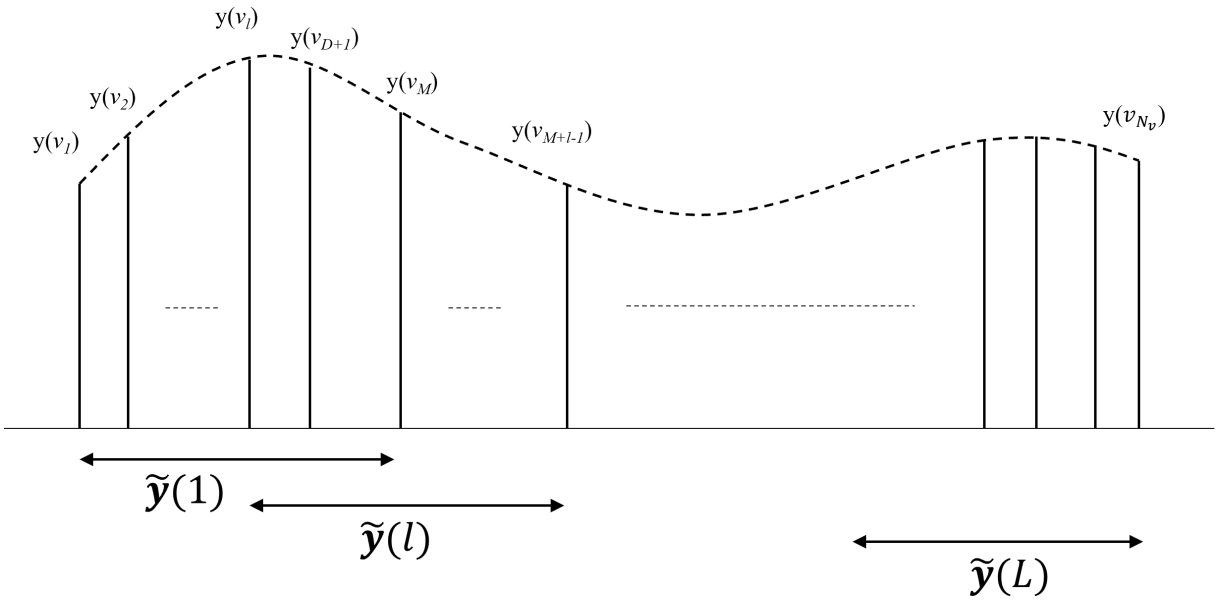

FIGURE 5.1 – Subarrays of SSP method

with

$$\tilde{\mathbf{y}}^T(l) = \Big[[\mathbf{y}]_l, \ldots, [\mathbf{y}]_{l+M-1}\Big] \text{ with } M \in \mathbb{N}^{*+} \tag{5.12}$$

where M is the length of a sub-array.

According to (5.3), $\tilde{\mathbf{y}}$ can be rewritten as :

$$\tilde{\mathbf{y}}(l) = \sum_{i=0}^{N_s-1} \tilde{s}_i(l)\tilde{\mathbf{a}}(f_i) + \tilde{\mathbf{w}} \tag{5.13}$$

where $\tilde{s}_i(l) \triangleq s_i\, \mathrm{e}^{j2\pi l f_i}$, and

$$\tilde{\mathbf{a}}^T(f_i) = [1, \mathrm{e}^{j2\pi f_i}, \ldots, \mathrm{e}^{j2\pi(M-1)f_i}] \quad \text{where} \quad f_i = 2\frac{d_i}{c}\mathrm{d}\nu \tag{5.14}$$

Hence, the subarray covariance matrix can be expressed as :

$$\begin{aligned}\widehat{\mathbf{R}}_{\widetilde{\mathbf{y}}\widetilde{\mathbf{y}}} &= \sum_{m=0}^{N_s-1} p_m \tilde{\mathbf{a}}(f_m)\tilde{\mathbf{a}}^H(f_m) + \frac{1}{L}\sum_{l=0}^{L-1}\sum_{m=0}^{N_s-1}\sum_{n=0,n\neq m}^{N_s-1} \sqrt{p_m p_n}\rho_{mn}\, \mathrm{e}^{j2\pi l f_{mn}}\, \tilde{\mathbf{a}}(f_m)\tilde{\mathbf{a}}^H(f_n) + \sigma_w^2\mathbf{I}_M \\ &= \widetilde{\mathbf{A}}\widehat{\mathbf{R}}_{\widetilde{\mathbf{s}}\widetilde{\mathbf{s}}}\widetilde{\mathbf{A}}^H + \sigma_w^2\mathbf{I}_M\end{aligned} \tag{5.15}$$

where $f_{mn} = f_m - f_n$ and $L + M - 1 = N_\nu$, and finally

$$\widehat{\mathbf{R}}_{\mathbf{ss}}(m,n) = \mathbf{R}_{\mathbf{ss}}(m,n)\frac{1}{L}\sum_{l=0}^{L-1} e^{j2\pi l f_{mn}} \tag{5.16}$$

The modified correlation coefficient can also be written as :

$$\hat{\rho}_{mn} = \rho_{mn}\frac{1}{L}\sum_{l=0}^{L-1} e^{j2\pi l f_{mn}} = \rho_{mn}\frac{\sin(\pi L f_{mn})}{L\sin(\pi f_{mn})}e^{j\pi(L-1)f_{mn}} \tag{5.17}$$

$$|\hat{\rho}_{mn}| = |\rho_{mn}|\left|\frac{\sin(\pi L f_{mn})}{L\sin(\pi f_{mn})}\right| = |\rho_{mn}|\left|\frac{\sin\left(\pi L\frac{\alpha_{mn}}{N_\nu}\right)}{L\sin\left(\pi\frac{\alpha_{mn}}{N_\nu}\right)}\right| \tag{5.18}$$

where $\alpha_{mn} = N_\nu f_{mn}$, defined as the lag between sources m and n in terms of the resolution cell, which is the ratio used to evaluate resolution. Consequently, the value of the source correlation $\hat{\rho}_{mn}$ can be estimated as a function of the relative values of L or M, and α_{mn} in equation (5.18). The variation of $\hat{\rho}_{mn}$ with the subarray ratio of M/N_ν changes with different resolution ratios α_{mn} are illustrated in Fig. 5.2. One may note, the reduction of subarray ratio M/N_ν within a fixed frequency band results in the decorrelation between sources, indicated by the decreased correlation coefficient $\hat{\rho}_{mn}$. However, this reduction comes at the cost of diminished resolution α_{mn}. Therefore, it is essential to strike a balance between resolution and correlation.

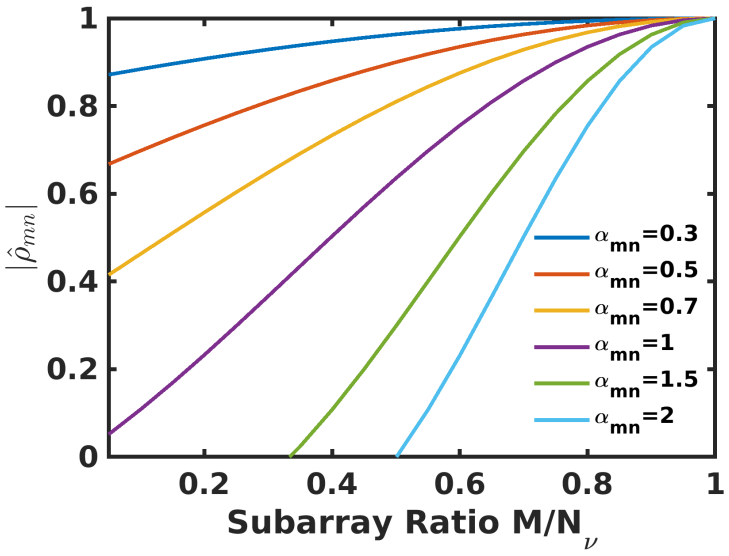

FIGURE 5.2 – Variation of correlation coefficient $\hat{\rho}_{mn}$ and resolution α_{mn} in the case of $\rho_{mn} = 1$

Forward-Back Spectral Smoothing

Based on SSP, the forward-back spectral smoothing is implemented as a Modified Spectral Smoothing Preprocessing (MSSP) to make further decorrelation.

$$\mathbf{R}_{\mathbf{yy}l} = \mathbf{R}_{\mathbf{yy}}(l : l + M - 1, l : l + M - 1), l = 1....L \tag{5.19}$$

$$\widehat{\mathbf{R}}_{\mathbf{yy}\_MSSP} = \frac{1}{2L}\sum_{l=1}^{L}(\mathbf{R}_{\mathbf{yy}l} + \mathbf{J}\mathbf{R}_{\mathbf{yy}l}^{H}\mathbf{J}) \tag{5.20}$$

where $\mathbf{J}$ is an inverse identity matrix. Considering $\mathbf{J}\tilde{\mathbf{a}}(f_i) = e^{j2\pi(M-1)f_i}\tilde{\mathbf{a}}(-f_i)$, the estimation covariance matrix can be expreseed as :

$$\begin{aligned}\widehat{\mathbf{R}}_{yy\_MSSP} = \sum_{m=0}^{N_s-1} p_m\tilde{\mathbf{a}}(f_m)\tilde{\mathbf{a}}^H(f_m) + \frac{1}{2L}\sum_{l=0}^{L-1}\sum_{m=0}^{N_s-1}\sum_{n=0,n\neq m}^{N_s-1}\sqrt{p_m p_n}(\rho_{mn}\,\mathrm{e}^{j2\pi l f_{mn}}\,\tilde{\mathbf{a}}(f_m)\tilde{\mathbf{a}}^H(f_n) + \\ \rho_{mn}^{*}\,\mathrm{e}^{j2\pi(M+l-1)f_{mn}}\,\tilde{\mathbf{a}}(f_m)\tilde{\mathbf{a}}^H(f_n)) + \sigma_w^2\mathbf{I}_M\end{aligned} \tag{5.21}$$

Given that the reflection coefficients of sources are equal $a_{c_m} = a_{c_n}$, then $\rho_{mn} = \rho_{mn}^{*}$. Therefore, the correlation coefficient of MSSP can be written as :

$$\begin{aligned}\hat{\rho}_{mn\_MSSP} &= \frac{1}{2L}\rho_{mn}\sum_{l=0}^{L-1}(e^{j2\pi l f_{mn}} + \mathrm{e}^{j2\pi(M+l-1)f_{mn}}) \\ &= \rho_{mn}\frac{\sin(\pi L f_{mn})}{L\sin(\pi f_{mn})}\frac{e^{j\pi(L-1)f_{mn}} + e^{j\pi(M+L-2)f_{mn}}}{2}\end{aligned} \tag{5.22}$$

$$\begin{aligned}|\hat{\rho}_{mn\_MSSP}| &= |\rho_{mn}|\left|\frac{\sin\left(\pi L\frac{\alpha_{mn}}{N_\nu}\right)}{L\sin\left(\pi\frac{\alpha_{mn}}{N_\nu}\right)}\right||\cos(\pi\alpha_{mn}(N_\nu + 2\nu_0)/N_\nu)| \\ &= |\hat{\rho}_{mn\_SSP}|\,|\cos(\pi\alpha_{mn}(N_\nu + 2\nu_0)/N_\nu)| \leq |\hat{\rho}_{mn\_SSP}|\end{aligned} \tag{5.23}$$

which indicates that MSSP consistently demonstrates better performance in terms of decorrelation effect compared with SSP.

5.3 Spectral estimation methods

Spectral estimation is an essential concept in signal processing and statistics that deals with the estimation of the frequency content or spectral characteristics of a signal

[SM+05 ; Mar+98 ; KV96]. The ability to separate two or more closely spaced scatterers is mainly affected by SNR, the resolution of analysis, and the kind of observed target responses (stochastic or deterministic/correlated or uncorrelated,...). [Sau+11 ; HFR12]. As a fundamental process in signal processing that entails estimating the Power Spectral Density (PSD), spectral estimation can be achieved through two primary methodologies : nonparametric and parametric methods.

5.3.1 Nonparametric methods

Nonparametric methods do not impose any specific assumptions about the underlying statistical model governing the signal. Instead, they directly estimate PSD or spectral content from the data.

From this category, one can cite the beamforming and the Capon techniques, also known as the adaptive beamformer [SM+05 ; Cap69]. Beamforming is equivalent to the Fourier transform, whereas the Capon technique follows a constrained optimization, which aims to minimize interference between different sources. The resolution of beamforming is generally coarse, as it is related to the bandwidth of the measured signals, whereas Capon's resolution is generally better. Both techniques can be implemented using a 1-D search, and the peaks of the estimated reflectivity indicate the location of the targets.

The power spectral density estimate of beamforming, $P_{\mathrm{BF}}(f)$ and Capon, $P_{\mathrm{CP}}(f)$, are given by

$$\begin{aligned} P_{\mathrm{BF}}(f) &= \mathbf{a}^H(f)\hat{\mathbf{R}}\mathbf{a}(f) \\ P_{\mathrm{CP}}(f) &= \frac{1}{\mathbf{a}^H(f)\hat{\mathbf{R}}^{-1}\mathbf{a}(f)} \end{aligned} \tag{5.24}$$

5.3.2 Parametric methods

The parametric methods rely on a model of the measured signal. The model described in (5.3) is particularly powerful. It is referred to as the line spectrum, as it corresponds to a set of monochromatic terms located at different frequencies, resulting in a signal that occupies a small subspace. Hence, high-resolution methods, relying on the low dimensionality of this subspace, can be implemented. The particularity lies in their ability to discriminate sources separated by a spectral distance much smaller than the classical Fourier resolution. The quality of the estimation depends on the accuracy of the covariance matrix estimation. In general, high-resolution techniques rely on a multidimensional

optimization process aimed at determining the parameters of each source.

One may note some interesting techniques such as MUSIC and ESPRIT, which can achieve high resolution at a highly reduced computational cost. MUSIC is based on a 1-D search technique, it requires computing the eigenvector decomposition of the covariance matrix [Sch86]. ESPRIT is also widely used as it allows for determining the characteristics of targets without any search, simply by employing the eigenvector decomposition of the covariance matrix [RK89]. One may note that ESPRIT requires to deal with uniformly sampled signals.

The MUSIC cost function is given by

$$P_{\text{MUSIC}}(f) = \frac{1}{\mathbf{a}^H(f)\mathbf{U}_N\mathbf{U}_N^H\mathbf{a}(f)} \tag{5.25}$$

where $\mathbf{U}_N$ contains the eigenvectors of the covariance matrix spanning the subspace that is orthogonal to the one containing the contribution of different scatters.

5.3.3 Spectral estimation applied to defects inspection using a nadir-looking GPR

Spectral estimation methods are applied to nadir-looking GPR in order to detect the sand-defect layer shown in Fig. 5.3, which is a light defect hard to discriminate in the original images. At C band, from the original 1-D profiles displayed in Fig. 5.4a, the

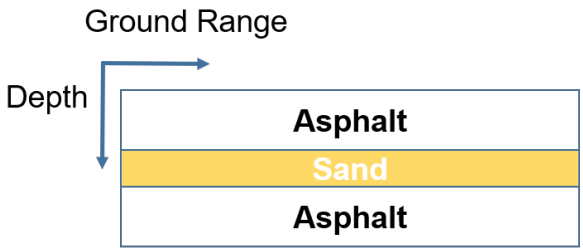

FIGURE 5.3 – Structure of the sand-defect zone

response attributed to the sand defect is discernible albeit with high variability and a relatively low SNR. By employing the nonparametric beamforming spectral estimation method, the noise level is lowered at the cost of a worse resolution, leading to enhanced discrimination of the defect response. However, at X band, the echo of the sand layer is completely mixed with the sidelobe of the main ground response, and little improvement may be obtained with the beamforming method, as indicated in Fig. 5.4b.

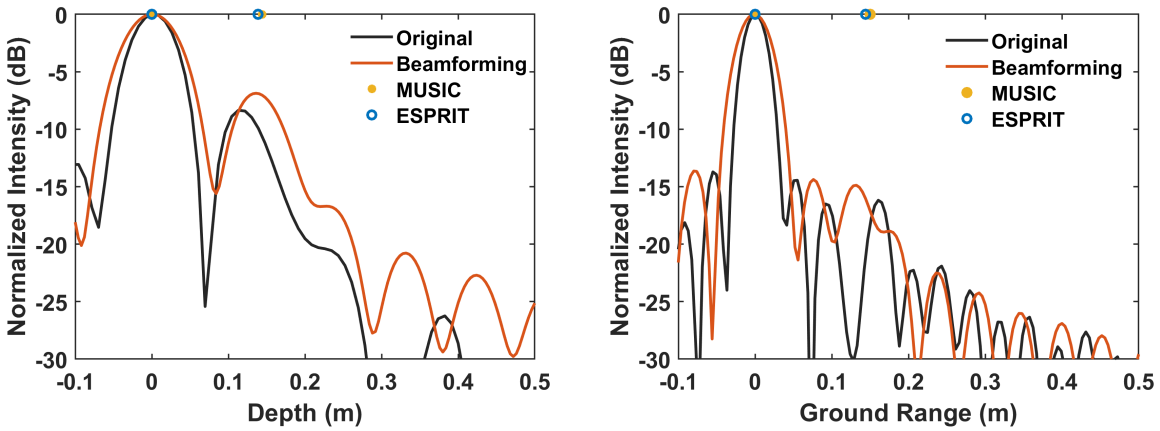

(a) C band **(b)** X band

FIGURE 5.4 – Application of spectral estimation techniques to nadir-looking A-scan at C and X bands over the sand-defect zone

Notable disparities are observed when employing high-resolution techniques in B-scan images displayed in Fig. 5.5. Both MUSIC and ESPRIT techniques are able to successfully discriminate the ground and direct responses, and to localize them correctly in the vertical direction. One may note a more stable behavior at C band compared to X band, due to the better SNR. In this case, the properties of these methods allow to easily separate the two layers.

5.4 High-resolution imaging techniques applied in the COSBis configuration

5.4.1 Principles of COSBis focusing using spectral estimation methods

As mentioned in the preceding chapter, the COSBis configuration corresponds to a wide-band near-field situation characterized by range migrations and nonlinear phase behaviors. The application of spectral estimation techniques to such signals reveals certain challenges. Solutions presented in [DeG98 ; Jou+17 ; Mar+98] utilize classical focusing techniques to compensate for near-range migrations and nonlinear phase. High-resolution techniques of spectral analysis may hence be applied to the spectrum of the compensated SAR images. In our case, these techniques are employed in the elevation direction.

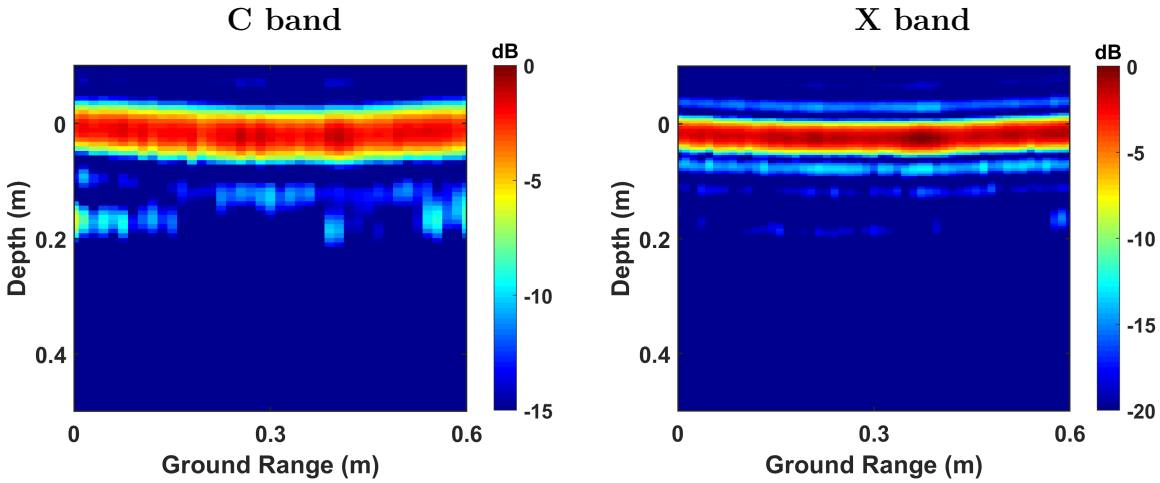

(a) Original images

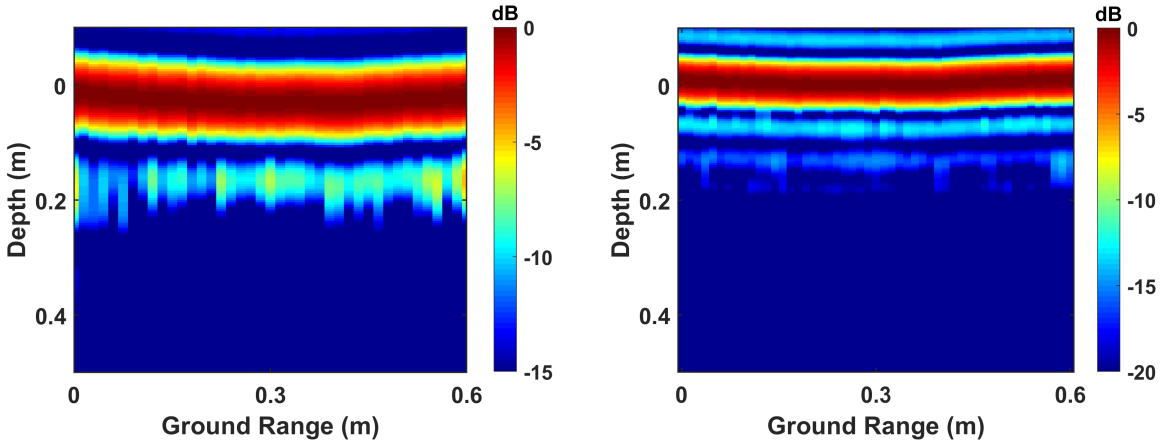

(b) Beamforming images

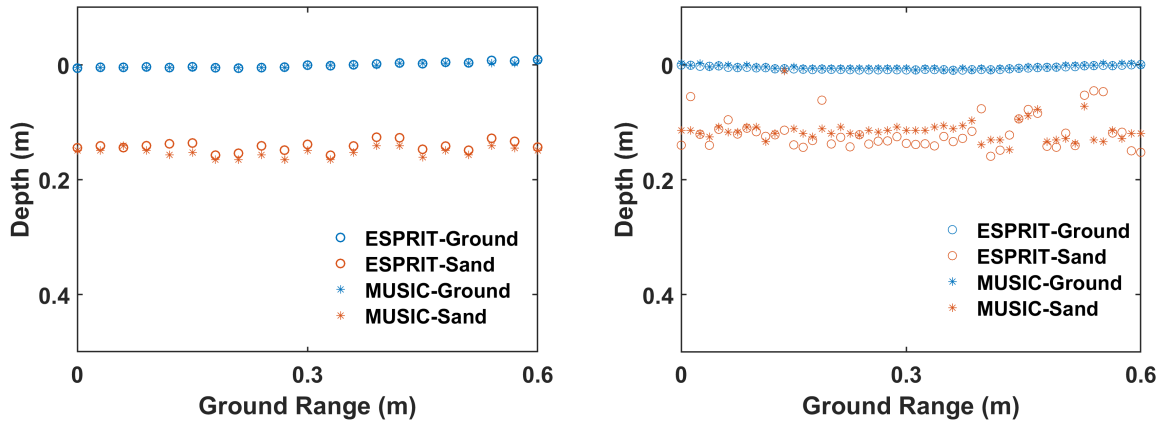

(c) MUSIC and ESPRIT estimated echos

FIGURE 5.5 – Application of spectral estimation techniques to nadir-looking B-scan at C and X bands over the sand-defect zone

One may note that, as mentioned in [Jou+17], in BSC mode, the use of a polar grid when focusing the data is well-adapted to the application of high-resolution techniques, as illustrated in Fig. 5.6a. This accounts for the inclination of the data spectrum, implied by the non-zero incidence angle at which data are measured. In such a case, using a Cartesian grid will lead to a serious deterioration of the performance.

In the COSBis case, as shown in Fig. 5.6b, the spectrum of the focused data is rectangular, with its axes aligned with the ground-range and elevation direction. As a consequence, the simple Cartesian grid is the most adapted reference frame for applying high-resolution techniques.

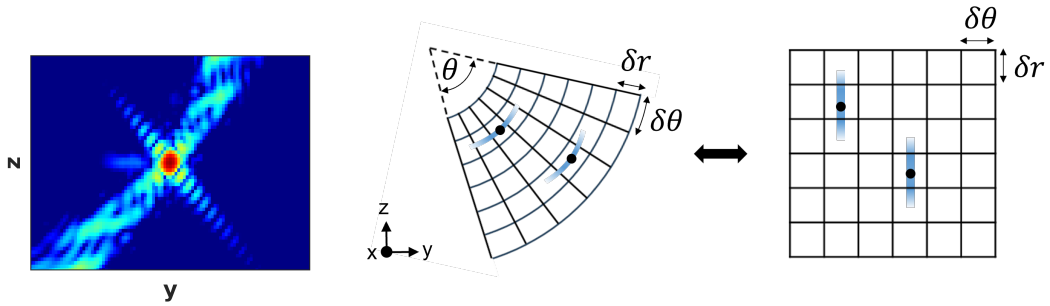

(a) BSC mode - Polar grid

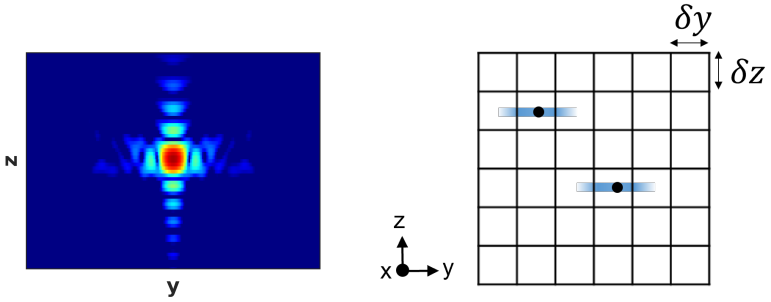

(b) COSBis mode - Cartesian grid

FIGURE 5.6 – Illustration of focusing grids of BSC and COSBis modes

The steps for applying 1-D spectral analysis in elevation to the COSBis configuration are listed as follows :

1. **Fourier Transform :**
   Transform the complex focused 2-D SAR image to the spectral domain by employing a DFT.
2. **Select Useful Spectrum :**
   Define the limits of the useful spectrum and compensate for potential amplitude

variations.

3. **Spectral Smoothing :**
   Apply a spectral smoothing technique to the useful spectrum.
4. **Spectral Estimation :**
   Implement spectral estimation methods on the resulting data from step 3, to obtain the final result.

5.4.2 Horizontal crack

The application of COSBis focusing to pavement inspections has demonstrated its pronounced effectiveness to characterize horizontal cracks, particularly in HH polarization, as displayed in Fig. 5.7b. However, in VV polarization, as shown in Fig. 5.7c, the vertical gap is less discriminated, and distinguishing echoes from the two ground layers proves challenging.

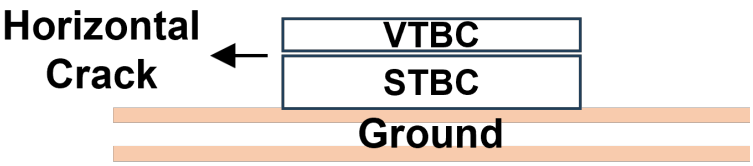

(a) Geometry of the horizontal crack

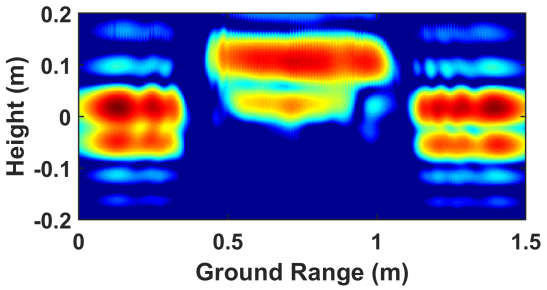

(b) HH polarization

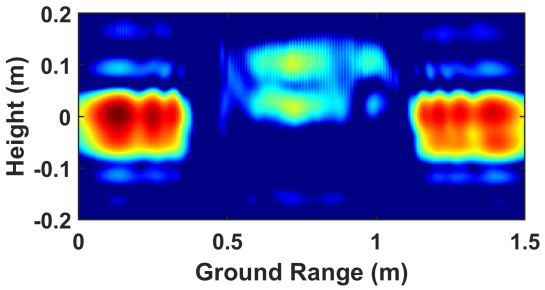

(c) VV polarization

FIGURE 5.7 – Original COSBis images over the horizontal crack

Utilizing nonparametric methods like beamforming and Capon does not improve vertical discrimination, as depicted in Figs. 5.8a and 5.8b, respectively. It even worsens the resolution due to the constrained effective length of samples during spectral smoothing.

In contrast, the MUSIC approach reveals distinct echoes in Fig. 5.8c, originating from the two layers of the ground at their accurate elevations, which are not obtained in the

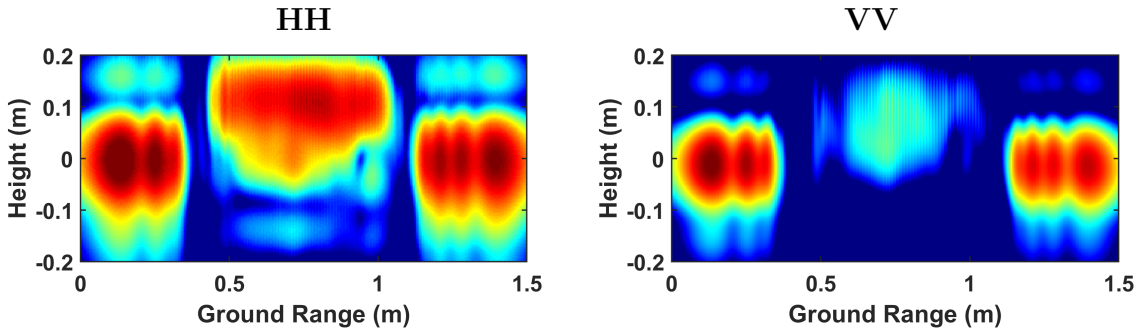

(a) Beamforming images

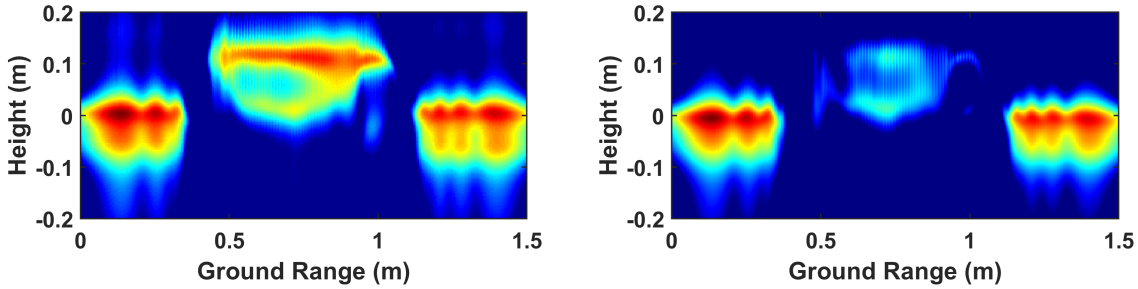

(b) Capon images

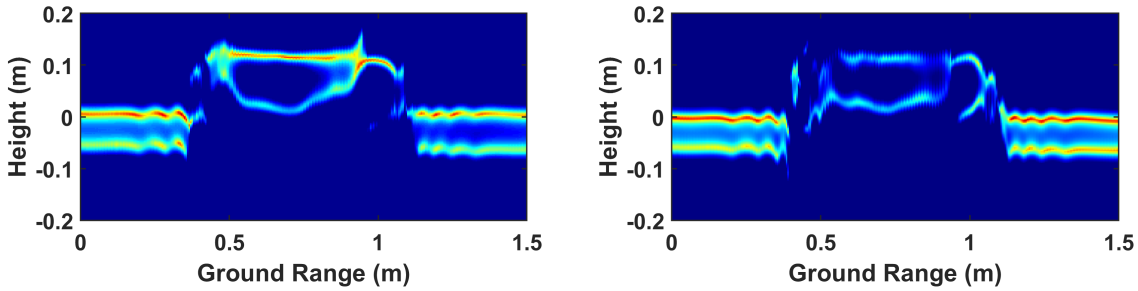

(c) MUSIC - score function images

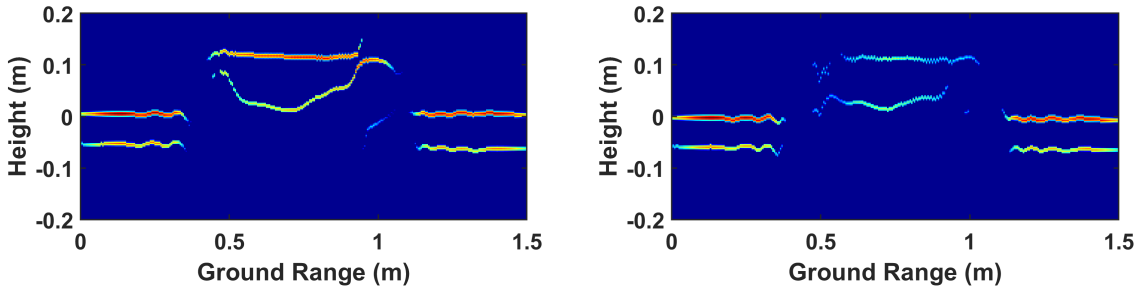

(d) Reconstructed images

FIGURE 5.8 – Application of spectral estimation techniques to COSBis at VV and HH polarizations over the horizontal crack

original focused image in VV polarization. More accurate profiles corresponding to the VTBC and STBC separated by a vertical gap are obtained, through the exploitation of the orthogonality between signal and noise components.

The reflectivity estimates can be obtained from the source elevation, $\hat{\mathbf{z}}$, derived from a spectral analysis technique, using a Least Squares (LS) approach, which corresponds to the CM maximum likelihood solution, as

$$\hat{\boldsymbol{\sigma}} = \mathrm{diag}(\mathbf{A}^{\dagger}(\hat{\mathbf{z}})\widehat{\mathbf{R}}\mathbf{A}^{\dagger H}(\hat{\mathbf{z}})) \tag{5.26}$$

where $\hat{\boldsymbol{\sigma}}$ represents the source intensity vector, and $\mathbf{A}^{\dagger}$ denotes the pseudo-inverse of $\mathbf{A}$. These intensity estimates can then be thresholded in order to discard non-significant contributions. The images displayed in Fig. 5.8d are reconstructed from the parameters, estimated with the MUSIC and LS approaches, i.e. the elevation and intensity of the contributions. With these parameters, an artificial image is synthesized using in a prior waveform, here a Gaussian function, with a very high apparent resolution, which helps to compare the results to those obtained in the full resolution case.

The integration of the MUSIC algorithm in the 2-D imaging process significantly enhances the discrimination of horizontal cracks and provides more precise profiles of slab interfaces. Furthermore, this approach brings to light details that appear as ambiguous features within the ground structure in the initial focusing results.

5.4.3 Vertical crack

Results obtained through the application of the COSBis system for the inspection of vertical cracks have demonstrated their effectiveness in 4.4.4. The discontinuity is hard to perceive in HH polarization as one may notice in Fig. 5.9b, whereas it is accurately localized at its true position in VV polarization, as depicted in Fig. 5.9c, due to the absence of wave transmission through the crack within the slab.

The evaluation of the focusing results using both beamforming and Capon algorithms, as presented in Fig. 5.10a and 5.10b, reveals their ability to discriminate horizontal discontinuities between slabs in VV polarization, whereas the presence of the gap is still not obvious in HH polarization.

The MUSIC algorithm is applied with a preset number of sources $N_s = 2$. The double-layer ground is clearly distinguished as one may see in Fig. 5.10c. However, challenges arise in the slab region, where the true number of contributions is equal to one, and the

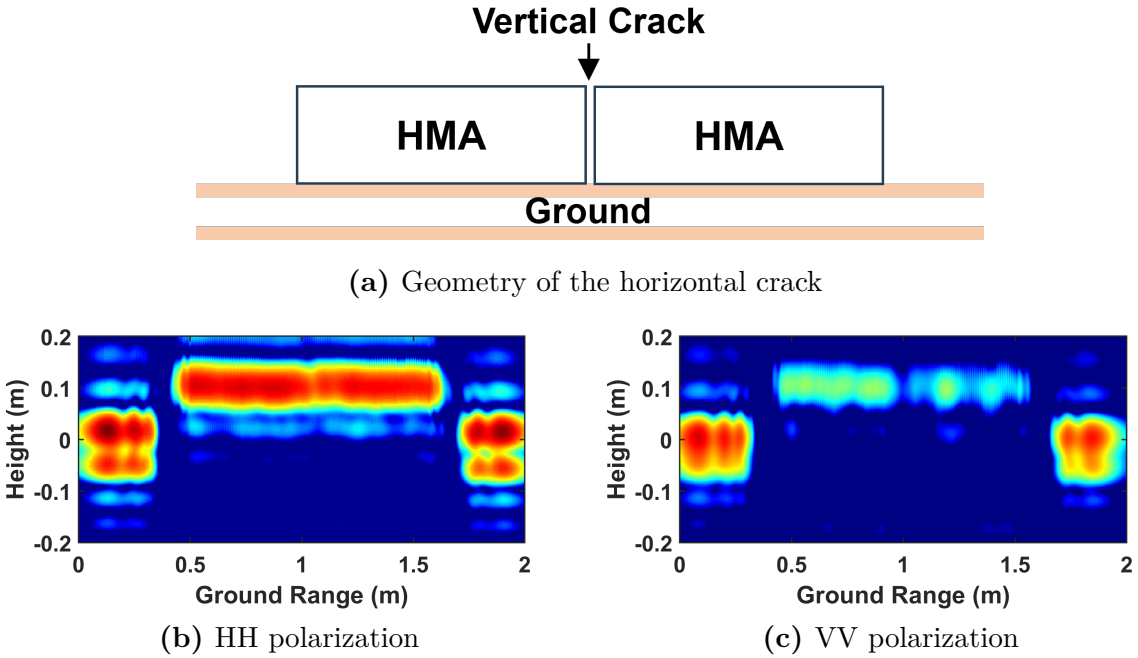

(a) Geometry of the horizontal crack

(b) HH polarization

(c) VV polarization

FIGURE 5.9 – Original COSBis images over the vertical crack

horizontal discontinuity is characterized by invalid responses. Through the application of a selection criterion, the ghost echoes with an LS intensity estimate lying below an established threshold are effectively eliminated. This refined approach is applied to the reconstruction of MUSIC images displayed in Fig. 5.10d, where clear responses indicating the top surface of the two slabs are obtained, and the horizontal discontinuity is identified in VV polarization.

Nonparametric approaches, i.e. beamforming and Capon, are not able to discriminate contributions, due to the limited size of the selected spectrum and the associated coarse resolution. MUSIC provides remarkable improvement in vertical discrimination, while also showcasing its adaptability in complex situations, where the actual number of sources is lower than the preset value, by eliminating invalid ghost echoes through the application of an intensity based criterion.

5.5 Conclusion

In this chapter, high-resolution imaging techniques are applied to the COSBis configuration, with a focus on spectral estimation, aimed at refining the precision of roadway

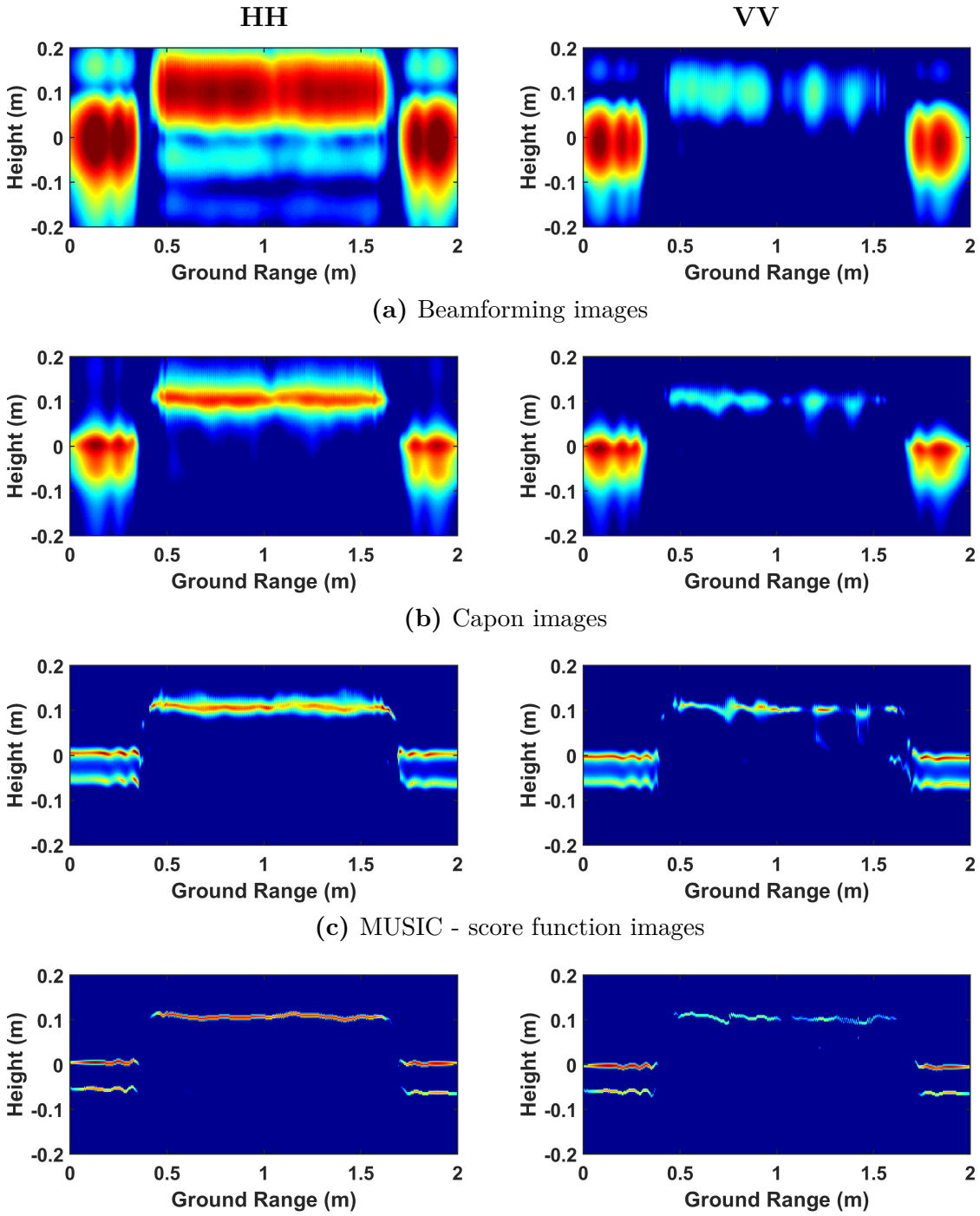

(a) Beamforming images

(b) Capon images

(c) MUSIC - score function images

(d) Reconstructed images

FIGURE 5.10 – Application of spectral estimation techniques to COSBis at VV and HH polarizations over the vertical crack

diagnostics. Subspace spectral smoothing methods are explored within the CM context to decorrelate the received signals. Both nonparametric and parametric spectral estimation approaches are presented to enhance discrimination and detect embedded defects and cracks.

High-resolution techniques are applied onto COSBis focused 2-D SAR images, in order to compensate for near-range migration, and provide a more accurate representation of subsurface features. Results demonstrate that nonparametric approaches such as beamforming and Capon, when applied to the COSBis configuration, do not lead to significant resolution improvements due to their limited resolution. In contrast, the MUSIC algorithm exhibits remarkable improvement in vertical discrimination, even in cases where the actual number of sources is lower than the preset value. This is achieved through the elimination of invalid echoes using a selection criterion.

The COSBis configuration, coupled with high-resolution techniques, represents a promising improvement in subsurface imaging. This methodology has shown significant potential in characterizing both horizontal and vertical cracks, providing more accurate representations of subsurface features. The adaptability of the MUSIC algorithm with the selected criterion, particularly in complex scenarios, highlights its robustness and applicability in practical applications. This study further demonstrates the potential of COSBis in pavement characterization and diagnosis.

Conclusions and perspectives

This dissertation addresses remote sensing techniques for pavement diagnosis and monitoring. It aims to explore 3-D TomoSAR imaging in roadway inspection through the utilization of GB-SAR acquisitions.

A side-looking bistatic GB-SAR configuration is presented in detecting underground defects and characterizing roadways, with its natural high SNR and constant vertical resolution. Signals obtained in FSC mode traveling along a quasi-optical specular path significantly improve the SNR and detection capability, and achieves quasi-constant vertical resolution δz converted from the range resolution δd. Tomography is introduced to resolve the ambiguity problem in the ground-range direction of a single-channel acquisition. The displacement of the transmitting antennas in the vertical direction synthesizes an antenna aperture, which focuses an equivalent beam, brings an improved tomographic ground-range resolution.

Measurements conducted with a laboratory-developed GB-SAR operated at C and X bands over a pavement fatigue carousel, consisted of a ring of full-scale asphalt paved road, are used to evaluate the capability for detecting artificial defects corresponding to very thin layers, or cracks, filled with a geotextile, sand or with air.

The experimental results and theoretical analysis provide valuable insights into the strengths and limitations of the proposed FSC TomoSAR mode, compared with nadir-looking B-scan and BSC TomoSAR modes. Specifically, the nadir-looking configuration proves less effective in discerning subtle defects in the absence of UWB conditions. The BSC TomoSAR mode excels in identifying geotextile and sand defects. The FSC TomoSAR mode emerges as the most promising, successfully isolating and localizing all defect types, benefiting from significant scattered signal amplitudes, even in the X band, where the obtained results show an improved resolution that helps to discriminate the defects.

Furthermore, the incorporation of polarimetric and angular diversities with the side-looking configuration offers additional advantages. This enables the estimation of dielectric permittivity, correction of geometric distortions induced by signal refraction in the 3-D medium, and the assessment of roughness indicators for the imaged interfaces through a scattering model.

It is important to acknowledge that while the FSC TomoSAR mode exhibits good capabilities in road characterization, the horizontal resolution is limited by the vertical aperture of the antenna array. Its operational implementation is constrained by various factors, including the need for a more complex hardware configuration and coherent processing, resulting in longer acquisition times.

A novel configuration of a sliding bistatic SAR, COSBis, is thus proposed, in order to solve the mentioned drawbacks, i.e. high complexity, long acquisition time, and restricted horizontal resolution of the preceding Tomo FSC imaging technique, while keeping the advantages of FSC mode with good and constant vertical resolution and high SNR. A single pair of opposite-side looking Tx and Rx antennas is employed, reducing the system complexity to a minimal level. An angular aperture described by a moving platform horizontal is created using a focusing algorithm, resulting in an improved ground-range resolution. The experiments are conducted with COSBis system, operated in both VV and HH polarizations, over the surface layer of pavement simulated by asphalt samples, i.e. VTBC, STBC, and HMA, containing artificially generated both horizontal and vertical cracks, which yield compelling results.

Experimental results reveal that the sliding FSC mode effectively achieves vertical discrimination compared with nadir-looking GPR over horizontal cracks inside bilayer slabs, and is sensitive to variations in gap width. Vertical cracks are well detected in the sliding FSC mode, due to the improved ground-range discrimination, whereas cracks are not perceived in nadir-looking mode. Notably, a unique horizontal discrimination capability is found in BSC mode, and facilitates clear perception and accurate localization of horizontal discontinuities. Leveraging polarimetric diversity in conjunction with the sliding FSC modes facilitates the estimation of dielectric permittivity over slightly rough asphalt surfaces. The discrimination disparities are observed under different polarizations, with HH polarization exhibiting better sensitivity to vertical discrimination, while VV polarization displays greater discernment of horizontal discontinuities. Double-bounce effects in BSC mode bring a stronger response in HH polarization, at the boundary between the ground and the volume.

COSBis offers a promising alternative for pavement analysis and maintenance. Its inherent strengths lie in its simple configuration, coupled with good discrimination capabilities in both vertical and horizontal dimensions, and sensitivity to polarimetry.

In order to further enhance the capability of COSBis in discriminating pavement defects, high-resolution techniques are applied to improve the precision of roadway diag-

nostics through spectral estimation. Subspace spectral smoothing methods are explored within the CM context to decorrelate the received signals. Both nonparametric and parametric spectral estimation approaches are presented to enhance discrimination and detect embedded defects and cracks.

High-resolution techniques are applied on COSBis focused 2-D SAR images, in order to compensate for near-range migration, and provide a more accurate representation of subsurface features. Results demonstrate that nonparametric approaches such as beamforming and Capon, when applied to the COSBis configuration, do not lead to significant resolution improvements due to the limited resolution. In contrast, the MUSIC algorithm exhibits remarkable improvement in vertical discrimination, even in cases where the actual number of sources is lower than the preset value. This is achieved through the elimination of invalid echoes using a selection criterion.

Two new imaging configurations presented in this paper, Tomo FSC and sliding FSC, are proposed and validated for characterizing embedded cracks and defects in the subsurface of road pavement. The incorporation of polarimetric and angular diversities with the side-looking configuration enables the characterization of pavement, including surface roughness and material dielectric permittivity. The application of high-resolution techniques to COSBis configuration shows a promising improvement in characterizing cracks and more accurate representations of subsurface features.

Perspective

Based on the advancements discussed in this dissertation, some of the key points for future research and development are outlined as following :

— Utilize Tomo FSC for detailed exploration of dispersive characteristics ;

— Implement COSBis on a fast-moving platform to achieve high-speed sampling and global imaging ;

— Apply 2-D spectrum estimation in COSBis configuration to reduce sidelobes and improve discrimination in the ground-range direction ;

— Explore irregular sampling methods, such as co-prime sampling, to reduce sampling requirements and broaden the applicability of research techniques ;

— Extend the application scene to various areas like buildings, snow, ice, grasslands, and farms.

BIBLIOGRAPHIE

[Abd+21] Ray Abdo, Laurent Ferro-Famil, Frederic Boutet et Sophie Allain-Bailhache, « Analysis of the double-bounce interaction between a random volume and an underlying ground, using a controlled high-resolution polto-mosar experiment », in : *Remote Sensing* 13.*4* (2021), p. 636.

[Ado06] Mourad Adous, « Caractérisation électromagnétique des métariaux traités de génie civil dans la bande de fréquence 50 MHz-13 GHz », thèse de doct., Université de Nantes, 2006.

[Agh+20] Hossein Aghababaei, Giampaolo Ferraioli, Laurent Ferro-Famil, Yue Huang, Mauro Mariotti D'Alessandro, Vito Pascazio, Gilda Schirinzi et Stefano Tebaldini, « Forest SAR Tomography : Principles and Applications », in : *IEEE Geoscience and Remote Sensing Magazine* 8.*2* (2020), p. 30-45.

[Ara+16] Steven Araujo, Laurent Delbreilh, Laurent Laguerre, Hervé Dumont, Éric Dargent et Cyrille Fauchard, « Rock permittivity characterization and application of electromagnetic mixing models for density/compactness assessment of HMA by means of step-frequency radar », in : *Near Surface Geophysics* 14.*6* (2016), p. 551-562.

[Bar+20] Maria Barriera, Simon Pouget, Bérengère Lebental et Julien Van Rompu, « In situ pavement monitoring : A review », in : *Infrastructures* 5.*2* (2020), p. 18.

[BP15] Andrea Benedetto et Lara Pajewski, *Civil engineering applications of ground penetrating radar*, Springer, 2015.

[CA21] Qingqing Cao et Imad L Al-Qadi, « Effect of moisture content on calculated dielectric properties of asphalt concrete pavements from ground-penetrating radar measurements », in : *Remote Sensing* 14.*1* (2021), p. 34.

[Cap69] J. Capon, « High-Resolution Frequency-Wavenumber Spectrum Analysis », in : *Proceedings of the IEEE* 57.*8* (août 1969), p. 1408-1418, issn : 1558-2256.

[Cha+07] A. Chazelas, Xavier Dérobert, C. Adous, D. Villain, Vincent Baltazart, F. Laguerre et P. Queffelec, « EM Characterization of Bituminous Concretes Using a Quadratic Experimental Design », in : juill. 2007, p. 278-283, isbn : 978-1-4244-0886-3.

[CW05] Ian G Cumming et Frank H Wong, « Digital processing of synthetic aperture radar data », in : *Artech house* 1.*3* (2005), p. 108-110.

[Dat23] Eurostat Database, *Total length of motorways*, 2023, url : `https://ec.europa.eu/eurostat/databrowser/view/ttr00002/default/table`.

[DeG98] S.R. DeGraaf, « SAR Imaging via Modern 2-D Spectral Estimation Methods », in : *IEEE Transactions on Image Processing* 7.*5* (mai 1998), p. 729-761, issn : 1941-0042.

[Dér+21] Xavier Dérobert, Vincent Baltazart, Jean-Michel Simonin, Shreedhar Savant Todkar, Christophe Norgeot et Ho-Yan Hui, « GPR Monitoring of Artificial Debonded Pavement Structures throughout Its Life Cycle during Accelerated Pavement Testing », in : *Remote Sensing* 13.*8* (2021), p. 1474.

[DJ92] M.D. Desai et W.K. Jenkins, « Convolution Backprojection Image Reconstruction for Spotlight Mode Synthetic Aperture Radar », in : *IEEE Transactions on Image Processing* 1.*4* (oct. 1992), p. 505-517, issn : 1941-0042.

[Dub+06] Pascale Dubois-Fernandez, Hubert Cantalloube, Bernard Vaizan, Gerhard Krieger, Ralf Horn, Michael Wendler et Vincent Giroux, « ONERA-DLR bistatic SAR campaign : Planning, data acquisition, and first analysis of bistatic scattering behaviour of natural and urban targets », in : *IEE Proceedings-Radar, Sonar and Navigation* 153.*3* (2006), p. 214-223.

[Fer+22] Laurent Ferro-Famil, Stefano Tebaldini, Ray Abdo, Lekhmissi Harkati et Mengda Wu, « 3D SAR imaging using bistatic opposite side acquisitions, the bizona concept », in : *2022 19th European Radar Conference (EuRAD)*, IEEE, 2022, p. 209-212.

[Fer13] Laurent Ferro-Famil, « Principes de l'imagerie Radar à synthèse d'ouverture (RSO) », in : *Techniques de l'Ingenieur* (2013).

[FHP16a] Laurent Ferro-Famil, Yue Huang et Eric Pottier, « Principles and Applications of Polarimetric SAR Tomography for the Characterization of Complex Environments », in : *International Association of Geodesy Symposia. F. Sanso Ed.., Springer-Verlag* 142.*1-13* (2016), p. 243-255.

[FHP16b] Laurent Ferro-Famil, Yue Huang et Eric Pottier, « Principles and applications of polarimetric SAR tomography for the characterization of complex environments », in : *VIII Hotine-Marussi Symposium on Mathematical Geodesy : Proceedings of the Symposium in Rome, 17-21 June, 2013*, Springer, 2016, p. 243-255.

[FLS05] G. Fornaro, F. Lombardini et F. Serafino, « Three-Dimensional Multipass SAR Focusing : Experiments with Long-Term Spaceborne Data », in : *IEEE Transactions on Geoscience and Remote Sensing* 43.*4* (avr. 2005), p. 702-714, issn : 1558-0644.

[FP16a] Laurent Ferro-Famil et E. Pottier, « 1 - Synthetic Aperture Radar Imaging », in : *Microwave Remote Sensing of Land Surface*, Elsevier, 2016, p. 1-65.

[FP16b] Laurent Ferro-Famil et E. Pottier, « 2 - SAR Imaging using Coherent Modes of Diversity : SAR Polarimetry, Interferometry and Tomography », in : *Microwave Remote Sensing of Land Surface*, Elsevier, 2016, p. 67-147.

[Fre+17] Othmar Frey, Charles L. Werner, Rafael Caduff et Andreas Wiesmann, « Inversion of SNOW structure parameters from time series of tomographic measurements with SnowScat », in : *2017 IEEE International Geoscience and Remote Sensing Symposium (IGARSS)*, 2017, p. 2472-2475.

[Har+20] Lekhmissi Harkati, Ray Abdo, Stéphane Avrillon et Laurent Ferro-Famil, « Low complexity portable MIMO radar system for the characterisation of complex environments at high resolution », in : *IET Radar, Sonar & Navigation* 14.*7* (2020), p. 992-1000.

[HFR12] Yue Huang, Laurent Ferro-Famil et Andreas Reigber, « Under-Foliage Object Imaging Using SAR Tomography and Polarimetric Spectral Estimators », in : *IEEE Transactions on Geoscience and Remote Sensing* 50.*6* (juin 2012), p. 2213-2225, issn : 1558-0644.

[Hua11] Yue Huang, « Tomographic processing of polarimetric and interferometric SAR data for urban and forestry remote sensing », thèse de doct., Rennes 1, 2011.

[HZF21] Yue Huang, Qiaoping Zhang et Laurent Ferro-Famil, « Forest Height Estimation Using a Single-Pass Airborne L-Band Polarimetric and Interferometric SAR System and Tomographic Techniques », in : *Remote Sensing* 13.*3* (jan. 2021), p. 487, issn : 2072-4292.

[IDR14] IDRRIM, *Livre Blanc IDRRIM "Entretenir et Préserver Le Patrimoine d'infrastructures de Transport : Une Exigence Pour La France"*, oct. 2014.

[JGB03] Edward J Jaselskis, Jonas Grigas et Algirdas Brilingas, « Dielectric properties of asphalt pavement », in : *Journal of materials in Civil Engineering* 15.*5* (2003), p. 427-434.

[Jol08] Harry M Jol, *Ground penetrating radar theory and applications*, Elsevier, 2008.

[Jou+17] Antoine Jouadé, Laurent Ferro-Famil, Stephane Méric, Olivier Lafond et Laurent Le Coq, « High Resolution Radar Focusing Using Spectral Estimation Methods in Wide-Band and Near-Field Configurations : Application to Millimeter-Wave Near-Range Imaging », in : *Progress In Electromagnetics Research* 79 (2017), p. 45-64.

[JZ07] Tian Jin et Zhimin Zhou, « Refraction and dispersion effects compensation for UWB SAR subsurface object imaging », in : *IEEE transactions on geoscience and remote sensing* 45.*12* (2007), p. 4059-4066.

[Kay88] Steven M Kay, *Modern spectral estimation*, Pearson Education India, 1988.

[KM20] Sadra Karimzadeh et Masashi Matsuoka, « Remote Sensing X-Band SAR Data for Land Subsidence and Pavement Monitoring », in : *Sensors* 20.*17* (jan. 2020), p. 4751, issn : 1424-8220.

[KS01] Avinash C. Kak et Malcolm Slaney, *Principles of computerized tomographic imaging*, Philadelphia : Society for Industrial et Applied Mathematics, 2001, isbn : 089871494X 9780898714944.

[KV96] Hamid Krim et Mats Viberg, « Two decades of array signal processing research : the parametric approach », in : *IEEE signal processing magazine* 13.*4* (1996), p. 67-94.

[LDA18] Wallace Wai-Lok Lai, Xavier Derobert et Peter Annan, « A review of Ground Penetrating Radar application in civil engineering : A 30-year journey from Locating and Testing to Imaging and Diagnosis », in : *Ndt & E International* 96 (2018), p. 58-78.

[Le +14] Cédric Le Bastard, Yide Wang, Vincent Baltazart et Xavier Dérobert, « Time Delay and Permittivity Estimation by Ground-Penetrating Radar with Support Vector Regression », in : *IEEE Geoscience and Remote Sensing Letters* 11.*4* (avr. 2014), p. 873-877, issn : 1558-0571.

[Le +19] Cédric Le Bastard, J. Pan, Y. Wang, S. S. Todkar, A. Ihamouten, X. Dérobert, D. Guilbert et M. Sun, « Roadway Interface Analysis with a Support Vector Regression Based Linear Prediction Method Using Stepped-Frequency Radar », in : *IGARSS 2019 - 2019 IEEE International Geoscience and Remote Sensing Symposium*, juill. 2019, p. 3598-3601.

[Le 07] Cédric Le Bastard, « Apport de techniques de traitement du signal super et haute résolution à l'amélioration des performances du radar-chaussée », thèse de doct., Université de Nantes, 2007.

[Liu+23] Hai Liu, Zefan Yang, Yunpeng Yue, Xu Meng, Chao Liu et Jie Cui, « Asphalt pavement characterization by GPR using an air-coupled antenna array », in : *NDT & E International* 133 (2023), p. 102726.

[MAH20] Franz J. Meyer, Olaniyi A. Ajadi et Edward J. Hoppe, « Studying the Applicability of X-Band SAR Data to the Network-Scale Mapping of Pavement Roughness on US Roads », in : *Remote Sensing* 12.*9* (jan. 2020), p. 1507, issn : 2072-4292.

[Mar+98] Sylvie Marcos et al., « Les méthodes à haute résolution », in : *Hermes* 42 (1998).

[Mas96] Kenneth R Maser, « Condition assessment of transportation infrastructure using ground-penetrating radar », in : *Journal of infrastructure systems* 2.*2* (1996), p. 94-101.

[Mir+04] V.L. Mironov, M.C. Dobson, V.H. Kaupp, S.A. Komarov et V.N. Kleshchenko, « Generalized refractive mixing dielectric model for moist soils », in : *IEEE Transactions on Geoscience and Remote Sensing* 42.*4* (2004), p. 773-785.

[Ott+93] Björn Ottersten, Mats Viberg, Petre Stoica et Arye Nehorai, « Exact and large sample maximum likelihood techniques for parameter estimation and detection in array processing », in : *Radar array processing*, Springer, 1993, p. 99-151.

[Ozd+16] Abdulkadir Ozden, Ardeshir Faghri, Mingxin Li et Kaz Tabrizi, « Evaluation of Synthetic Aperture Radar Satellite Remote Sensing for Pavement and Infrastructure Monitoring », in : *Procedia Engineering*, ICSDEC 2016 – Integrating Data Science, Construction and Sustainability 145 (jan. 2016), p. 752-759, issn : 1877-7058.

[Pan+21] Jingjing Pan, Meng Sun, Yide Wang, Cédric Le Bastard et Vincent Baltazart, « Time-Delay Estimation by a Modified Orthogonal Matching Pursuit Method for Rough Pavement », in : *IEEE Transactions on Geoscience and Remote Sensing* 59.*4* (avr. 2021), p. 2973-2981, issn : 1558-0644.

[PK15] Andrea Porubiaková et Jozef Komačka, « A comparison of dielectric constants of various asphalts calculated from time intervals and amplitudes », in : *Procedia Engineering* 111 (2015), p. 660-665.

[Ras+20] Mezgeen A Rasol, Vega Pérez-Gracia, Francisco M Fernandes, Jorge C Pais, Sonia Santos-Assunçao, Caio Santos et Viviana Sossa, « GPR laboratory tests and numerical models to characterize cracks in cement concrete specimens, exemplifying damage in rigid pavement », in : *Measurement* 158 (2020), p. 107662.

[Rek+17] Badreddine Rekioua, Matthieu Davy, Laurent Ferro-Famil et Stefano Tebaldini, « Snowpack permittivity profile retrieval from tomographic SAR data », in : *Comptes Rendus Physique* 18.*1* (2017), p. 57-65.

[Ric51] Stephen O Rice, « Reflection of electromagnetic waves from slightly rough surfaces », in : *Communications on pure and applied mathematics* 4.*2-3* (1951), p. 351-378.

[RK89] R. Roy et T. Kailath, « ESPRIT-Estimation of Signal Parameters via Rotational Invariance Techniques », in : *IEEE Transactions on Acoustics, Speech, and Signal Processing* 37.*7* (juill. 1989), p. 984-995, issn : 0096-3518.

[RM00] A. Reigber et A. Moreira, « First demonstration of airborne SAR tomography using multibaseline L-band data », in : *Geoscience and Remote Sensing, IEEE Transactions on* 38.*5* (sept. 2000), p. 2142-2152, issn : 0196-2892.

[Sau+11] Stefan Sauer, Laurent Ferro-Famil, Andreas Reigber et Eric Pottier, « Three-Dimensional Imaging and Scattering Mechanism Estimation Over Urban Scenes Using Dual-Baseline Polarimetric InSAR Observations at L-Band », in : *IEEE Transactions on Geoscience and Remote Sensing* 49.*11* (nov. 2011), p. 4616-4629, issn : 1558-0644.

[Sch86] R. Schmidt, « Multiple Emitter Location and Signal Parameter Estimation », in : *IEEE Transactions on Antennas and Propagation* 34.*3* (mars 1986), p. 276-280, issn : 1558-2221.

[SET94] LCPC SETRA, *Conception et Dimensionnement des Structures de Chaussée : Guide Technique*, Laboratoire Central des Ponts et Chaussées et Service d'Études Techniques des Routes et Autoroutes, Ministère de l'Équipement, des Transports et du Tourisme, 1994.

[Sim+14] JM Simonin, V Baltazart, P Hornych, X Dérobert, E Thibaut, J Sala et V Utsi, « Case study of detection of artificial defects in an experimental pavement structure using 3D GPR systems », in : *Proceedings of the 15th International Conference on Ground Penetrating Radar*, IEEE, 2014, p. 847-851.

[Sko08] Merrill Ivan Skolnik, *Radar handbook*, McGraw-Hill, 2008.

[SM+05] Petre Stoica, Randolph L Moses et al., *Spectral analysis of signals*, t. 452, Pearson Prentice Hall Upper Saddle River, NJ, 2005.

[Sou99] Mehrdad Soumekh, *Synthetic aperture radar signal processing*, t. 7, New York : Wiley, 1999.

[SPF21] Mercedes Solla, Vega Pérez-Gracia et Simona Fontul, « A Review of GPR Application on Transport Infrastructures : Troubleshooting and Best Practices », in : *Remote Sensing* 13.*4* (2021), issn : 2072-4292.

[SS00] Timo Saarenketo et Tom Scullion, « Road Evaluation with Ground Penetrating Radar », in : *Journal of Applied Geophysics* 43.*2* (mars 2000), p. 119-138, issn : 0926-9851.

[Sta19] European Standard, *EN 12697-33. Bituminous Mixtures-Test Method-Part 33 : Specimen Prepared by Roller Compactor*, 2019.

[Sun+18] Meng Sun, Cédric Le Bastard, Yide Wang, Nicolas Pinel, Jingjing Pan, Vincent Baltazart, Jean-Michel Simonin et Xavier Dérobert, « Time Delay and Interface Roughness Estimation Using Modified ESPRIT with Interpolated Spatial Smoothing Technique », in : *IEEE Transactions on Geoscience and Remote Sensing* 56.*3* (mars 2018), p. 1475-1484, issn : 1558-0644.

[Sun+19] M. Sun, J. Pan, C. Le Bastard, Y. Wang et J. Li, « Advanced Signal Processing Methods for Ground-Penetrating Radar : Applications to Civil Engineering », in : *IEEE Signal Processing Magazine* 36.*4* (2019), p. 74-84.

[Sun+22] Meng Sun, Jingjing Pan, Yide Wang, Xiaofei Zhang, Xiaoting Xiao, Cyrille Fauchard et Cédric Le Bastard, « Time-Delay Estimation by Enhanced Orthogonal Matching Pursuit Method for Thin Asphalt Pavement with Similar Permittivity », in : *IEEE Transactions on Intelligent Transportation Systems* 23.*7* (juill. 2022), p. 8940-8948, issn : 1558-0016.

[Teb+16] Stefano Tebaldini, Thomas Nagler, Helmut Rott et Achim Heilig, « Imaging the internal structure of an alpine glacier via L-band airborne SAR tomography », in : *IEEE Transactions on Geoscience and Remote Sensing* 54.*12* (2016), p. 7197-7209.

[TKD04] Leung Tsang, Jin Au Kong et Kung-Hau Ding, *Scattering of electromagnetic waves : theories and applications*, t. 27, John Wiley & Sons, 2004.

[TR12] Stefano Tebaldini et Fabio Rocca, « Multibaseline Polarimetric SAR Tomography of a Boreal Forest at P- and L-Bands », in : *IEEE Transactions on Geoscience and Remote Sensing* 50.*1* (2012), p. 232-246.

[UMF81] F.T. Ulaby, R.K. Moore et A.K. Fung, *Microwave Remote Sensing : Active and Passive*, Artech House microwave library v. 3, Artech House, 1981, isbn : 9780890061923.

[WFW21] Mengda Wu, Laurent Ferro-Famil et Yide Wang, « Comparison of radar imaging configurations for the characterization and diagnosis of roadways », in : *2021 IEEE International Geoscience and Remote Sensing Symposium IGARSS*, IEEE, 2021, p. 1958-1961.

[Wu+23a] Mengda Wu, Laurent Ferro-Famil, Frederic Boutet et Yide Wang, « A New Ground-Based SAR Technique for Roadway Characterization and Deterioration Inspection », in : *2023 20th European Radar Conference (EuRAD)*, IEEE, 2023, p. 258-261.

[Wu+23b] Mengda Wu, Laurent Ferro-Famil, Frederic Boutet et Yide Wang, « Comparison of Imaging Radar Configurations for Roadway Inspection and Characterization », in : *Sensors* 23.*20* (2023), issn : 1424-8220.

[Yit+16] Temesgen Gebrie Yitayew, Laurent Ferro-Famil, Torbjørn Eltoft et Stefano Tebaldini, « Tomographic imaging of Fjord ice using a very high resolution ground-based SAR system », in : *IEEE Transactions on Geoscience and Remote Sensing* 55.*2* (2016), p. 698-714.

[Yit+17] Temesgen Gebrie Yitayew, Laurent Ferro-Famil, Torbjørn Eltoft et Stefano Tebaldini, « Lake and Fjord Ice Imaging Using a Multifrequency Ground-Based Tomographic SAR System », in : *IEEE Journal of Selected Topics in Applied Earth Observations and Remote Sensing* 10.*10* (oct. 2017), p. 4457-4468, issn : 2151-1535.

[Zhe+20] YL Zheng, XB Zhao, QH Zhao, JC Li et QB Zhang, « Dielectric properties of hard rock minerals and implications for microwave-assisted rock fracturing », in : *Geomechanics and Geophysics for Geo-Energy and Geo-Resources* 6.*1* (2020), p. 22.

PUBLICATIONS

[1] Mengda Wu, Laurent Ferro-Famil, Frederic Boutet et Yide Wang, « Comparison of Imaging Radar Configurations for Roadway Inspection and Characterization », in : *Sensors* 23.*20* (2023), issn : 1424-8220

[2] Mengda Wu, Laurent Ferro-Famil, Frederic Boutet et Yide Wang, « A New Ground-Based SAR Technique for Roadway Characterization and Deterioration Inspection », in : *2023 20th European Radar Conference (EuRAD)*, IEEE, 2023, p. 258-261

[3] Mengda Wu, Laurent Ferro-Famil et Yide Wang, « Comparison of radar imaging configurations for the characterization and diagnosis of roadways », in : *2021 IEEE International Geoscience and Remote Sensing Symposium IGARSS*, IEEE, 2021, p. 1958-1961

[4] Laurent Ferro-Famil, Stefano Tebaldini, Ray Abdo, Lekhmissi Harkati et Mengda Wu, « 3D SAR imaging using bistatic opposite side acquisitions, the bizona concept », in : *2022 19th European Radar Conference (EuRAD)*, IEEE, 2022, p. 209-212

COLLEGE DOCTORAL BRETAGNE
MATHS, TELECOMS
INFORMATIQUE, SIGNAL
SYSTEMES, ELECTRONIQUE

Université de Rennes

Titre : Techniques d'imagerie radar pour la caractérisation et le diagnostic des chaussées

Mot clés : radar à synthèse d'ouverture (SAR) ; radar de pénétration de sol (GPR) ; SAR de terrain (GB-SAR) ; tomographie SAR (Tomo-SAR) ; propagation vers l'avant ; rétro diffusion

Résumé : Ce travail concerne l'imagerie tomographique 3-D par Radar à Synthèse d'Ouverture au sol (GB-SAR) pour la détection in situ des défauts de chaussée. Un GB-SAR bistatique à visée latérale, fonctionnant en mode de propagation vers l'avant (FSC), caractérisé par un rapport Signal sur Bruit (SNR) élevé et une résolution verticale constante, est proposé. Une focalisation tomographique utilisant une ouverture dans la direction verticale est introduite pour résoudre l'ambiguïté et améliorer la résolution en distance au sol. Une configuration SAR bistatique FSC à déplacement horizontal et à décalage constant (COSBis), est proposée afin de réduire la complexité du système à un niveau minimal, en utilisant une seule paire d'antennes Tx et Rx, et qui permet d'obtenir une résolution en distance au sol améliorée par focalisation sur une ouverture angulaire générée par le mouvement horizontal. Les résultats expérimentaux démontrent la capacité du mode proposé à détecter des défauts artificiels et à caractériser des détails fins en utilisant une diversité de polarisation. Des techniques d'analyse spectrale à haute résolution sont appliquées à l'approche COSBis pour affiner le diagnostic routier. Cette configuration innovante de GB-SAR, associée à des techniques d'imagerie à haute résolution, démontre un fort potentiel pour l'inspection et la maintenance des chaussées.

Title: Radar imaging techniques for the characterization and diagnosis of roadways

Keywords: synthetic aperture radar (SAR); ground penetrating radar (GPR); ground-based SAR (GB-SAR); SAR tomography (Tomo-SAR); forward scattering; back scattering

Abstract: This work concerns 3-D tomographic imaging with Ground-Based Synthetic Aperture Radar (GB-SAR) for in situ pavement defect detection. A side-looking bistatic GB-SAR operated in forward-scattering (FSC) mode characterized by a high Signal-to-Noise Ratio (SNR) and constant vertical resolution is proposed. Tomographic focusing is introduced to solve the ground-range ambiguity and improve the resolution by using an additional vertical aperture. A Constant Offset Sliding Bistatic (COSBis) SAR configuration operated in the FSC mode is proposed, which reduces the system complexity to a minimal level by using a single pair of Tx and Rx antennas, leading to an improved ground-range resolution, through focusing along an angular aperture created by the horizontal motion. Experimental results demonstrate the capability of the proposed mode for detecting artificial defects, and characterizing detailed features by employing polarimetric diversity. High-resolution techniques are applied to COSBis approach to refine roadway diagnosis. The innovative GB-SAR configuration, coupled with high-resolution imaging techniques, proves a good potential for roadway inspection and maintenance.